UNIVERSIDADE DE SANTIAGO DE COMPOSTELA

FACULTADE DE FÍSICA

DEPARTAMENTO DE FÍSICA DE PARTÍCULAS

Grupo de Imagen Molecular y Física Médica

PhD THESIS

Development of silicon sensors for dosimetry and microdosimetry.

Author:
Juan Prieto Pena

PhD supervisor:
Faustino Gómez Rodríguez

Santiago de Compostela, October 2019

USC
UNIVERSIDADE
DE SANTIAGO
DE COMPOSTELA

USC
UNIVERSIDADE
DE SANTIAGO
DE COMPOSTELA

USC
UNIVERSIDADE
DE SANTIAGO
DE COMPOSTELA

Dr. Faustino Gómez Rodríguez, Profesor Titular do Departamento de Física de Partículas da Universidade de Santiago de Compostela,

CERTIFICA

Que a presente memoria titulada ≪*Development of silicon sensors for dosimetry and microdosimetry*≫ foi realizada por **D. Juan Prieto Pena** baixo a súa dirección no Departamento de Física de Partículas da Universidade de Santiago de Compostela e constitúe a Tese que presenta para optar ao título de Doutor pola Universidade de Santiago de Compostela.

Santiago de Compostela, outubro de 2019

Faustino Gómez Rodríguez
Director da tese

Juan Prieto Pena
Autor da tese

USC
UNIVERSIDADE
DE SANTIAGO
DE COMPOSTELA

A mis padres, a mi hermano y a María.

USC
UNIVERSIDADE
DE SANTIAGO
DE COMPOSTELA

Acknowledgments

I think some acknowledgment for the support and help that some people have provided is in order, or in words of my wise mother, "De bien nacido es ser agradecido". This dissertation would be so much different (or even non-existent) without their support and input.

The first person I want to express my sincere gratitude and acknowledge all the support that he provided me all this years is my supervisor, Faustino Gómez Rodríguez for all his help along this path. His advice not only in scientific matters, but also all kind of problems we had to deal throughout the research and writing process. His kind words when I thought that I was not going to make it helped me to carry on and if you, reader, have this document in your hands is probably thanks to him. Almost all I learned about research and medical physics is thanks to him.

Also, I would like to offer my most sincere gratitude to the rest of the people from our research group, Diego González and Nicolás Gómez, for their support and help with some of the experiments we performed on the microdosimeters. I would like to also thank them for all the coffee breaks and happy times during the conferences we have been together. I hope the future will bring more people like you near me, as I felt humbled of working alongside you and learning all the knowledge you shared with me. Antonio Pazos, our technician, was the backbone of all the experiments and deserves some acknowledgement here and my gratitude,

for delivering all those electric bondings on time, even when I broke them with my clumsy fingers. Thank you for teaching me how to treat all the equipment and letting me borrow some of yours.

A big thank you to my colleagues from other institutions, specially to Dr. Consuelo Guardiola, who helped me a lot throughout these years and who contributed enormously to most of the work presented in this thesis, the people from CNM in Barcelona, Dr. Celeste Fleta, Dr. Sergi Esteban (who allowed me to use some of his figures in this thesis, for the fabrication process of the silicon detectors), and last but not least, the INFN medical physics group in Turin (Roberto, Simona, Marco, Valeria, Lorenzo...) who helped me during my stay, showed me new italian (and specially Piedmontese) food and to pass time during the long hours of the experimental shift at CNAO.

My friends deserve another acknowledgement paragraph on their own, since I think their contribution to my wellness was invaluable. All my friends from Santiago, PhD students or not, with whom I shared my free time since I have started my studies. Thank you, Javi Díaz, Manu Fraga, Jose Castaño, Daniel Sóñora, Manu Feijoo, María Aymerich, Pablo Antonio Lombao, Damián García and Simón Bujía for all those fun times, movie nights, concerts and laughter during these four years. Also all the people from Lugo with whom I shared almost all my life since we started school together when we were three and also the ones that tagged along the way, Laura Pérez, Adrián Salgado, Fran González, Javi Gauna, Carlos Rubio and many more. I hope we will continue to be friends for thirty or thirty hundred more years. A big thank you also to Irenita for supporting me in the troubled years of 2017-18. And also thanks Costa, Itu, Fer, Grande, David, Choco, Pedro and Breixo for all the geekiness, RPGs and laughter.

A very special mention should be made to two very special friends that I met during our undergrad years and deserve a whole paragraph on their own: Yass

and Malpica. These two are the most similar thing I would have to brothers-in-arms (even though Malpica would prefer the term comrades). Without you the degree, master and PhD would be much more boring and dull, and that flat would be less crazy and fun without all those CK2/EUIV/HoI4 shenanigans. Gloria al 14 y a las pizzas cojonudas con los colegas.

A big thank you also for our neighbours from the Optics school, Maite Flores-Arias, Justo Arines, Carmen Bao, Ferran Cambronero, Ángel Aragón and the aforementioned María and Manuel (Blanco) for letting me experiment with a field a little bit different from what I was used to and for all the "research group meetings" involving scotch and gossip. I hope we can raise our glasses one meeting more.

Even though she arrived relatively late to my life, when I was wrapping up all the research I have done during these years and starting to write this dissertation, I would like to thank María Álvarez all the support she gave me during the most difficult months of my PhD life, writing all this. Thank you, María for your support and not sending me to hell even though I am pretty sure you felt tempted a couple times (I would have done it to me probably). I hope we will find more happy times together now that I will not be so stressed (I hope!).

And last but not least, I want to thank all the support I received from my family during all these years. All my possible successes will be thanks to them. Thanks to my mother, Carmen, my father, Ramón, for my upbringing and teaching me values that helped me reaching this very point of my life in which I am now. Thanks to my brother, Ramón (Jr.), for all the fun we had and all the computer games he recommended me to blow off steam (in Steam! hehe). Also I wish to thank my uncles, José Ángel and Isabel, and my grandparents, Arsenio and Carmiña, for all their loving support and raising me along my parents.

There are so much people to thank and not so much space, but I think all the personnel from the university deserve some gratitude, specially the people in administration, economic affairs and the janitorial service from the faculty for having so much patience and understanding when I was a newbie there. You are the unsung heroes of this story. Also, thanks to Elvira Canosa, the secretary of the department of Particle Physics for all her help with the bureaucratic system of this old University.

I acknowledge the financial support of the Spanish Government through the Ministerio de Economía y Competitividad grant MINECO DPI2014-57645-R. I would also like to acknowledge the support of the Fundación Barrié through the funding of my visiting research stay in Turin (Italy) in 2016 with a predoctoral stay grant.

"Natura non nisi parendo vincitur"

Francis Bacon.

"Equipped with his five senses, man explores the universe around him and calls the adventure Science."

Edwin Powell Hubble.

"If curiosity killed the cat, it was satisfaction that brought it back."

Holly Black.

USC
UNIVERSIDADE
DE SANTIAGO
DE COMPOSTELA

Contents

USC
UNIVERSIDADE
DE SANTIAGO
DE COMPOSTELA

Chapter 1

Introduction

Cancer is a broad term that defines a very large number of different diseases that are characterized by certain common traits [1, 2]: Self-stimulation of growth, insensitivity to growth inhibitory signals, evasion of apoptosis, limitless replicative potential, sustained angiogenesis, tissue invasion and metastasis, reprogramming of the body's energy metabolism and mechanisms to avoid immune response from the host's body.

The IARC (International Agency for Research on Cancer, an UN-dependent Agency) in its 2014 Cancer report [3] shows that cancer is one of the biggest causes of mortality worldwide, with around 14 million cases reported and 8 million direct attributable deaths only in the year 2012.

Reports show [4] that the number of cases projected for developed countries will increase by 20-60% in 2030, depending on the type of cancer studied due to the continuous increase in the living expectancy and the increase in healthcare quality.

Traditionally, the main avenues for cancer treatment were three, often combined between them: Surgery, chemotherapy and radiation therapy (RT). Currently, novel treatments are being developed, such as hormonal therapy or immunotherapy. Choice of method is dependent on the size and localisation of the tumour site, stage and other several factors.

The most common treatment for cancer, either as a main treatment or a coadjuvant one, is radiotherapy. It is estimated that around the 50% of all cancer treatments use any type of radiotherapy [5, 6]. This type of treatment has been demonstrated to be an efficient tool for a successful tumour control [7].

In radiotherapy, a certain quantity of radiation is prescribed by a physician to reach the tumour volume. The goal of radiotherapy is delivering to the tumour volume a prescribed dose of radiation, avoiding damage to healthy tissue if possible.

Dosimeters are used to verify that dose prescribed by a physician in the tumour volume is delivered to the patient correctly. Quality assurance programs describe how to measure dose appropriately [8, 9]. These devices work by reading the response to the radiation of a material by different means of processes (physical, chemical...) of a known size. By knowing the processes endured by the detector material to the radiation one can translate the measured affected property to a measurement of the dose imparted in the material.

Since tumour tissue is generally less radioresistant than healthy tissue, radiotherapy can provide a way to damage more the tumour region while not affecting significantly the healthy tissues surrounding the tumour area. Ionising radiation cannot distinguish between healthy and tumour tissue, except for some unusual types of radiotherapy, as Boron Neutron Capture Therapy, in which a tumour-binding drug with ^{10}B is injected and then the patient is irradiated with neutrons. Since ^{10}B has a high cross section for neutrons the radiation interacts more in the tumour area. Extreme care should be taken in order to avoid unnecessary damage that could compromise the correct healing of the patient.

There are several ways to accomplish this depending on the particularities of the disease. As stated before, cancer is a very broad term, and the tumour can take several forms (different types of cells, solid or liquid tumours, definition of the tumour area, etc.). Dose can be provided externally (as in linear accelerators) or internally (brachytherapy). The particles employed can be also different (electrons, photons, neutrons or even heavier particles as atomic nuclei). In this work we will focus on the effects of protons and atomic nuclei in tumour tissues,

called particle therapy (PT) or hadrontherapy.

External radiotherapy will always damage the healthy tissue around the tumour, delivering dose all over its propagation trajectory but several technological developments heavily reliant on imaging techniques can minimise the probability of complications. Also, traditionally, the treatments are fractionated, in order to allow the healthy tissue to repair the damage done by ionizing radiation and to attack the tumour cells in different stages of their cellular cycle.

A way to minimise damage to healthy tissue is to superpose several beams entering from different parts of the patient's body and make them converge in the region of interest, delivering the prescribed dose in the tumour volume. The shape of the beam can be adjusted to conform to the cross-section of the tumour to further minimise the damage to healthy tissue. This technique is called beam conformation.

The most common flavour of radiotherapy employs photons to irradiate the tumour volume. Nowadays, this form of radiotherapy is highly advanced [7], using Image-Guided Radiotherapy (IGRT) techniques, such as Intensity-modulated RT (IMRT) or stereotactic body RT (SBRT), allowing a very high dose conformation to the tumour volume. Combining these techniques with hypo-fractionation in some specific types of tumours, the treatment time can be greatly reduced, even to a unique fraction, allowing RT to compete directly with surgery in some cases.

Due to the nature of the interaction between radiation and matter, specially the exponential decay of the intensity with depth in the case of X-Ray radiation, it is necessary to irradiate the healthy tissue surrounding the tumour area, increasing the probability of further complications in the patient.

A different approach was proposed by Robert Wilson in 1946. In his seminal paper [10] Wilson proposed the use of heavier charged particles for therapy, citing several advantages of using protons (and heavier particles) instead of X-rays, giving birth to the field of Particle Therapy.

The rationale behind it is that nuclei provoke a higher damage both at cellular and sub-cellular level than traditional radiotherapy using photons and electrons and a better dose conformation. By using heavier charged particles, additional

advantages can be obtained due to the higher deposition of energy per unit length (Linear Energy Transfer or LET) and the different behaviour of cells to different types of radiation. Using protons or ions, healthy tissue is irradiated with low-LET radiation, slightly similar to X-Rays, while the tumour region is irradiated with high-LET particles. Charged particles traverse the media in a very straight line, and its particle range is heavily dependent on the kinetic energy they have in the entrance of the body and the mean ionization potential of the medium. Charged particles deposit most of their energy at the end of their range and a very little amount of energy in the body entrance. By using a different mixture of energies, the whole tumour volume can be covered. Figure 1.1 shows the dose profiles in depth of photons compared to protons and carbon ions.

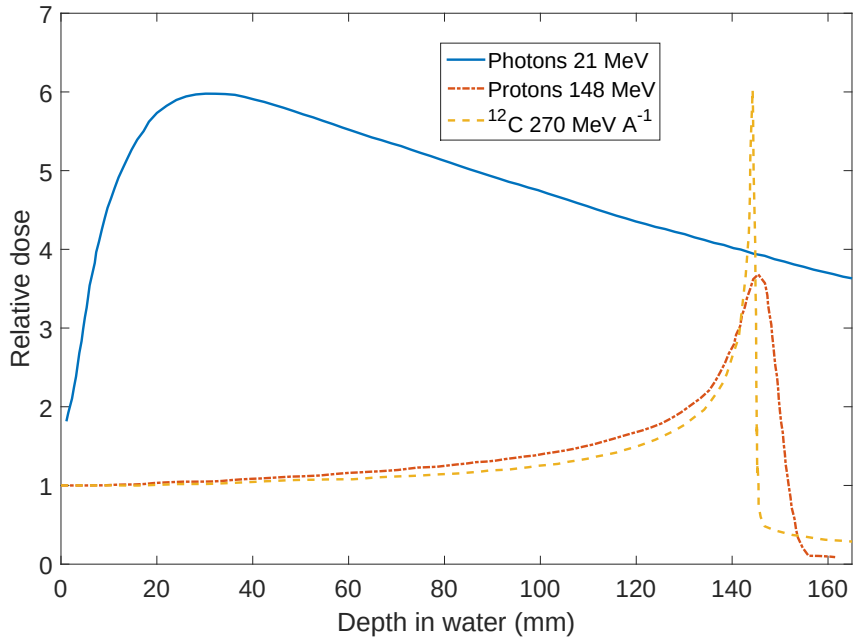

Figure 1.1: Different depth dose distributions for 21 MeV photons, 148 MeV protons and 270 MeV A^{-1} ^{12}C ions. Data taken from [11]

The number of proton and ion radiotherapy facilities has been growing steadily during the past decade [12]. In the case of Europe, particle therapy started its

course in Uppsala, Sweden in the year 1953. According to PTCOG [13], there are currently 80 facilities in operation (as of January 2019) and 67 particle therapy centres (either in planning phase or under construction). Currently, in Spain, two private hospitals are building proton therapy centres in Madrid with opening planned in 2019 and 2020.

Although there is no significant evidence in favour of using protons and heavier charged particles for the treatment of tumours [14] there is evidence that for some types of tumours the use of particle therapy results in less secondary complications [15]. This suggests that further research on the topic to assess the validity of these new techniques and its effectiveness against cancer is of clinical interest.

To study the biological processes and energy deposition in small masses related to radiation-matter interaction a new approach to the dosimetry, called microdosimetry, is employed [16, 17]. From the microdosimetric behaviour of the radiation in the energy transfer to cells, radiation weighting factors can be obtained. Lineal energy distributions can be benchmarked to a Monte Carlo model to aid experimental methods and perform beam characterization [18, 19].

The contents of this dissertation are the results from research in the field of microdosimetry and silicon detectors for hadrontherapy done at the Molecular Imaging and Medical Physics group of the University of Santiago de Compostela (USC) from 2014 to 2019.

Chapter two consists of a brief introduction to describe the basic terms employed through the dissertation and the theory in which the following chapters are sustained, with a description of radiation physics, different physical quantities employed in the dissertation, an introduction to dosimetry and microdosimetry, radiobiology, radiation detectors, and Monte Carlo simulation.

Next, **chapter three** describes the different silicon devices employed for measuring the particle beams, with an electrical characterisation of the different silicon detectors, their layout, the electrical circuits used to obtain the signal, all the associated 'hardware' employed to get the data for this thesis, and a study on the limitations of these particular detection systems.

Chapter four is focused on the data obtained, with a description of the

Monte Carlo methods used to compare the experimental data with the theoretical results, a description of the monoenergetic fields used, the results for carbon nuclei.

Finally, **chapter five** discusses future work on the microdosimeters, some of the possible improvements that could be done to the system in order to increase accuracy with respect to physical characteristics of the silicon detectors, the possible changes to the data acquisition system and changes to charge collection efficiency, and also states the conclusions from this work.

Chapter 2

Background and state of the art

Summary of the chapter:

This chapter presents the theoretical background needed to understand the following chapters of this manuscript, regarding radiation-matter interaction, dosimetry, microdosimetry, and radiobiology.

2.1 Radiation-matter interaction

The emission or transmission of energy by any method and through any medium is called radiation. Radiation can be classified into two large groups according to its capability to produce or not ionisation in the media in which it is travelling, i.e. transferring enough energy to create a pair electron-ion. Inside the group of ionising radiation, it can be further classified by which mechanism employs to provoke said ionisation [20].

In the medical physics energy regime, directly ionising radiation (charged particles) deposit energy mainly by means of direct Coulomb interactions between the incident radiation and the atom-bound electrons present in the media. On the other hand, uncharged particles as photons or neutrons deposit energy in the medium in an indirect manner through a two-step process: in the first step the neutral particle provokes a release of a charged particle in the medium through one particular process (e.g. photoelectric effect in the case of photons or spallation in the case of neutrons). Afterwards, the released charged particles deposit the energy by electromagnetic interactions in the surrounding media.

The radiation field can be assessed in terms of the incident number of radiation quanta per unit area. This term is called fluence as shown in equation 2.1.

$$\Phi \equiv \frac{dN}{da} \tag{2.1}$$

Where dN is the number of particles incident on a sphere of elemental cross-sectional area da [21]. The time-derivative of this quantity is called fluence rate, denoted by placing a point over the fluence sign. It denotes the number of particles crossing the unit area per unit time.

$$\dot{\Phi} \equiv \frac{d\Phi}{dt} = \frac{d^2N}{da\ dt} \tag{2.2}$$

2.1.1 Interaction of charged particles with matter

When a charged particle (e.g. electrons, protons, carbon ions) propagates through matter interacts with its surrounding media through several kinds of processes. These processes can involve slowing down of the incident particle through collisions with the numerous atomic electrons, elastic scattering with atomic nuclei, head-on collisions with the atom (inelastic interactions) that can give birth to daughter particles that will deposit their kinetic energy on their own or, in the case of electrons, hard deflections that will generate a photon (Bremsstrahlung) [22].

All these processes will provoke a more or less important loss of energy of the incident radiation and the relative importance of those processes will vary with the kinetic energy of the particle, its type, mass, and the characteristics of the traversed medium. The trajectory of the particles will be modified by elastic and Coulomb scattering processes leading to a beam broadening as the particles penetrate further into the media. These processes are well modelled and understood by current scattering and stopping theories. Nuclear processes that can give birth to daughter particles, on the other hand, are described by a patchwork of different models but fortunately its occurrence in hadrontherapy is limited and the cases found in the range of energies employed can be described by simple approximations.

The rate at which the incident radiation losses its energy is described by the linear stopping power, as shown in the following equation.

$$S \equiv -\frac{dE}{dx} \tag{2.3}$$

Where dE is the quantity of energy lost by the particle in a distance dx. The usual units for the stopping power are MeV cm^{-1} instead of the SI standard units, J m^{-1}. Stopping power is usually described in terms of the media density with the mass stopping power, as shown in equation 2.4.

$$\frac{S}{\rho} \equiv -\frac{dE}{\rho\ dx} \tag{2.4}$$

Not all energy lost by the incident radiation may be deposited locally. A fraction of the incident energy can go into the generation of neutral secondary particles that can deposit their energy some distance away (for example, during a proton therapy treatment a proton can give some energy to a neutron that will deposit its energy in the room shielding).

Mass stopping power (and consequently, stopping power) can be classified into three components:

$$\frac{S}{\rho} = -\frac{1}{\rho}\left[\left(\frac{dE}{dx}\right)_{el} + \left(\frac{dE}{dx}\right)_{rad} + \left(\frac{dE}{dx}\right)_{nuc}\right] \tag{2.5}$$

The first component in equation 2.5 is called electronic or collision stopping power and comprises all the energy lost by interactions with atomic electrons resulting in ionization or excitation. The second component is the mass radiative stopping power due to bremsstrahlung and/or radiative emission near the electric atomic or nuclear fields. Finally, the third term is the nuclear stopping power due to elastic Coulomb interactions with atoms. In this work only the electronic and nuclear stopping power will be discussed due to the energies involved in particle therapy.

Electronic stopping power

The maximum energy transferred per collision to an electron, W_{max}, is generally much smaller than the total energy of charged particles, leading to a somewhat continuous slowing down of the particle in its traversal of the medium. W_{max} is described in equation 2.6:

$$W_{max} = \frac{2m_e c^2 \beta^2 \gamma^2}{1 + 2\gamma m_e/M + (m_e/M)^2} \tag{2.6}$$

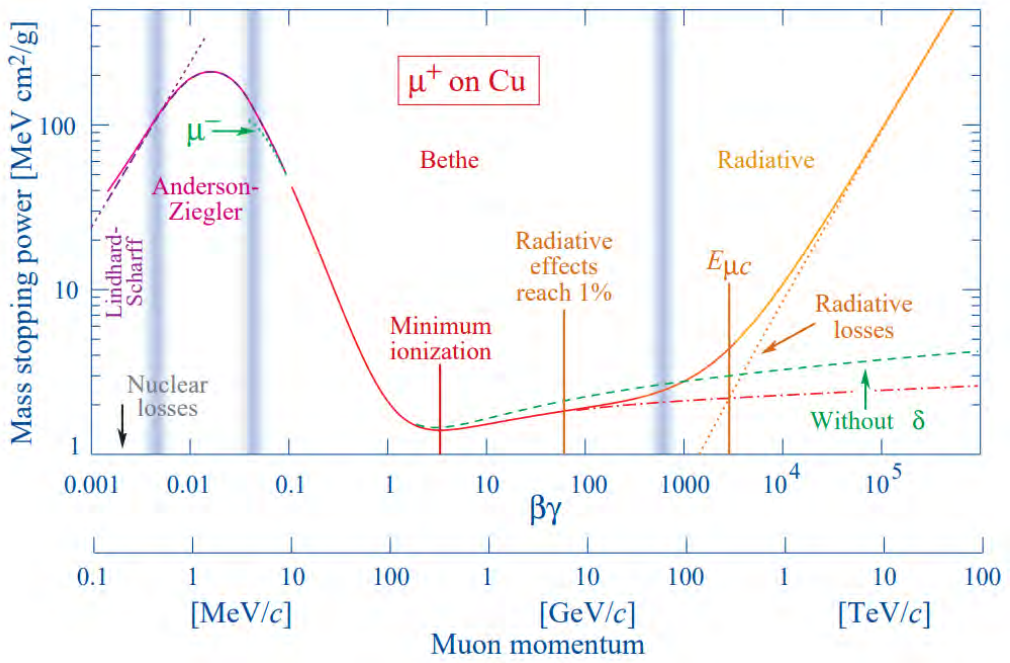

Figure 2.1: Mass stopping power of positive muons in copper as a function of the muon momentum. In the figure the different models for describing the stopping power are shown, limited by blue vertical bars and different colours. Figure taken from [23].

Where m_e is the mass of the electron, c the speed of light, β the ratio of particle velocity to c, γ the Lorentz factor of the incident particle and M the mass of the incident particle.

Depending on the incident energy of the particle the energy loss can be described by one of several models, as shown in figure 2.1. The mean electronic stopping power for moderately relativistic heavy particles can be described by the Bethe-Bloch formula and depends on the particle velocity, density of the medium and total energy of the incident particle.

$$\left\langle -\frac{dE}{dx} \right\rangle =$$
$$= 4\pi\rho N_a r_e^2 m_e c^2 z^2 \frac{Z}{A}\frac{1}{\beta^2}\left[\frac{1}{2}ln\frac{2m_e c^2\beta^2\gamma^2 W_{max}}{I^2} - \beta^2 - \frac{\delta(\beta\gamma)}{2} - \frac{C(\beta\gamma)}{Z}\right] \quad (2.7)$$

Where ρ is the medium density, N_a the Avogadro number, r_e the classical electron radius, z the atomic number of the incident particle, Z the atomic number of the medium, A the mass number of the medium, I the ionisation potential of the medium, δ the density effect correction, and C the shell correction.

The mean excitation energy employed in the Bethe-Bloch equation, I, cannot be calculated from first principles and it is often adjusted experimentally. The ratio between I and Z is more or less constant, but this does not hold always true due to atomic shell structure. "The determination of the mean excitation energy is the principal non-trivial task in the evaluation of the Bethe stopping-power formula" [23, 24].

The density effect correction in the Bethe-Bloch formula takes into account the polarisation effects present at high energies. As the electric field flattens and extends in high-energy radiation, the medium responds to this by polarising and limiting the field extension and the loss of energy by the incident radiation. This density effect is usually described by Sternheimer's parametrisation and can be widely found in the literature [25]. At higher energies the radiative effects start to dominate the energy loss and the Bethe-Bloch formula no longer holds true.

The shell correction term to the Bethe-Bloch formula considers the fact that atomic electrons of the traversed medium are not stationary and becomes important if the particle velocity is close to the orbital velocity of the atomic electrons. Shell correction is generally small, except at low energies.

As can be seen in the Bethe-Bloch formula, the loss of energy of the incident particle is highly dependent on its kinetic energy, leading to a higher energy deposition for low kinetic energies, giving rise to a sharp peak of energy loss

when the kinetic energy is at its lowest known as Bragg peak and shown in figure 1.1.

For particles with $0.1 \leq \beta\gamma \leq 1000$ this equation can describe the energy loss of the particle with an accuracy of a few percent. In the upper limit, radiative losses become more important and corrections to account for that are needed. Additional corrections to the formula can be added for low-energy incident particles that can extend the validity of $0.05 \leq \beta\gamma$, around 1 MeV in the case of protons.

If the energy loss of the particle is assumed as continuous and equal to the Bethe-Bloch equation 2.7 and any kind of energy loss fluctuation (energy straggling) is neglected, a particle range can be found by integrating the energy loss between the initial energy (E_i) and zero. This is called continuous slowing down approximation (CSDA) range, shown in equation 2.8.

$$R_{CSDA}(E_i) = \int_0^{E_i} \left(\frac{1}{\rho} \left\langle -\frac{dE}{dx} \right\rangle \right)^{-1} dE \tag{2.8}$$

On the other hand, the projected range is defined as the average value of the depth to which a charged particle will penetrate in the course of slowing down to rest. It takes into account energy and position straggling (as any interaction could cause the initial trajectory of the incident particle to vary). Depth is measured along the initial direction of the particle. The projected range will always be less than the CSDA range. The ratio between projected an CSDA range is known as the detour factor, which is bigger than 0.99 for particles with residual ranges over 10^{-3} cm in the clinical hadrontherapy beams [26].

Straggling

As stated before, Bethe-Bloch formula calculates the *mean* stopping power. There will be some deviations from this value arising from the stochastic nature of the radiation-matter interaction. As the incident radiation starts to lose energy by traversing the media it will broaden its energy, position and angle distribution.

This statistic fluctuation resulting in a different range of values for energy or range associated to each individual particle is called straggling. In the case of hadrontherapy, these distributions can be considered Gaussian. The summation of multiple scattering events yielding a Gaussian energy loss can be described [27] by equation 2.9 to account for the energy straggling:

$$\frac{N(E)}{dE}\frac{1}{N} = \frac{1}{\alpha\pi^{1/2}} exp\left[- \frac{(E-\bar{E})^2}{\alpha^2} \right] \tag{2.9}$$

This equation represents the density of probability of particles having energies in the interval (E,$E + dE$) after traversing a thickness x_0 of absorber from an initially monoenergetic beam. After the transport through a thickness x_0 the particles have a mean energy $\bar{E}$ being α the straggling parameter representing the half-width at the (1/e)-th height of the energy distribution and given by [28]:

$$\alpha = 4\pi z^2 e^4 n Z x_0 \left[1 + \frac{KI}{mv^2} ln\left(\frac{2mv^2}{I} \right) \right] \tag{2.10}$$

With n the electron density in the medium, K a constant depending on the electron shell structure varying from 2/3 to 4/3 and v the initial velocity of the heavy ion. Range straggling can also be described in a similar manner as equation 2.9:

$$\frac{N(R)}{dR}\frac{1}{N} = \frac{1}{\alpha\pi^{1/2}} exp\left[- \frac{(R-\bar{R})^2}{\alpha^2} \right] \tag{2.11}$$

Where $\bar{R}$ is the mean range. Figure 2.2 shows some range (also called longitudinal straggling) and lateral straggling values for protons and carbon ions as a function of the incident energy.

Another consequence of incident particles traversing matter is the deflection due to atomic nuclei collisions. Those angular deflections, individually, will be almost negligible, but the sheer number of them will provoke a significant deviation from the expected particle position by the end of the range. They can be

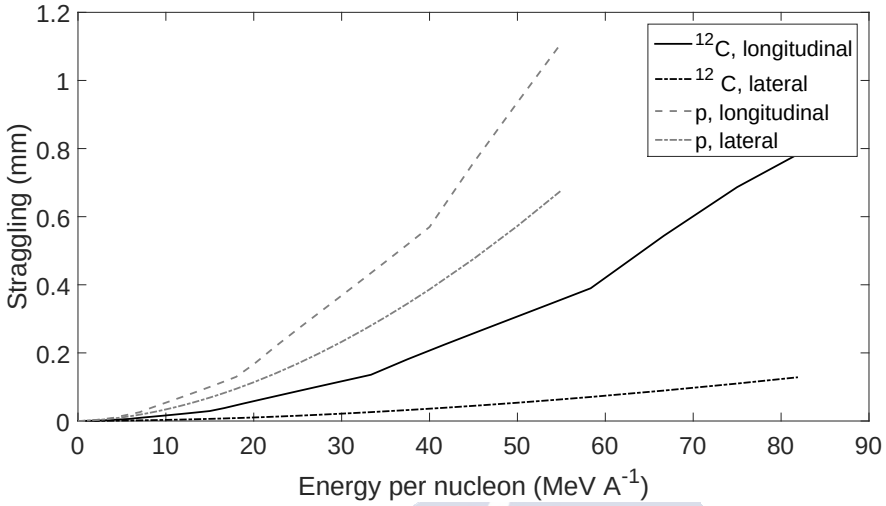

Figure 2.2: Range (longitudinal) and lateral straggling for protons and carbon ions in water as a function of the energy per nucleon of the incident particle. Data taken from SRIM [29].

thought of as a lateral straggling effect that adds to the other two mentioned before in this section.

This phenomenon is called multiple Coulomb scattering (MCS). The MCS distribution will be very close to a Gaussian one, since it is the result of a big number of small interactions that follow the Central Limit Theorem, but there also be some non-Gaussian contribution from big scatters, although with the energies used in clinical practice those contributions are almost negligible. The main models employed to describe MCS are the Highland's formula [30,31], that only considers the Gaussian contribution, and the widely used but also algebraically complicated Molière's Theory [32,33]. A thorough discussion on Molière's theory is out of the scope of this thesis, and the author would refer any interested reader to the aforementioned literature. Highland's formula only depends on the incident energy of the particle and the material traversed and can be described in the following way:

$$\theta_0 = \frac{14.1MeV}{pv}\sqrt{\frac{L}{L_R}}\left[1 + \frac{1}{9}log_{10}\left(\frac{L}{L_R}\right)\right] \tag{2.12}$$

Where θ_0 represents the standard deviation of the angular distribution (approximately Gaussian) expressed in radians. L refers to the thickness of the absorber, L_R is a material dependent parameter called radiation length that can be found in tables and pv is a term called kinematic factor and described as

$$pv = \frac{\tau + 2}{\tau + 1}E \tag{2.13}$$

with τ being the reduced kinematic energy of the particle:

$$\tau \equiv \frac{E}{mc^2} \tag{2.14}$$

2.1.2 Interaction of neutral particles with matter

Photons

There are three main mechanisms by which the photons interact with matter. Those mechanisms are the photoelectric effect, the Compton scattering and the pair production. Figure 2.3 shows the predominance of these effects as a function of the photon energy and atomic number of the absorber.

In the photoelectric effect, an incident photon transfers all its energy to an atomic electron that will escape the nucleus influence with a kinetic energy equal to the photon energy minus the atomic binding energy. In addition to the electron emission, the atom will have a vacancy in one of its shells that will be quickly filled by a re-ordination of the remaining bound electrons or the capture of a free electron. This process will emit fluorescence X-Rays. Photoelectric effect is the dominant mechanism for low energy photons and materials with high atomic number.

The Compton scattering is the interaction between a photon and an electron,

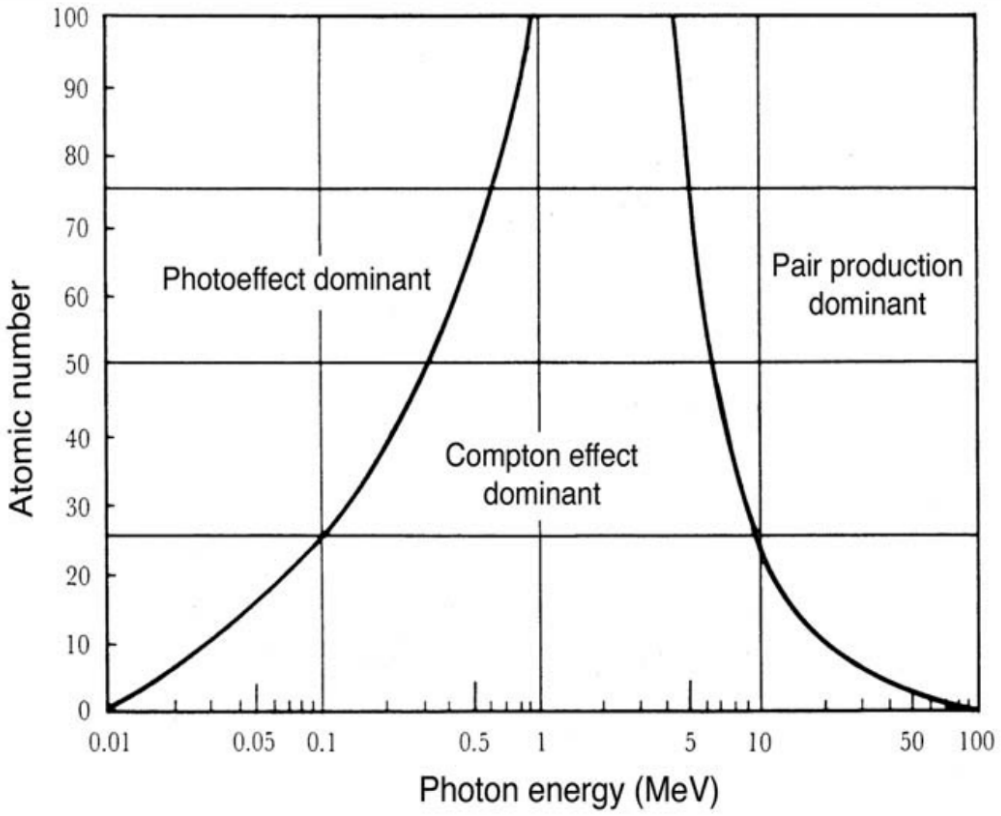

Figure 2.3: Regions of relative predominance of the three main photon-matter interactions as a function of the photon energy and the atomic number, Z, of the absorber. The left line shows where the probabilities of photoelectric effect and Compton scattering are equal. Right line shows where the probabilities of Compton scattering and pair production are equal. Figure taken from [34]

in which the photon transfers some of its energy to the electron and is deflected. This process is dominant in the keV range. The transferred energy ($E = hc/\lambda$) and the scattering angle can be found by the Compton relation:

$$\Delta\lambda = \lambda' - \lambda = \frac{h}{m_e c}(1 - cos\theta) = \lambda_C(1 - cos\theta) \tag{2.15}$$

Where $\Delta\lambda$ is the wavelength shift and $\lambda_C = h/m_e c$ is the Compton wavelength.

In pair production the photon gives up all its energy to create an electron-positron pair. For pair production in the nuclear field there is an energy threshold for it to occur equal to the sum of an electron and a positron rest mass (1.022 MeV).

Neutrons

Neutrons are highly penetrating particles since they do not interact through Coulomb force. Neutrons can propagate until they suffer a scattering or capture process mediated by the strong nuclear force. Even in the case of elastic scattering, neutrons may transfer some of their kinetic energy to recoil nuclei.

Scattering processes involve the change of momentum of the incident neutron and the target particle but do not involve a nuclear process that changes the internal structure of the nucleus. In the case of inelastic scattering, the target may reach an excited level during a brief period before emitting a gamma particle to go back to its ground state.

Lastly, absorption processes involve the capture of the neutron by a target nucleus. In the case of radiative capture, after the capture the nucleus will be in an excited state and a de-excitation gamma particle will be emitted. In a non-radiative process, the compound nucleus will emit a charged particle or a neutron. Finally, in the fission process the neutron absorption will de-stabilize the nucleus and it will divide in two daughter nuclei with approximately the same mass and the release of one or more fast neutrons that can induce fission in other nuclei.

2.1.3 Nuclear reactions

Although main stopping power contribution for beam particles comes from Coulomb interactions, in hadrontherapy nuclear interactions are very relevant, either leading to an additional effective attenuation of primary beam particles or producing secondary particles through nuclear processes. Between these secondary particles we can find fast neutrons emitted mainly in the forward direction (with

an average around 0.5 neutron per primary particle for ^{12}C beams and 0.025 for proton beams [35]) and beam particle fragments that share almost the same speed and direction of the parent particle. [36, 37]. ICRU63 [38] distinguishes three different kinds of nuclear reactions:

1. Elastic nuclear reaction: "A reaction in which the incident projectile scatters off the target nucleus, with the total kinetic energy being conserved (the internal state of the target nucleus and of the projectile are unchanged by the reaction)."

2. Nonelastic nuclear reaction: "General term referring to nuclear interactions that are not elastic (i.e. kinetic energy is not conserved). For instance, the target nucleus may undergo breakup, it may be excited into a higher quantum state, or a particle transfer reaction may occur."

3. Inelastic nuclear reaction: "Specific type of non elastic reaction in which the kinetic energy is not conserved, but the final nucleus is the same as the bombarded nucleus."

Particles created in a nuclear reaction between a primary (incident) particle and the media are called secondary particles. If a secondary particle creates a new one by means of a nuclear reaction, that new particle is classified as tertiary particle, and so on. The possible secondary particles that can be created in non-elastic nuclear reactions between a nucleus with atomic number Z and the media are all the fragments with atomic number less or equal than Z, neutrons and gamma rays.

Nuclear fragments heavier than alpha particles are quite rare but nonetheless could modify the biological dose because of their significant RBE because of the high ionisation density along its tracks, typically increasing the energy deposition beyond the range of the primary particles, as can be seen in figure 2.4.The secondary particles will typically make large angles with the beam direction axis.

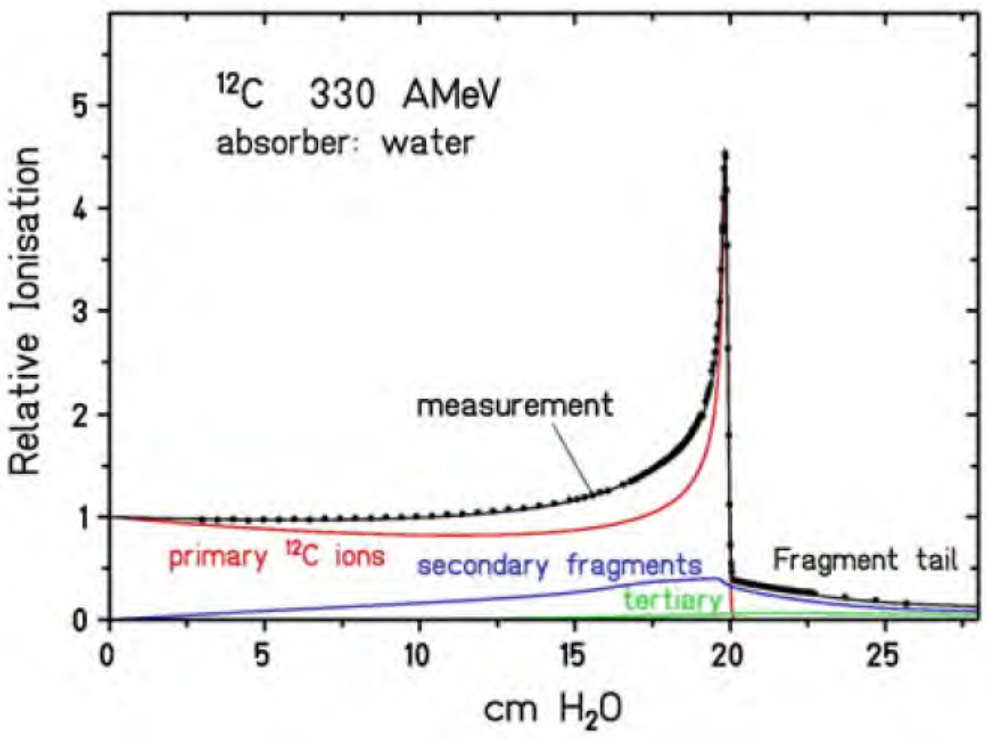

Figure 2.4: Relative ionisation of a ^{12}C ion beam along with nuclear fragments coming from primary and secondary particles. The fragments will contribute to increase the dose along the Bragg curve, specially towards and beyond the end of the range of the primary particles. Taken from [35]

2.2 Introduction to dosimetry

2.2.1 Dosimetric quantities

The amount employed to describe the quantity of energy transferred to a medium by radiation is called absorbed dose and is defined in terms of absorbed energy per unit mass of the target (J/Kg, in S.I. units) [21] as shown in the following equation.

$$D = \frac{d\bar{\varepsilon}}{dm} \tag{2.16}$$

where $d\bar{\varepsilon}$ is the mean energy imparted to a site of mass dm. The size of the site must be big enough in the macroscopic approximation to avoid statistical fluctuation of the mean imparted energy, but still as small as possible to be useful in the dose calculations. Dose is expressed in gray (Gy), and one gray is equal to one joule (J) per kilogram (kg) as stated before. Dose can also be described in terms of charged particle fluence, Φ, and mass electronic stopping power, S_{el}/ρ, as in the following equation.

$$D = \Phi \frac{S_{el}}{\rho} \tag{2.17}$$

The term imparted energy, ε, refers to all the energy deposited in a volume of study of mass dm. That is, imparted energy is the difference between the incoming energy minus the outgoing energy. The energy can be carried out by either the primary particles (particles entering the volume) or by new particles, by-product of the different reactions that occurred inside the volume. In this balance, any energy to mass conversion or vice-versa is taken into account. The equation for imparted energy is

$$\varepsilon \equiv \sum_i \varepsilon_i \equiv (R_{in})_u - (R_{out})_u + (R_{in})_c - (R_{out})_c + \sum Q \tag{2.18}$$

Where the sub-indexes in and out refer to energy entering and exiting the volume, respectively; c and u refer to either charged or uncharged particles, R is the radiant energy and finally the sum over Q represents the net energy derived from rest mass in the volume, and can be either positive or negative depending on if there is more mass transforming to energy or vice-versa [39]. Energy is transferred to the volume discretely, in the so-called transfer points inside the volume under study.

Dose alone is not useful to determine the biological effect of a given radiation. The modifications radiation does over biological media depend on the physical

conditions of the irradiation and other chemical and biological parameters. Even though the energy imparted per unit mass (absorbed dose) is important, the quality of the radiation and the temporal distribution of the energy deposition are quantities to consider when studying the effects of the radiation in the region of interest. Quality is defined here as those features of the spatial distribution of energy transfers (along and within the tracks of the particles) that influence the effectiveness of an irradiation in producing a given effect, when other physical factors such as total energy dissipated, absorbed dose, absorbed dose rate and absorbed dose fractionation are kept constant [40].

Beam quality is described by means of the Linear Energy Transfer or LET. This quantity describes the density of energy deposition in media by incident particles. The LET of a charged particle when traversing a material, of a given type and energy is defined [21] by

$$L_\Delta \equiv \frac{dE_\Delta}{dl} \tag{2.19}$$

Where dE_Δ is the mean energy lost by charged particles due to electronic interactions in traversing the distance dl minus the mean sum of the kinetic energies in excess of Δ of all electrons released by charged particles. If no energy cut-off is imposed, thus for $\Delta = \infty$, unrestricted LET, is equal to the electronic stopping power, S_{el} and denoted by L.

There are some limitations in the LET-based dosimetric analysis of the radiation beams. Rossi realised that LET is not enough to dosimetric characterise a radiation beam and specify its radiobiological effectiveness (see also section 2.4). LET is only an average value of the energy loss of a particle along the macroscopic track considered [41, 42]. The limitations of the LET analysis were the starting point of the developments in the field of microdosimetry led by Rossi and Kellerer in the 1970s. This does not mean that the LET notion must be discarded completely. In some cases an approximate evaluation of radiation quality for comparing different types of radiation is needed, and the analysis of LET distributions can fill that gap [43].

Traditionally water is used as an equivalent for tissue and in the fields of dosimetry and microdosimetry the relevant quantities are often referred to the ones in water to allow a better comparison of the results. The water equivalence of a material can be computed if the range-energy relations or the stopping power ratios between such material and water are known. If a material is significantly different in effective atomic number to the one of water the relation becomes more complicated. In the case of energies and materials used traditionally in clinical microdosimetry there is enough literature to convert microdosimetric spectra between materials.

This is not the case for silicon. Microdosimetric spectra from silicon are hard to convert to spectra from tissue-equivalent materials because of the difference in stopping power, specially at low energies. Traditionally this has been done through the use of a single conversion factor [44] with relative success, but recently new methods have been proposed to make this conversion more accurate [45, 46].

2.3 Microdosimetry

In the previous section it was discussed that for absorbed dose definition the site should have a size big enough to avoid the statistical fluctuation of the mean imparted energy, but what would happen if the size of the volume is too small to fulfil this condition, as when studying the behaviour of a single cell or a molecule during its irradiation?

Although the mean imparted energy is a good indicator of the energy deposition over a volume the microscopic distribution and the pattern of energy deposition at microscopic scales also is very important in order to assess the biological damage produced by ionising radiation. Effects depend on the pattern of the energy deposition in media [17]. Microdosimetry, as conventional dosimetry, also uses equation 2.18 as a starting point but considers statistical fluctuations to this quantity due to the stochastic nature of the radiation-matter interaction. Both matter (made of atoms) and radiation (composed by radiation quanta) can be described as discrete structures that can individually cause fluctuations in

physical processes. Usually, outlier values departing from the mean can be ignored due to being negligible in the calculations, but in the case of radiation, where only one particle or one single ionisation process can produce dramatic effects in the site under study, statistical fluctuations play a key role and must be considered. Thus, microdosimetry uses the approach that all the relevant dosimetric quantities follow a certain probability distribution.

2.3.1 Microdosimetric quantities

If a point within the volume described in equation 2.18 is chosen, the corresponding microdosimetric stochastic quantity to describe the energy imparted per unit mass, or specific energy, z, is described by the following equation

$$z \equiv \frac{\varepsilon}{\rho V} = \frac{\varepsilon}{m} \tag{2.20}$$

where ρ is the medium density and V its volume. By decreasing the volume of the site, V, the variance of z would increase and due to the stochastic nature of radiation there is a growing probability that z would equal zero since there may be no transfer points inside the region under study, so knowledge about the volume is important in microdosimetry. At large enough volumes, the mean value of the specific energy probability distribution, $\bar{z}$, is equal to the mean value of the macroscopic absorbed dose, $\bar{D}$.

The microdosimetric analogue to linear energy transfer (equation 2.19) is called lineal energy, y, and is defined by the following equation:

$$y \equiv \frac{\varepsilon_1}{\bar{l}} \tag{2.21}$$

Where the sub-index in the imparted energy means that the energy is imparted in a single event, and $\bar{l}$ is the mean chord length of the volume, that is, the average length traversed by the particles inside the volume. This single-event distribution can also be made for the case of specific energy. It is easy to see why this quantity is the microdosimetric equivalent of LET, as both have units

of energy over length.

From now on this dissertation we will be referring only to single event distributions and the sub-index in equation 2.21 will be dropped.

The probability that the lineal energy will be in an interval $[y, y+dy]$ is $f(y)dy$. Analogously, the probability that the specific energy will be inside the interval $[z, z+dz]$ is $f(z)dz$. Once the probability distributions $f(y)$ and $f(z)$ are known, their momenta can be calculated. The first momenta of this microdosimetric quantities are called frequency (or fluence) averages.

$$\bar{z}_F = \int_0^\infty z f(z) dz \tag{2.22}$$

$$\bar{y}_F = \int_0^\infty y f(y) dy \tag{2.23}$$

The dose weighted distribution (or microdosimetric dose distribution) can be calculated from the fluence distributions and their first momenta.

$$d(z) = \frac{z f(z)}{\bar{z}_F} \tag{2.24}$$

$$d(y) = \frac{y f(y)}{\bar{y}_F} \tag{2.25}$$

The ratio between the second and first momenta of the specific or lineal energy are equal to the first moment of the dose averaged distributions.

$$\bar{z_D} = \frac{1}{\bar{z}_F} \int_0^\infty z^2 f(z) dz = \int_0^\infty z d(z) dz \tag{2.26}$$

$$\bar{y_D} = \frac{1}{\bar{y}_F} \int_0^\infty y^2 f(y) dy = \int_0^\infty y d(y) dy \tag{2.27}$$

One of the main problems with microdosimetry is how to display graphically the data. Both the microdosimetric quantities and their probability distributions

may span a large spectrum of values. In some cases, they can span up to eight orders of magnitude, so the use of a linear-linear plot is not advisable. In order to be able to estimate the fraction of events that have a given lineal or specific energy value a special semi-logarithmic representation called microdosimetric spectra is used. For example, for lineal energy this representation plots $y\ f(y)$ against $log(y)$.

The reasoning behind that representation is that the area delimited by any two values of y is proportional to the frequency of events that have lineal energy in that range of lineal energy values and the details at low energy are no longer concealed by the linear representation in the plot, as the following relation shows

$$\int_{y_1}^{y_2} f(y)dy = \int_{y_1}^{y_2} [yf(y)]d[log(y)] \tag{2.28}$$

For the representation of the dose distributions the reasoning is the same, with the area between two values of lineal energy showing the dose delivered in that range.

$$\int_{y_1}^{y_2} d(y)dy = \int_{y_1}^{y_2} \frac{yf(y)}{\bar{y}_F}dy = \frac{1}{\bar{y}_F}\int_{y_1}^{y_2} [y^2 f(y)]d[log(y)] \tag{2.29}$$

The reasoning is analogous in terms of specific energy, z.

2.3.2 Chord length estimation

Mean chord length can be obtained from the chord length probability density, $g(l)$ of the particle tracks across the site. In the case of a convex body, this distribution can take several forms [47]. For a convex body, K, there are five principal random distributions, with the three more important being the following:

1. Surface radiator randomness (S-randomness): The track is defined by a point in the surface of the volume K and a direction from independent uniform distributions.

2. Interior radiator randomness (I-randomness): The track is defined by a point inside the volume K and a direction, from independent uniform distributions.

3. Mean free path randomness (μ-randomness): A chord of a convex body K is obtained by the intersection of this body and a straight line defined by a point in Euclidian space and a direction. The point and the direction are from independent uniform distributions. This randomness results if the convex body is exposed to a uniform, isotropic field of straight infinite tracks.

Kellerer [43] studied the problem of the lineal energy distribution and obtained a general solution, providing that these two mutually exclusive conditions are fulfilled: 1-In the case of neutron radiation, their energies are high enough so that most of the recoil tracks are long compared with the dimensions of the site and 2- the stopping power of the particles and the diameter of the region are large enough that energy loss straggling and efflux and influx of δ-rays can be neglected.

If a site, U, is randomly traversed by charged particles (μ-randomness general case). There is a distribution of chord lengths (l) traversed by the charged particles, $g(l)$. The distribution of lineal energy[1] is $t(L)$.

The energy, E, deposited in U during a traversal is the product of the two independent variables l and L. The distribution of energies, $f(E)$, is experimentally determined. Also, the chord length distribution, $g(L)$ can be estimated from geometrical conditions and particle radiance models, and the lineal energy distribution, $t(L)$ has to be derived. The cumulative probability distributions obtained from the probability densities use the same letters capitalised, e.g. $F(E)$ is the probability that the energy deposited by the traversal of one charged particle in the site is equal or less than E, as shown here:

[1]Kellerer calls this LET, but since he uses a chord length distribution we will use the more modern terminology and call it lineal energy. The mathematical formulation remains unchanged.

$$F(E) = \int_0^\infty t(L)G(E/L)dL \tag{2.30}$$

And $G(L)$ being the cumulative distribution function of $g(l)$:

$$G(L) = \int_0^\infty g(l)dl \tag{2.31}$$

By differentiating with respect to the energy:

$$f(E) = \frac{dF(E)}{dE} = \int_0^\infty t(L)g(E/L)\frac{dL}{L} \tag{2.32}$$

Kellerer provided a solution for the special case of a sphere of diameter d with the following chord length distribution:

$$g(l) = \frac{2l}{d^2} \quad l \leq d \tag{2.33}$$

Then, equation 2.32 can be written as

$$f(E) = \frac{2E}{d^2}\int_{L=\frac{E}{d}}^\infty t(L)L^{-2}dL \tag{2.34}$$

and, by differentiating

$$\frac{1}{E}\frac{df(E)}{dE} - \frac{f(E)}{E^2} = -\frac{2t(E/d)}{dE^2} \tag{2.35}$$

and, therefore

$$t(L) = \frac{d}{2}\Big[-E\frac{df(E)}{dE} + f(E)\Big] \quad with \;\; E = Ld \tag{2.36}$$

Figure 2.5, taken from [43] represents the experimental pulse height distribution, along with the chord length distribution to obtain the lineal energy (LET in the figure) distribution. The measurements were taken with a spherical propor-

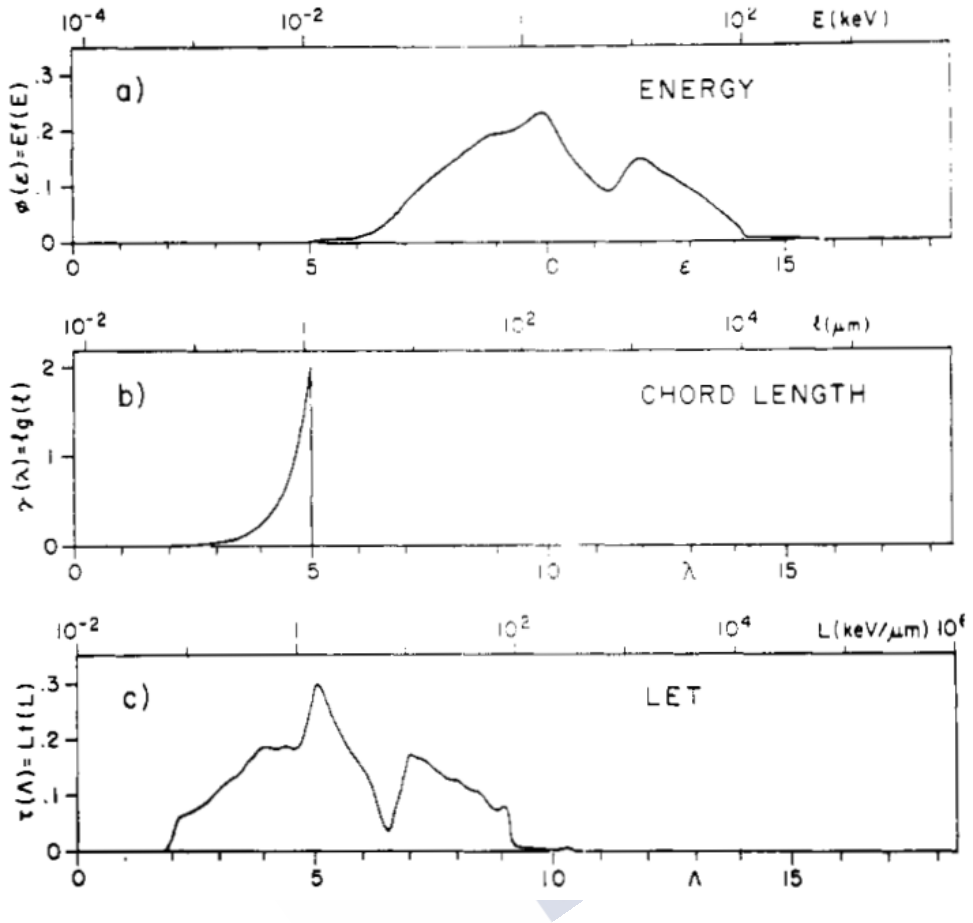

Figure 2.5: Energy deposition spectrum (a), along with the chord length distribution (b), $lg(l)$ in the sphere, and the obtained lineal energy distribution (c) obtained with the method described above. The convolution of (a) and (b) gives (c). Taken from [43]

tional counter exposed to a mixed radiation field of 3.7 MeV neutrons with a γ-ray component. For general chord length distributions, the resolution of equation **??** may be obtained by iterative or Fourier transform methods.

For convex and regularly shaped structures, under μ-randomness, the mean chord length can be described in terms of its surface S and volume V using the Cauchy formula

$$\bar{l} = \frac{4V}{S} \tag{2.37}$$

In the case of a beam of particles with almost parallel trajectories and coming from a fixed point in the space outside the volume of interest the situation is far from μ-randomness. Additionally, in the case of the planar detectors used in this dissertation, the incidence is perpendicular to the active surface and the thickness of the detector is much less than the range of the primary particles. Thus, the thickness, h, can be used as the mean chord length value due to the high directionality of the radiation field produced [45]. A correction factor, $k_y(\Delta)$, can be calculated to consider the divergence between the dimensions of the detector and the mean chord length.

$$\bar{l} = \int_0^{l_{max}} l g(l) dl \approx h \; ; \qquad y = \frac{\varepsilon}{\bar{l}} \approx \frac{\varepsilon}{h} k_y(\Delta) \tag{2.38}$$

$$k_y(\Delta) = \frac{h}{\int_0^{l_{max}} l \; g(l) \; dl} \tag{2.39}$$

The correction factor described in equation 2.39 can be calculated using Monte Carlo methods and generally $k_y(\Delta)$ close to unity for all points up to the Bragg peak. For example, let us take a cylinder with height equal to its diameter, $L = 20$ μm, and irradiated with protons with an initial kinetic energy of 50 MeV. Through the use of a Monte Carlo code (in this case the Monte Carlo code SRIM was employed [29]), different chord length distributions can be calculated. Those values can be compared with the mean chord length in the case of μ-randomness for this scenario, 13.3 μm. Figure 2.6 shows the mean chord length in the case of perpendicular incidence to the bases of the cylinder for different depths in water. The correction factors for planar fluence for this example were calculated and shown in figure 2.7.

By turning the cylinder around an axis parallel to its bases the chord length angular dependence can be calculated. This is shown in figure 2.8 for a depth in water of 19 mm. At this depth, the rms value for the angle of the proton tracks

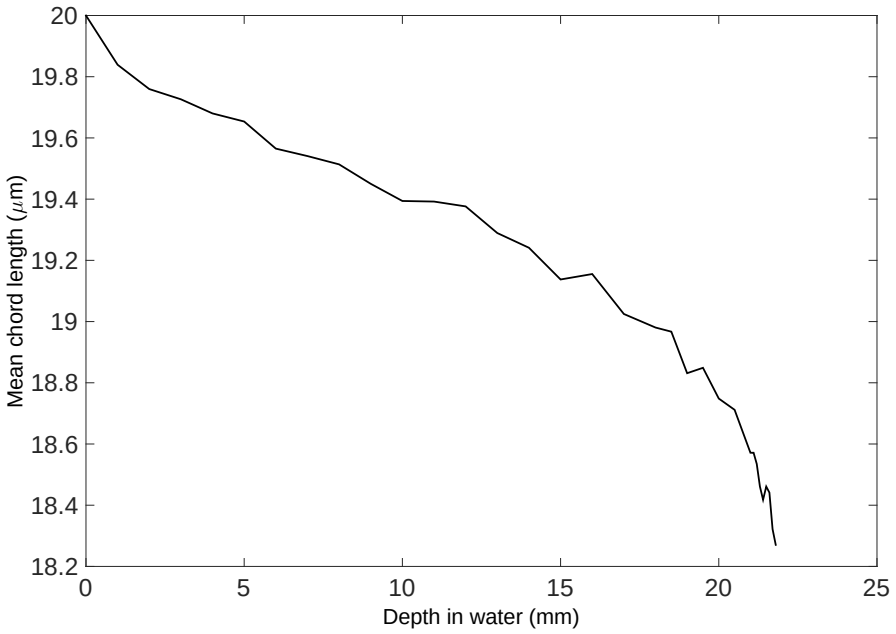

Figure 2.6: Mean chord length in the case of protons with initial kinetic energy of 50 MeV and perpendicular planar fluence with respect to the base of a cylinder with height and diameter L=20 μm for different depths in water.

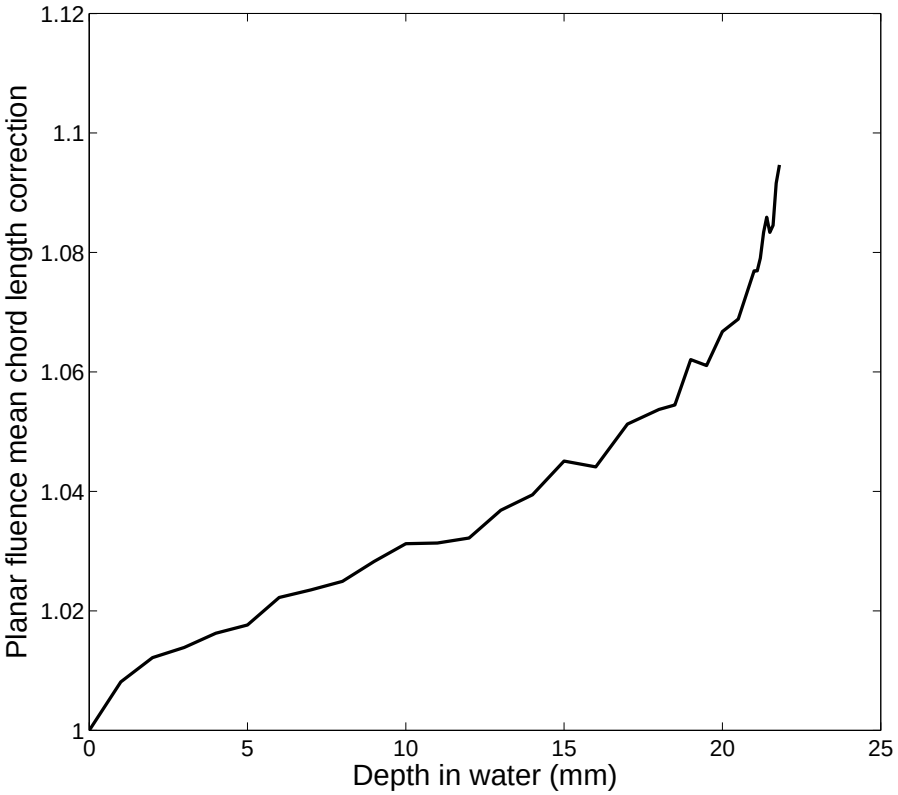

Figure 2.7: Mean chord length correction factor in the case of protons with initial kinetic energy of 50 MeV and perpendicular planar fluence with respect to the base of a cylinder with height and diameter L=20 μm for different depths in water.

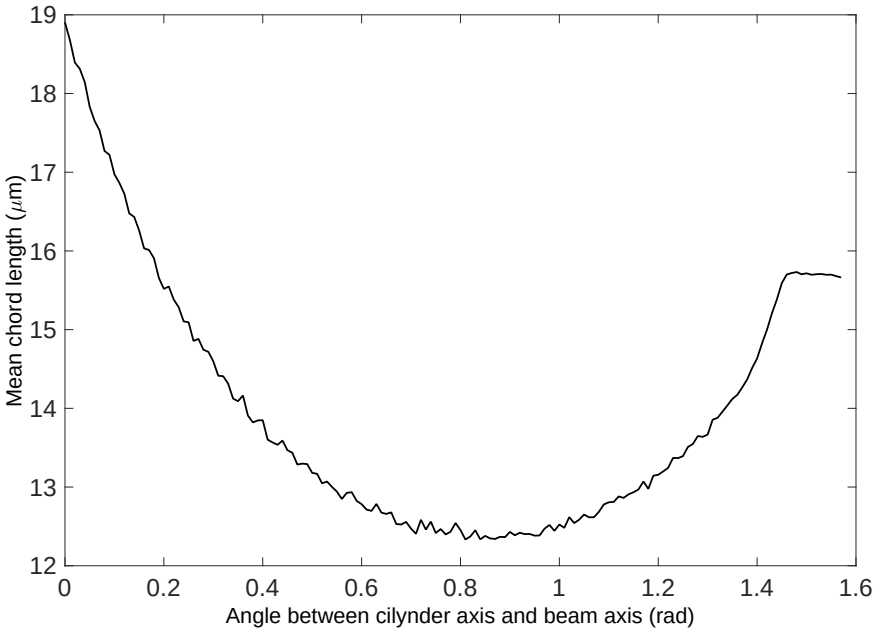

Figure 2.8: Mean chord as a function of the angle between the bases of the cylinder and the initial axis of propagation of protons with an initial kinetic energy of 50 MeV after traversing 19 mm of water.

with respect to the original perpendicular incidence axis is around 40 mrad.

2.4 Radiobiology

Radiobiology studies effects of ionising radiation on biological tissue through the analysis of mechanisms involved in the interaction of incident radiation on cells and the subsequent biochemical responses.

One of the ways to summarize the damage done by an agent (radiation, chemicals, etc.) to cells, is the determination of their survival probability as a function of delivered dose. Usually, the survival curve follows a sigmoid, with a shoulder followed by an asymptotic approach to zero with increasing dose. The cell sensit-

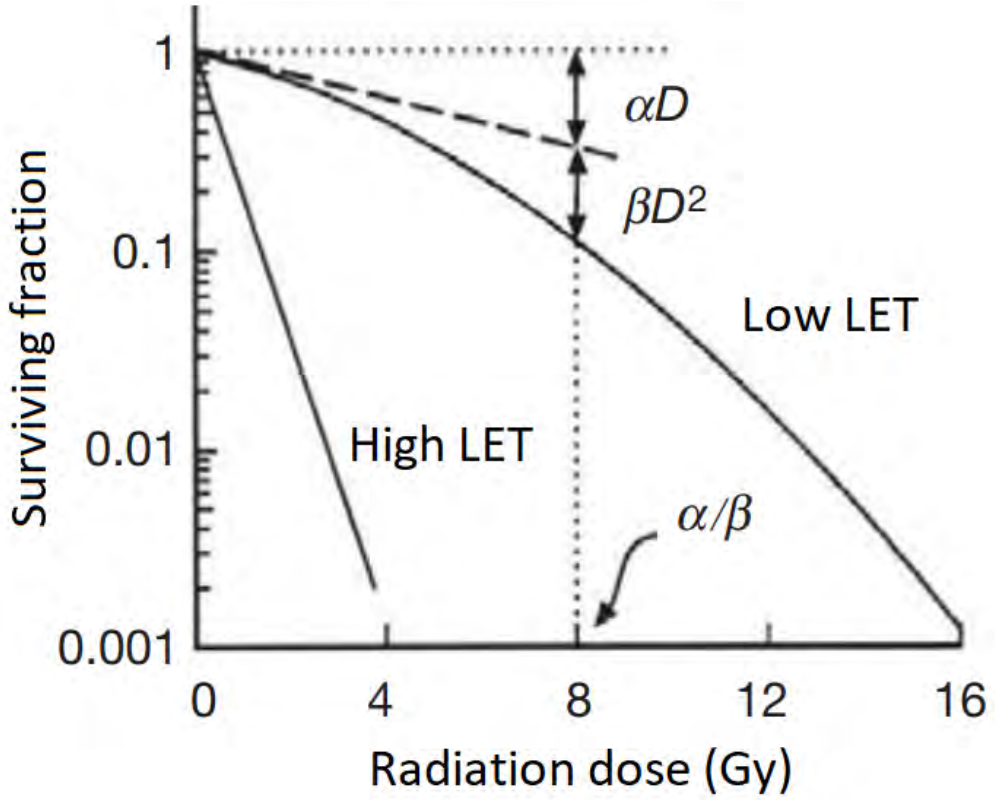

Figure 2.9: Number of surviving cells as a function of dose for low and high LET radiation. The different contributions from the two parameters from the lineal-quadratic model are shown. Graph taken from [34]

ivity to radiation is indicated by the dose needed to reach a certain survival level (e.g. the dose needed to obtain a surviving fraction of 0.5). Figure 2.9 shows the survival fraction of a typical cell culture when irradiated with high and low LET radiation.

These curves can be fitted to a two-parameter model termed lineal-quadratic (LQ) model [48], also shown in figure 2.9. The formula for the model that gives us the probability, $p(S)$, of a given survival fraction,S, is:

$$-ln(S) = \alpha D + \beta D^2 \tag{2.40}$$

$$p(S) = e^{-(\alpha D + \beta D^2)} \tag{2.41}$$

For a given type of radiation and tissue the ratio α/β denotes the dose value at which the linear and quadratic components have an equal contribution, and the shape of the curve also depends on this ratio. For highly ionising radiation the α/β ratio is usually high, i.e. the decay is purely exponential with small quadratic contribution.

Relative Biological Efficiency, or RBE, allows to compare the effectiveness of a certain type of radiation with respect to a standard radiation, usually ^{60}Co gamma rays or 250 keV X-rays [48]. This is done by comparing the doses needed to provoke the same effect (i.e. a determined cell survival ratio) following this relation:

$$RBE \equiv \frac{D_{std}}{D_{test}}\bigg|_{isoeffect} \tag{2.42}$$

In the equation 2.42, the subindex 'std' refers to the standard radiation quality, and 'test' to the radiation quality of interest for which the RBE is calculated.

RBE is not only dependent on the physical properties of the particle (dose rate, total dose, fractionation, particle type and velocity, LET), but also in biological properties (end point, oxygen concentration and cell-cycle phase) [12].

2.4.1 Relation between LET and RBE

As LET increases towards 100 $keV/\mu m$, RBE also increases but once over that point, the RBE starts to decrease again. This is defined as cell overkill, that is, the dose deposited in a single cell is more than enough to kill it, wasting radiation in the process.

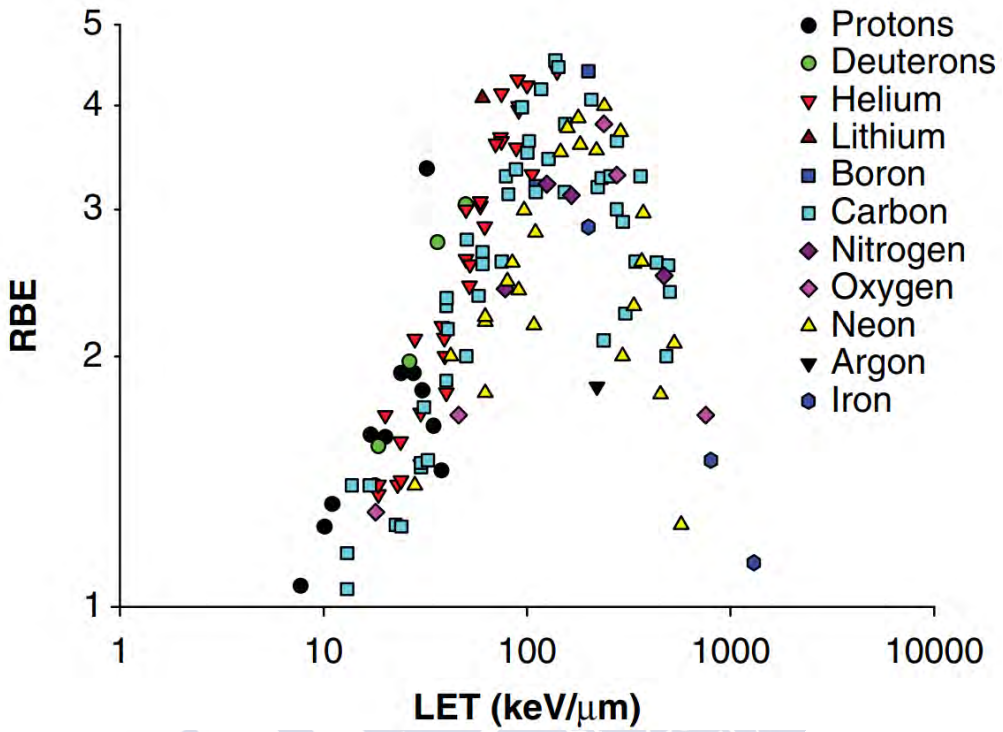

Figure 2.10: Comparison of RBE values from V79 cells for different radiation qualities as a function of LET for the biological endpoint 10% survival in colony formation. Figure taken from [49]

Figure 2.10 shows the RBE values for V79 cells for 10% survival colony formation as a function of LET for different particles. Protons can have similar RBE to photons (RBE around 1) even though their LET is higher, but their radiobiological properties are almost the same. Heavier particles like Carbon ions, on the other hand, offer values of RBE up to 5.

In treatment planning, the RBE is used to transform the physical dose into a biological or RBE-weighted dose that considers not only the amount of radiation delivered to the target, but many biological factors as discussed earlier. RBE must be defined by using complex models instead of the use of a single factor. There are different RBE models based on *in vitro* data that are used in different particle therapy installations around the world [50–54].

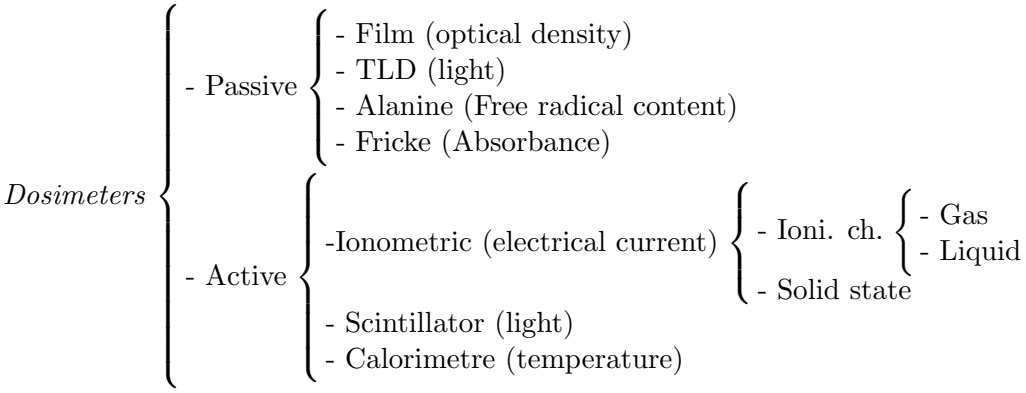

Figure 2.11: Dosimeters classified in terms of on (active) or off-line (passive) readout. For each type of dosmieter, the main physical property employed for the radiation measurement is shown between parentheses. Ioni. ch. is an abreviature for ionisation chamber.

2.5 Dosimeters

There is a wide array of detectors to be used in dosimetry and microdosimetry, each one employing different physical effects of radiation interaction with matter. A classification of dosimeters can be made by putting them into two broad groups: Active dosimeters have to be read in real time, whereas passive dosimeters do not show that capability. Figure 2.11 show an array of different dosimeters. In this work, we will cover exclusively silicon detectors, a sub-set of the solid state detectors shown in the figure.

An ideal dosimeter should follow these characteristics:

- Offer an accurate and precise measurement.
- Linear dose response
- No dose rate dependence
- No energy dependence
- No directional dependence

- Small size
- Small spatial resolution
- Ease of use and readout

An ideal dosimeter showing all these characteristics is not available. A compromise must be done to ensure the correct tool is used for its intended work amongst the panoply of different detectors available.

To obtain the experimental data for RBE and radiobiological calculations mentioned before, adequate instrumentation for the measurement of the microdosimetric quantities is needed. Traditionally the most common instrumentation in the field of particle therapy were tissue equivalent gas filled proportional chambers or TEPC. These devices work by measuring the ionization in a macroscopic volume that can be translated to a microscopic one by varying the gas density inside the chamber.

Gaseous detectors work by collecting the ion-electron pairs formed by ionizing radiation between two electrodes with an electrical potential difference between them. The measured charge is a function of the applied voltage between the electrodes, and its sensitivity will depend on the pressure of the gas and the electronic readout system. Depending on the applied potential between the electrodes different modes of operation can be used, shown in figure 2.12.

The first region employed in gaseous chambers is the ion chamber region (region I in figure 2.12). Here, the incident radiation will create electron-ion pairs that will modify the electric charge from the electrodes, with the accumulated charge (and the readout) being proportional to the ionisation in the chamber.

By augmenting the potential between the electrodes, the detector will work in the proportional chamber region (region II in figure 2.12), where due to the relatively high electric field present there will be multiplication effects of the created charge inside the gas, with the collected charge being proportional to the energy deposited inside the measuring volume.

The third region used and the one with the highest electrical potential between

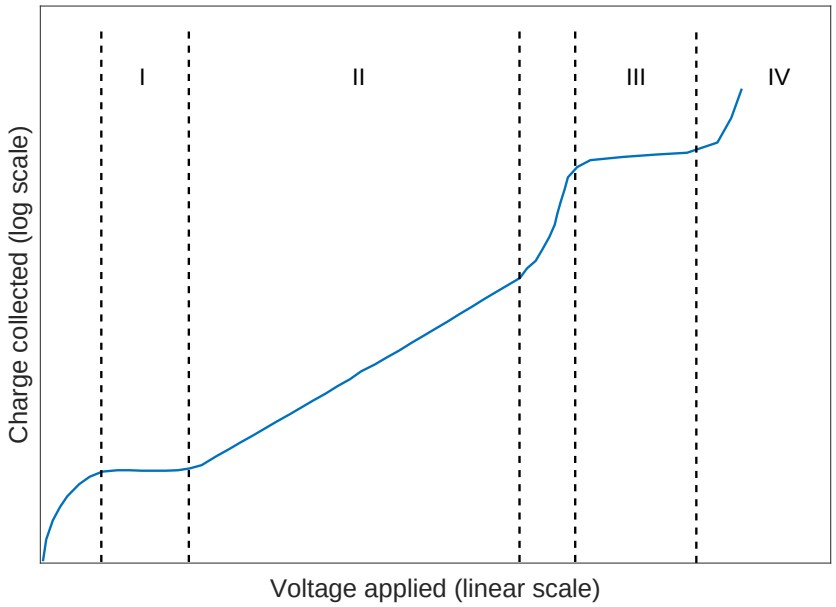

Figure 2.12: Sketch of different modes of operation of a gaseous detector as a function of the applied voltage between the electrodes. I: Ion chamber region II: Proportional chamber region III: Geiger-Müller region IV: Region of continuous discharge. The unnumbered regions and region IV are not used in radiation detection.

the electrodes is the Geiger-Müller region (region III in figure 2.12). In this mode of operation, the readout pulses will have the same amplitude regardless of the energy deposition inside the volume. G-M detectors will work as radiation counters.

By applying even more voltage, the region of continuous discharge (region IV in the figure 2.12) makes the device incapable of provide a reading.

Solid-state detectors provide numerous advantages for radiation detection. Using a solid medium means that the dimensions of the device could be kept smaller than an equivalent gas-based detector with respect to primary ionization signal, as densities of solid media are approximately one thousand times bigger

than gaseous media.

There are several types of active solid-state detectors, such as scintillators, semiconductor based detectors, etc. Solid-state detectors also have problems of their own depending on their technology and design. For example, scintillators have moderate energy resolution as there are several inefficiencies in the process of converting imparted energy in the detector to light and then to electric signal in a coupled photo-detector. The energy needed to create one photoelectron is around 100 eV, so there will be few photoelectrons per event resulting in relevant statistical fluctuations in the recorded signal.

One way to overcome this problem is to increase the number of information carriers by lowering the threshold energy to create one. Semiconductors can fulfil that role as the energy necessary to create an information carrier (in this case, electron-hole pairs that are analogous to electron-ion pairs in gaseous detectors) is in the order of the electronvolts.

2.5.1 Tissue equivalent proportional counters (TEPC)

TEPCs are the most common device for microdosimetry calculations, developed by Rossi in the 1950s [55, 57]. Any ionisation produced in the volume will be collected by means of a central anode and cathode walls. Both the gas employed in filling the chamber and the walls are tissue equivalent, with propane and methane gas mixtures usually employed and with the walls built using tissue-equivalent materials, as conductive plastic A-150 that mimics the composition of muscular tissue [58, 59].

As its name implies, these gaseous detectors work in the proportional zone. The voltage employed must be carefully chosen in function of the gas and its density inside the TEPC volume. TEPCs show an excellent energy sensitivity compared with other types of detectors used in microdosimetry, with a minimum detectable lineal energy of around 0.05 keV/μm [44].

On the other hand, the main disadvantage of the TEPCs is the so-called wall effects that cause distortions in the reading. These effects occur due to scattering

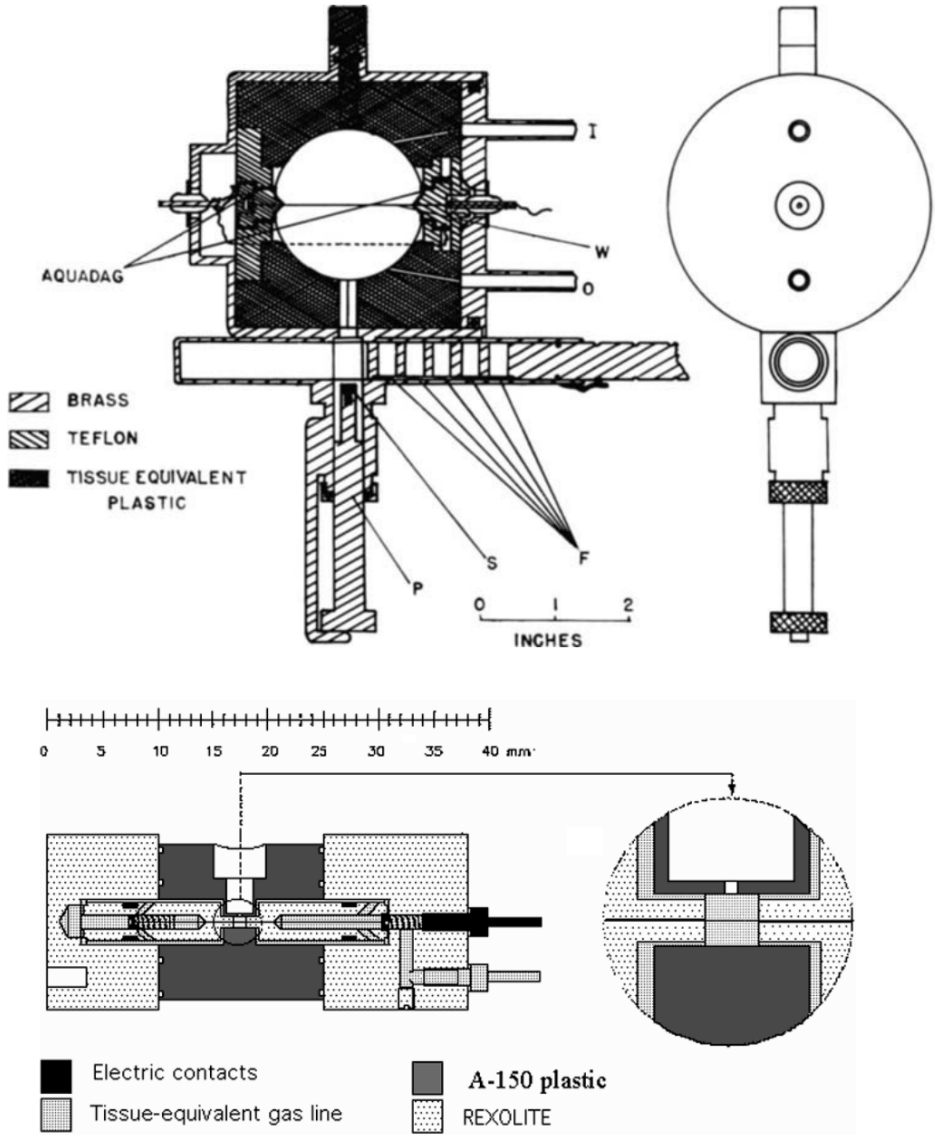

Figure 2.13: Schematic of a macroscopic sized TEPC as the ones developed by Rossi in the 1950s [55] (top), along with the more recent mini TEPC from Legnaro National Laboratories [56] (bottom).

effects of the particles traversing the wall of the device because of the difference in density between the wall and the low-pressure gas. This inhomogeneity will alter the electronic equilibrium because of the different distribution of delta rays produced in the wall and the active area, modifying the microdosimetric spectra. TEPCs also have very little spatial resolution due to its macroscopic size, only capable of mimicking one single isolated cell and show pile-up effects under beams of clinical intensity (10^8 particles s^{-1} cm^{-2}). Finally, are difficult to operate due to the high voltages involved in their operation and the difficulty of moving the experimental apparatus.

Despite all those drawbacks, TEPCs are the microdosimetric battle horse, with several applications of these kinds of detector around the globe [60–62] and even aboard the International Space Station (ISS) and space shuttle for radiation protection [63].

Recent developments have been made for TEPC miniaturisation. New miniaturized TEPCs are under development nowadays with a much smaller volume than traditional TEPCs capable of operate in clinical beams without noticeable pile-up effects [56, 64, 65]. Figure 2.13 show a schematic of those devices along with the more traditional ones.

2.5.2 Solid-state detectors

Solid-state detectors offer desirable features to be used as a detector: not only the detector would have high energy resolution and a small size, but also it would lack the need of using a high voltage source to operate and offer fast signal processing. The main disadvantages a semiconductor detector could have are the limitation to small sizes (a large semiconductor detector would be costly) and the high susceptibility of the material to radiation damage.

The first use of a semiconductor as a radiation detector was performed by McKay in 1951 [66] to detect alpha particles employing a germanium PN-diode and since then the use of semiconductors as radiation detectors has extended to nuclear physics, medical imaging, non-destructive testing, dosimetry, etc.

Currently, most semiconductors in use as radiation detectors are composed of crystalline silicon or germanium due to their carrier transport properties allowing the use of larger surfaces without the loss of carriers due to trapping or recombination processes. Another promising material for solid-state radiation detectors is diamond since it is more radiation resistant than silicon or germanium but is more expensive than the other two materials and has limited availability. Diamond would be a very good candidate for a medical physics radiation detector since its atomic number (Carbon, Z=6) is closer to the effective atomic number of tissue (Z=7.4) more than silicon (Z=14) or germanium (Z=32). Its main drawback is the high mean energy per electron-hole pair when compared to the other two, being significantly higher, leading to a lower number of charge carriers affecting the signal.

Compound semiconductors are also used, as mixing different elements can yield an array of stopping powers and band gaps. The main disadvantages of using compounds is that they have a higher density of traps than the elemental semiconductors described in the previous paragraph. The most common compound semiconductors come from groups IIIA and VA (i.e. GaAs), also called type P doping, and II and VIA (i.e. CdTe), or type N doping.

As most atoms of the IVA group, silicon forms a covalent crystal by bonding with four other neighbours by means of a covalent bond using the four outermost electrons of its atomic shell. This periodic crystalline lattice establishes allowed energy bands for electrons within the lattice. The energy of any electron within the crystal is confined to these energy bands, and these allowed energy bands can be separated by ranges of forbidden energy called gaps. Figure 2.14 represents the bands of interest in a semiconductor.

The full band represents the lower energy bands of the semiconductor, and is of no interest for radiation detection. Next,the valence band, comprises the outer-shell electrons from atoms within the crystal in covalent bonds. The high-energy band in the other side of the gap is the conduction band and represents electrons not bonded to any single site within the lattice that can move through the crystal. These electrons contribute to the electrical properties of a semiconductor.

	Diamond	**Si**	**Ge**
Atomic Number	6	14	32
Atomic Weight	12.01	28.09	72.60
Density $(g\ cm^{-3})$	3.51	2.33	5.32
Dielectric constant (relative to vacuum)	5.7	11.9	16.2
Gap energy (300 K) (eV)	5.47	1.12	0.66
Intrinsic carrier density (300 K) (cm^{-3})	$< 10^3$	$1.4\ 10^{10}$	$2.4\ 10^{13}$
Intrinsic resistivity (300 K) $(\Omega\ cm)$	$< 10^{12}$	$2.3\ 10^5$	47
Electron mobility (300 K) $(cm^2\ v^{-1}\ s^{-1})$	1800	1450	3900
Hole mobility (300 K) $(cm^2\ v^{-1}\ s^{-1})$	1200	450	1900
Mean energy per e^--h^+ *pair (300 K, 77 K for Ge)* (eV)	13.1	3.63	2.96

Table 2.1: Properties of diamond, intrinsic silicon, and germanium. Data taken from [68].

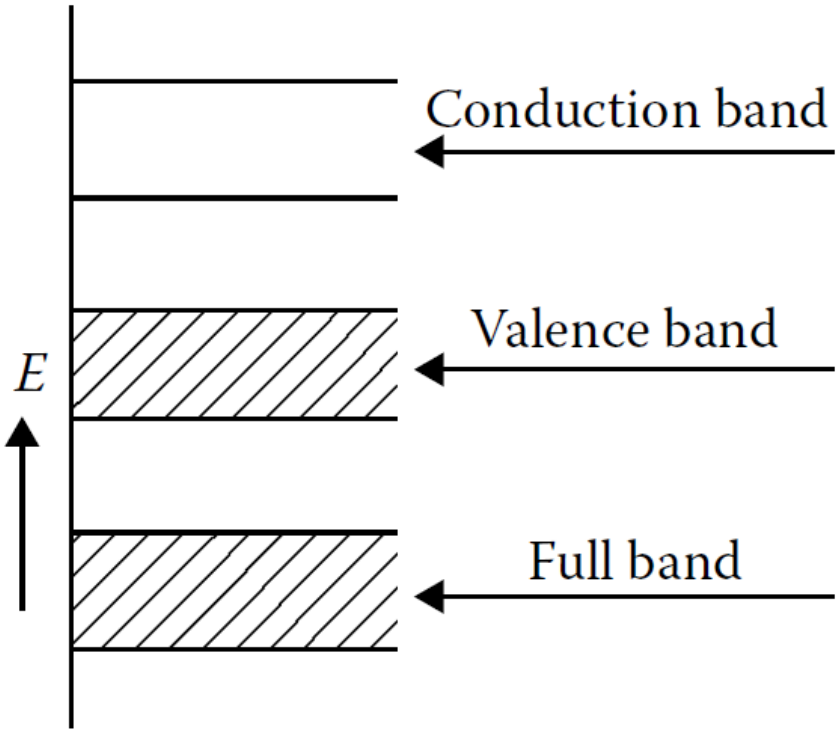

Figure 2.14: Band structure for electron energies in a semiconductor. The bands of interest are the valence band, where the positive charge carriers can move freely through the lattice, and the conduction band, where the electrons can move freely through the lattice. Taken from [67]

The size of the gap defines the electrical behaviour of the material and is used to classify the material as an insulator (high gap energies) or a semiconductor (low gap energy). The number of electrons in a lattice fills all available sites in the valence band.

Therefore, at 0 K there would not be any electron occupying the conduction band and the semiconductor would behave as an insulator. It is due to thermal excitations that the electrons can jump from the valence band into the conduction band taking advantage of the low energy of the gap between the two. In the case of conductors, the band of highest energy is not fully occupied, and the electrons

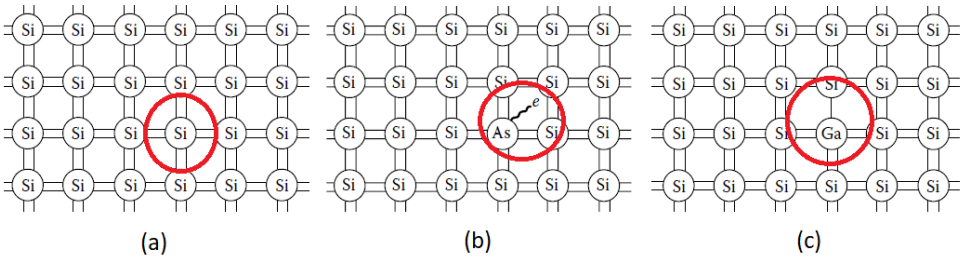

Figure 2.15: Representation of the bonds in a silicon lattice. (a) - Intrinsic silicon. (b) - N-type silicon, doped with impurities with 5 electrons in the valence band, as As. The fifth electron is not tightly bound and can the energy needed to move it to the conduction band is small. c- P-type silicon, doped with impurities containing 3 electrons in the valence band, as Ga. One of the covalent bonds in the lattice is not matched. Taken from [67]

can jump through the atoms as they need very little energy to do so.

The jump of an electron into the conduction band will create a vacancy in the valence band (a hole). This pair (electron-hole) is the equivalent of the ion pair in gases, as the electron in the conduction band can be moved by applying an electrical field to the material, but the hole, behaving as a net positive charge would also move but in the opposite direction. These movements contribute to the conductivity of the material. Table 2.1 shows some properties of diamond, intrinsic silicon and germanium. Data is taken from [68]

In an intrinsic semiconductor (like pure silicon) all the conductors would be generated by thermal excitation and every electron in the conduction band would leave a hole in the valence band. To improve the conduction in one of the bands some impurities can be added. This process is called “doping” the material. By adding impurities from groups IIIA or VA, one can have an excess of holes (p-type silicon) or electrons (n-type silicon), respectively. Figure 2.15 shows a schematic representation of the bonds in intrinsic, n and p-type silicon.

The traversal of a charged particle through the semiconductor volume will create a high number of hole-electron pairs along its track picoseconds after the interaction between the radiation and the detector. This process can be done by

direct or indirect ionisation, meaning that the energy will be imparted through a mediator particle (electrons ionising the media) or directly by the parent particle.

The average amount of energy needed to create an electron-hole pair is called ionisation energy, W, and it is largely independent of the type of particle and/or energy and approximately proportional to the band gap energy, E_g [69] as shown in equation 2.43. One of the greatest advantages of semiconductor detectors is the low value of W, with values 2.96 eV (77 K) and 3.63 eV (300 K) for germanium and silicon, respectively, as seen in table 2.1.

$$W \approx 2.8E_g + 0.6\ eV \tag{2.43}$$

This means a tenfold value increase when compared to the traditional gas filled detectors used in dosimetry. A higher number of charge carriers means that the relative statistical fluctuations on the number of carriers per pulse becomes smaller. Also, the signal-to-noise ratio (SNR) is increased, allowing higher sensitivity when measuring low-energy radiation.

Since the gap value for silicon is 1.2 eV not all the energy imparted into the silicon detector is used in the electron-hole creation. Some of the energy will be used in other processes as lattice excitation or phonon production. In the case of silicon, around 30% of the energy imparted will create a readable signal, with the other 70% being wasted in other processes that do not generate a useful signal [70].

The variance in the number of charge carriers is very important due to its relation to the energy resolution of the detector. Both the average and variance of the number of charge carriers can be used to calculate the minimum signal threshold and the energy resolution. For any imparted energy by radiation this number N will fluctuate around a mean value $< N >$.

$$< N >= \frac{E}{W} \tag{2.44}$$

Being E the energy absorbed by the detector and W the mean energy required

to create an electron-hole pair. This number, $< N >$, would also be exactly the value of the variance of N if the system behaved following Poisson statistics, that is, if all events along the track were independent. The Fano factor is introduced as a relation between the observed experimental variance and the Poisson variance.

$$F = \frac{\sigma^2(N)}{< N >} \tag{2.45}$$

Low values of the Fano factor will indicate a good energy resolution. True values of the Fano factor for semiconductors as silicon and germanium are experimentally determined around 0.1 but experimental and theoretical values of the Fano factor still exhibit some disagreement [71, 72].

Modes of operation

Generally, a solid-state semiconductor detector will work by joining two different doped semiconductor materials (p and n-type). Charge carriers will diffuse across the boundary if the two regions are in good thermodynamic contact, working together as if they were part of the same crystal lattice. Electrons from the n-side will diffuse through the contact to the p-side, and vice versa.

This diffusion process will generate an electric field that counteracts the movement of the charges, creating a region with no free charges in the boundary called depletion zone. This depletion zone will act as the active area of a semiconductor sensor. A particle traversing the detector will generate electron-hole pairs along its track, with these particles moving out of the depletion region because of the electric field present. These charges will be collected by means of ohmic contacts in the semiconductor and will generate an electrical signal in the detection system in the form of a small current pulse in the order of picoamperes. Most pairs generated outside the depletion region will recombine quickly, not generating a measurable charge. Figure 2.16 shows a schematic of a typical PN-junction semiconductor detector.

If no external voltage is applied (i.e. the detector is unbiased), the electric field generated in the depletion zone is inadequate to generate an electric field

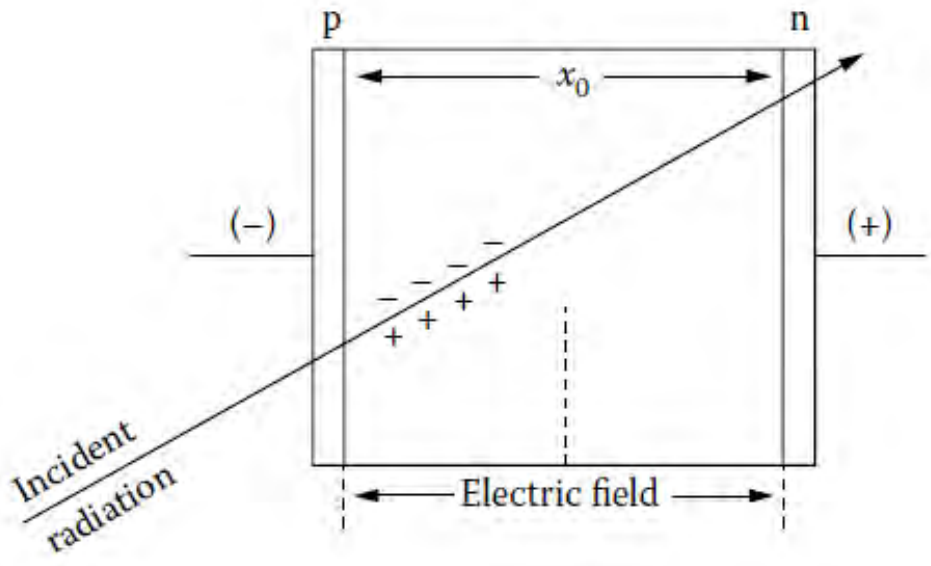

Figure 2.16: Schematic of a PN-junction semiconductor traversed by a particle generating electron-hole pairs. The diode can be reverse-biased to generate a larger depletion zone, with a thickness x_0 depending on the voltage.Taken from [67].

large enough to make the created electron-hole pairs move quickly to the collection zones and charges could be lost to trap and recombination processes in the semiconductor. The depletion zone in an unbiased detector is also very small and its capacitance will be high, so the capabilities of an unbiased detector will be very poor.

However, if an external voltage is applied by placing the n-side of the detector with a positive potential with respect to the p-side (this configuration is called reversed biasing) the depletion area of the detector will increase and the current flow through the semiconductor will be decreased. This is the usual configuration in semiconductor detectors.

If the bias voltage is large enough the depletion area of the semiconductor will fill the whole volume, resulting in a fully depleted detector. Higher voltages will

create an electrical breakdown, with a dramatic increase of the current flowing through the detector and the loss of accurate detection capabilities.

Solid-state based radiation detectors offer another way to obtain experimental data and offer several advantages over TEPCs, but lack some of the advantages a tissue equivalent detector can offer. Use of both kind of detectors yields the best results, as they complement between them. This dissertation will discuss the use of solid-state detectors, specially silicon micro-detectors.

2.6 Monte Carlo radiation transport

Monte Carlo methods are a branch of experimental mathematics that deal with experiments using random numbers [73]. These methods are computational algorithms that rely on random numbers to obtain numerical results and they have been found a use in a variety of fields.

In medical physics, Monte Carlo methods help with the problem of making calculations of dose deposition in media. Dose calculation is not a simple task since the analytical models used commonly for dose deposition in simple problems do not work when translated into complex geometries.

There is also a myriad of different outcomes for an incoming particle in the volume of study. If the particle is a photon, it could be annihilated, or could undergo soft or hard scattering, for example. Other kinds of particles (electrons, neutrons, protons, etc.) would yield different processes that could make the problem under study very difficult to solve[2], since the analytical solution of the propagation of a small number of particles would involve many very-large square matrices. Mathematically, this resembles a Markov chain [74].

If the probability for each specific type of event is known (i.e. we know all the cross sections for the energies at play for all the possible particles) the problem could be simulated by following many particles through the area of interest and their interactions sampled by following the cross sections for said particle. The

[2]In our case, this would mean that the Boltzmann Transport Equation should be solved analytically.

result of the simulation would be computed as the average quantity scored by repeating the process for many particles.

There are two big problems with this method: First, a good random number generator must be used to ensure the randomness of the sampling process. It is extremely difficult to generate true random numbers, as only a true random physical process (as radioactive decay, or cosmic ray spatial fluence) can generate true random numbers. This is not a problem for most applications, including radiation transport. A pseudo-random number generator could be used, sampling seemingly random numbers from a known probability distribution [75].

The second problem is that variance of the result is inversely proportional to the number of histories simulated and for very complex problems the computation time to reach an acceptable variance would be astronomically high. Furthermore, convergence to result is proportional to the square root of the number of histories. A compromise between desired uncertainty and computation time must be agreed upon.

Calculation efficiency, ε, can be described by the following relation between computational time T, and variance s.

$$\varepsilon = \frac{1}{s^2 T} \tag{2.46}$$

Maximisation of calculation efficiency is helped by using variance reduction techniques. Variance reduction must be used with caution since it can bias simulation results.

In medical physics there are a few codes to solve the particle transport problem. Some of them are multipurpose and can simulate the propagation of all kinds of particles, whereas there are some of them that can only handle a reduced number of them. Some Monte Carlo codes normally employed in the field of medical physics are the following:

- GEANT4: Monte Carlo code developed at CERN (EU) based in C++. GEANT4 is a toolkit with a complete range of functionality for tracking

the particles in user defined geometries with modular physics models [76]. The main inconvenient of this code is its complexity due to the number of options available, but this is also its strong point.

- MCNPX: General Monte Carlo N-Particle eXtended Transport Code. Developed by Los Alamos National Laboratory (USA) based in FORTRAN90 [77]. Capable of simulating particle interactions for up to 34 different particles and more than 2000 heavy ions at almost all energies. It is used mainly in the simulation of nuclear processes and in the nuclear industry.

- EGS: Electron Gamma Shower. Code designed originally for studying the electromagnetic showers produced in the detectors and accelerator of SLAC (USA), based in FORTRAN and no longer supported. An evolution of these code is EGSnrc developed at NRC/CNRC (Canada) and designed with medical physics applications in mind [78].

- PENELOPE: Code developed at University of Barcelona, also based in FORTRAN [79]. It is capable of simulating photon and electron/positron transport up to very low energies.

- SRIM: A package for simulation of ion transport in amorphous materials. The Monte Carlo portion of the program is called TRIM. Developed by James Ziegler [29]. TRIM can calculate the interactions of energetic ions with amorphous targets.

- FLUKA: Multi-purpose condensed history Monte Carlo code developed by CERN and INFN (Italy) based on FORTRAN77 [80]. Used for calculations of particle transport and interactions with matter and used in a very broad range of applications, including medical physics [81]. Capable of adding user routines to the code to further improve the output results.

2.6.1 FLUKA Monte Carlo code

The main Monte Carlo code chosen for this work was FLUKA. This was done because the FLUKA physics settings are fixed, although the thresholds for particle

transport and other options as step-sizes can be chosen by the user. FLUKA also has a very healthy community of users and their user support is generally positive. Even though FLUKA is based in FORTRAN77, a graphical user interface (GUI) called FLAIR can be used, making its use easier for a novice user. As GEANT4, FLUKA uses combinatorial geometry to build the simulation and includes a built-in scoring system.

FLUKA can simulate the transport of 60 different particles and heavy ions, can handle nucleus-nucleus interactions from the Coulomb barrier up to 10^4 TeV/u, electron and muon interactions from 1 keV to 10^4 TeV, photon interactions from 100 eV to 10^4 TeV, hadron-hadron interactions up to 10^4 TeV and neutron and neutrino interactions. It can also handle the tracking on magnetic fields and can handle analogue or biased calculations.

Furthermore, FLUKA has a pre-defined configuration set for hadrontherapy applications ('HADROTHErapy'). This pre-defined configuration changes the particle transport thresholds, activates multiple scattering and delta-ray options, makes corrections to form factor for inelastic Compton scattering and limits the maximum kinetic energy lost per step to achieve better accuracy in the results. The following settings are changed:

- Electromagnetic transport activated.
- Inelastic form factor corrections to Compton scattering and Compton profiles activated.
- Low-energy neutron transport down to thermal energies included.
- Fully analogue absorption for low-energy neutrons.
- Particle transport threshold set to 100 keV.
- Multiple scattering threshold set to minimum for both primary and secondary particles.
- Delta ray production activated with threshold of 100 keV.

- Ionisation fluctuations (straggling) activated for hadrons, muons and EM particles.
- Maximum energy loss per step 2% of the original energy.

A stricter additional limit to the maximum kinetic energy per simulation step was selected, changing it to the minimum energy allowed by FLUKA. This option was selected to reproduce the experimental results more accurately without adding too much additional computation time, as detailed in [82].

It should be noted that Monte Carlo simulations do not have any problems derived from measurement conditions or adequacy of the detectors. Also, the simulations follow the predictions of the model to the letter. With the proper code settings, the simulation can show the "true and real" behaviour of the radiation beam. Alas, Monte Carlo simulations cannot replace reality. The simulations are complementary to the experiment, as they rely in models to simulate reality, and quoting George E. P. Box, "All models are wrong, some of them are useful". Monte Carlo simulations have been broadly employed in this thesis, but they have been always compared to experimental verification.

USC
UNIVERSIDADE
DE SANTIAGO
DE COMPOSTELA

Chapter 3

Description of the silicon detectors and experimental device

Summary of the chapter:

This chapter describes the silicon microdosimeters used in this work, its fabrication process and read-out electronics. The limitations of the microdosimetric detector by means of charge collection efficiency processes is also discussed.

3.1 Introduction

In this chapter a novel type of silicon detectors for microdosimetry will be described. These devices are designed and manufactured by the IMB (Instituto de Microelectrónica de Barcelona, dependent of the Spanish National Research Council). The detector read-out and microdosimetric tests were performed by the Molecular Imaging and Medical Physics group of the University of Santiago de Compostela, group that the author of this dissertation belongs to.

In traditional planar detectors under conditions of high fluence the charges created induce a build-up of negative space charge in the depletion regions. To read all the generated signal is necessary to use very high bias voltages to overcome the trapping effect, generating a high leakage current that greatly reduces the signal to noise ratio. Also, typical drift paths of the charge carriers are in the same order of magnitude than the detector thickness, giving a relatively high charge collection time.

Parker and Kenney proposed the use of a 3D architecture to overcome these effects with aims to its use in medical imaging and high energy physics [83]. In the Parker and Kenney configuration the detector consists of a three-dimensional array of electrodes penetrating the silicon bulk and the charge carriers are collected by oppositely biased cylindrical electrodes. The drifting distance and collection times are greatly reduced since the charge carrier does not need to traverse the whole bulk to arrive to one of the collecting surfaces as in a planar detector. The biasing voltage needed to produce full depletion in the bulk is also reduced as the required depletion distance is equal to half the distance between two columns of opposite doping.

The U3DTHIN microdosimeter is the IMB version of this architecture. The first use of U3DTHIN detectors was plasma diagnostics and neutron detection [83–87], but due to their small thickness and defined active volume the detectors have been used in microdosimetric applications [88].

The second type of silicon detector described in this work is a 3D Cylindrical microdosimeter. This detector is an improvement of the U3DTHIN technology,

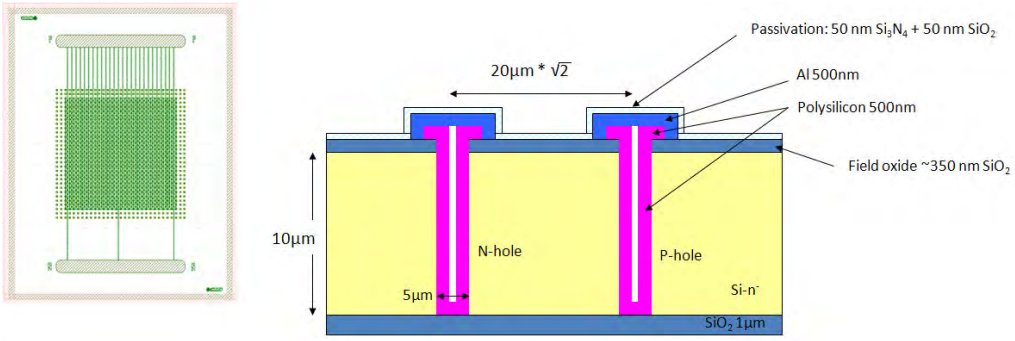

Figure 3.1: Left: Front-side view with columns of each type connected to a different collector. Right: Cross-section layout showing two different P and N columns drilled through the silicon bulk.

capable of individual cell readout and spatial detection. This iteration of the 3D technology was developed exclusively for microdosimetric applications and is based on the results found with U3DTHIN technology by IMB.

3.2 Description of the silicon detectors

3.2.1 U3DTHIN detectors

The first generation of 3D silicon detectors manufactured by the CNM (U3DTHIN) are PIN diodes fabricated on silicon-on-insulator wafers with an active thickness of 10 or 20 μm, with a 1 μm buried silicon oxide layer. The system rests over a 300 μm thick silicon support. Columns with a diameter of 5 μm are etched and filled with a p or n-type silicon, with each type connected to a different collecting electrode, therefore offering only one reading channel. The columns have a pitch of 80 μm between columns of the same doping type. The total area of the detector is 1042 $\times$ 1042 μm^2. Figure 3.1 shows a sketch of the detector.

The drilled electrode columns present in the detector do not add to the active area and were made as thin as possible, with a diameter of 5 μm. This type of detector adds the response of all the columns to a single channel, so a spatial

detection system in the micrometre range is not feasible with this detector.

As mentioned before, depletion volume on the detector is not dependent on the substrate thickness but on the length of the electrodes and the radius of the columnar electrodes since the depletion region will grow laterally in the bulk instead of vertically. This allows for much lower capacitances than planar silicon sensors for geometry sizes under 50 μm, meaning that the electronic noise will be much lower than on a planar detector set-up.

Fabrication process

U3DTHIN silicon sensors were manufactured in the clean room facilities of IMB-CNM on 4-inch SOI wafers from Icemos Technology Ltd. The n-type wafers were doped with phosphorous with nominal resistivity values $>$ 3.5 kΩ cm. Active thickness of the wafers was 10 and 20 μm. Buried oxide thickness was 1 μm and the support silicon thickness was of 300 μm. The main steps of the fabrication process will be discussed here. Figures from the fabrication process are taken from [89].

1. First, the wafers are labelled per IMB requirements. Then, the wafers are cleaned prior to the fabrication with a "piranha" etch composed of H_2SO_4 and H_2O_2, and a HF solution to eliminate any impurity from the surface. Finally, a silicon dioxide layer with a width of 400 nm is grown on both wafer sides by means of a wet oxidation process.

Figure 3.2: Wet oxidation process in the wafer creates a 400 nm width SiO_2 layer in both sides of the silicon wafer.

2. A photolithography process is done to define the position of the n-columnar electrodes. The photoresist is placed on the surface of the wafer and the first mask is placed. Then, UV-light is used to expose the resist is removed with a developer solution and the SiO_2 is eliminated with a buffed HF solution.

Figure 3.3: Photolithography process to define the poisition of columnar electrodes and SiO_2 etching.

3. Using a deep reactive ion etching (DRIE) process the electrode column is etched. DRIE is an anisotropic process that combines plasma etching using SF_6 with cycles of passivation using octafluorocyclobutane (C_4F_8). This allows to get vertical trenches with high aspect-ratio. After the DRIE process, the photoresist is removed.

Figure 3.4: DRIE process to create the columns and photoresist removal.

4. The etched N-columns are partially filled with a 500 nm polysilicon deposition process. The polysilicon layer is then doped with phosphorous coming from a $POCl_3$ gas source to form ohmic contacts on the sensor. A phospho-

silicate glass (PSG) layer is formed when the P atoms from the gas get in contact with the polysilicon that acts as a donor source. After the process the wafer is cleaned again.

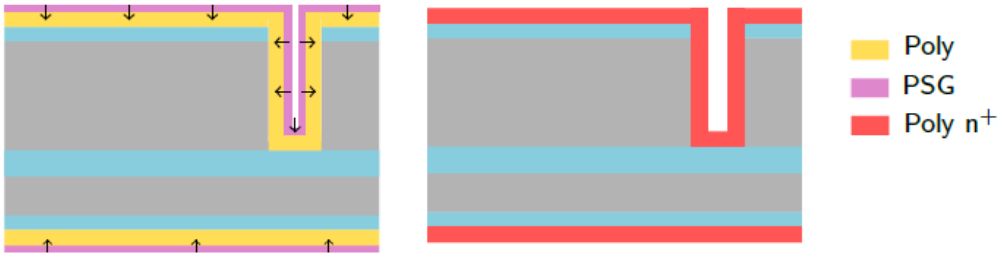

Figure 3.5: Filling of the N columns with doped polysilicon and creation of ohmnic contacts.

5. A second photolithography process is done to define the n-electrodes on the surface of the wafer, removing the exposed photoresist and polysilicon layer. Next, the photoresist is cleaned and a layer of 100 nm of SiO_2 is grown to protect the n+ electrodes.

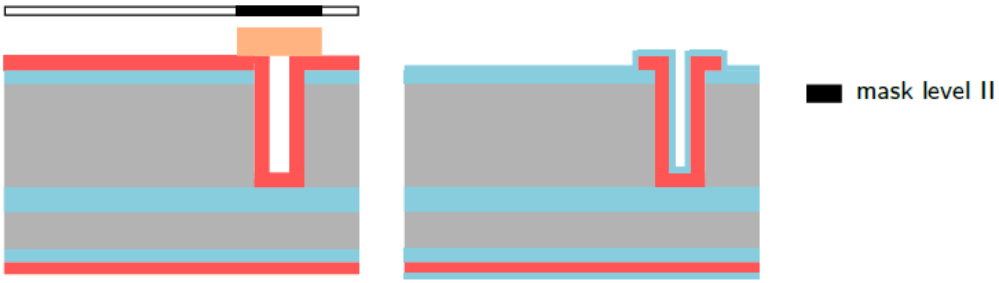

Figure 3.6: Photolithography process for the n+ contacts and oxide growth.

6. Steps 2-5 are repeated to create the p-type columnar electrodes. P-type impurities are added from a solid BN source. A borosilicate glass layer is grown on the wafer instead that acts as a source of acceptor impurities.

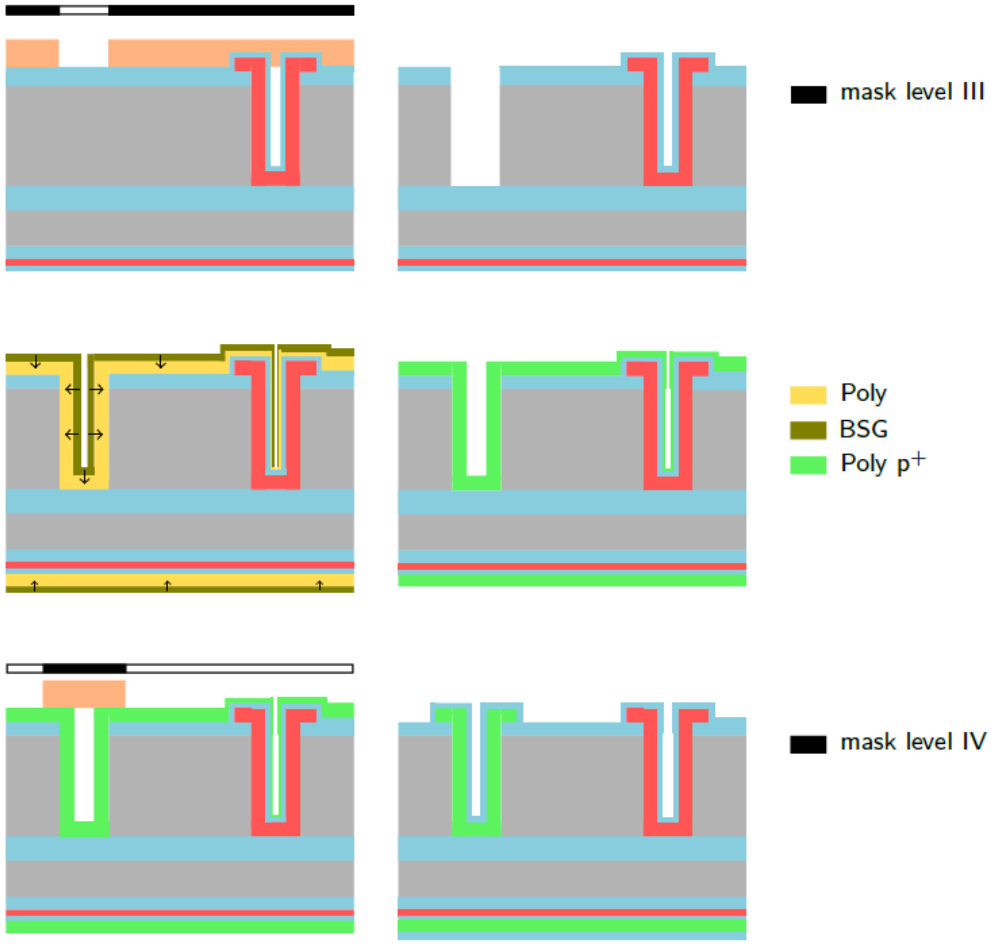

Figure 3.7: Fabrication process of the p-columnar electrodes, similar to the process of figure 3.14.

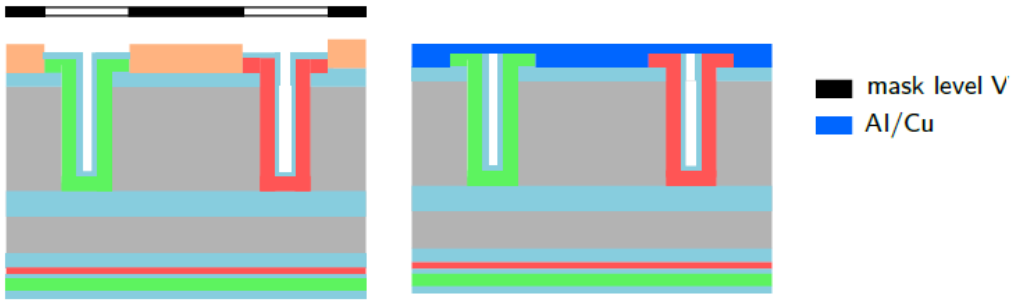

Figure 3.8: Photolithography process to etch the SiO_2 on top of the columnar electrodes and metal deposition.

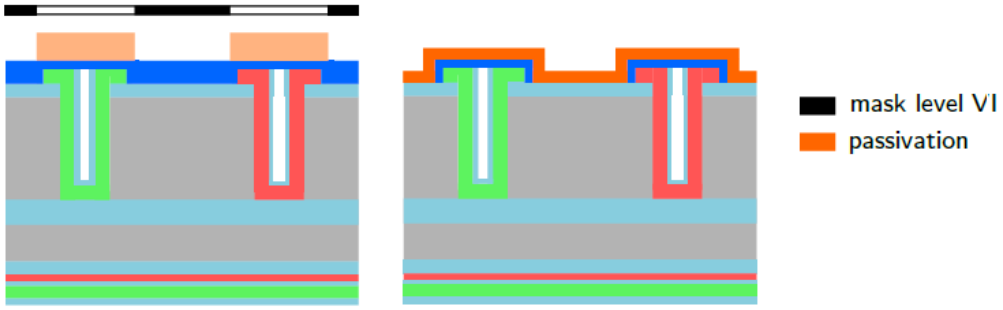

Figure 3.9: Photolithography process and passivation layer deposition.

7. A fifth photolithography process is done to etch the SiO_2 layer on top of the electrodes to provide a direct contact between the doped polysilicon and the 0.5 μm Al/Cu electrodes deposited next.

8. The metal lines connecting the p+ and n+ electrodes are placed through a new process of photolithography. Then, a passivation layer consisting of SiO_2 and Si_3N_4 is deposited by plasma enhanced chemical vapour deposition (PECVD) to protect the detectors from external agents. Contacts for the signal output were opened through the passivation layer with a final photolithography process.

3.2.2 3D Cylindrical Microdosimeters

The 3D cylindrical microdosimeter system consists of an array of independent reading cylindrical unit-cells with a volume like mammalian cellular structures [90]. The unit cell of the detector is a cylindrical structure with an implanted p+ junction electrode that collects the charge surrounded by a concentric three-dimensional n+ electrode trench. The axis of the unit cell is perpendicular to the silicon wafer plane. There are 11 x 11 unit-cells in the detector forming a square array. The diameter and separation between p-electrodes (pitch) can take different values depending on the model. There are available diameters of 9, 10, 15, 20 and 25 μm and pitches of 25, 50, 100 and 200 μm. A detailed device schematic and cross section can be seen in figure 3.10.

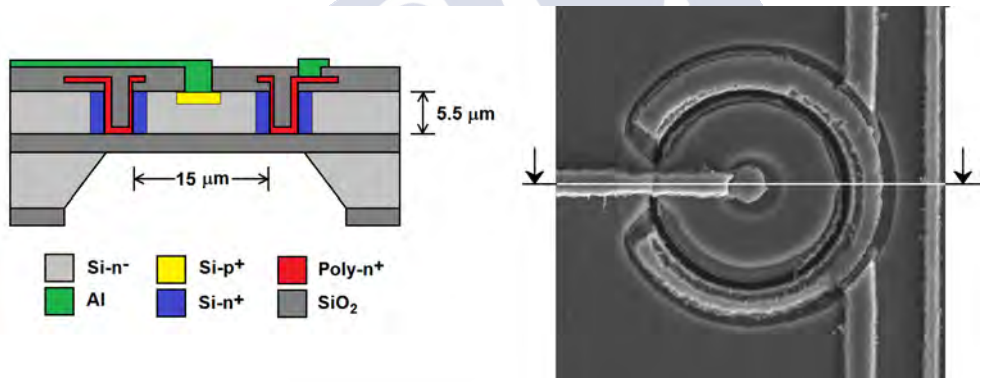

Figure 3.10: Electron microscope photograph and schematic cross section layout of the silicon sensor cell (not to scale).

The diameter of the central electrode is 4 μm and the width of the n+ trench is 3 μm. Each p+ unit-cell is connected individually to a contact pad through metal lines, allowing independent operation and providing spatial resolution. The n-electrodes of all the unit-cells are connected to the same pad on the opposite side of the detector. The thickness of the microdosimeter is of (5.50$\pm$0.5) μm and the substrate beneath was eliminated to avoid possible particle backscattering.

Fabrication process

The 3D cylindrical microsensors were fabricated with SOI wafers from Icemos Technology Ltd, as the U3DTHIN silicon detectors. The active thickness of the wafers were 6, 10 and 20 μm. The silicon was <100> n-type doped with phosphorous with nominal resistivity > 3 kΩ cm. The buried oxide had a thickness of 1 μm and the support silicon thickness was 300 μm in all the wafers. The main steps of the fabrication process will be briefly described here (there are several cleaning processes between these steps, not detailed in this enumeration), and as in the previous section, all diagrams are taken from [89]:

1. Wafer cleaning and growth of 0.4 μm SiO_2 on both sides of the wafer. The SiO_2 is then etched by means of a photolithographic process in the sites where the electrodes will be placed.

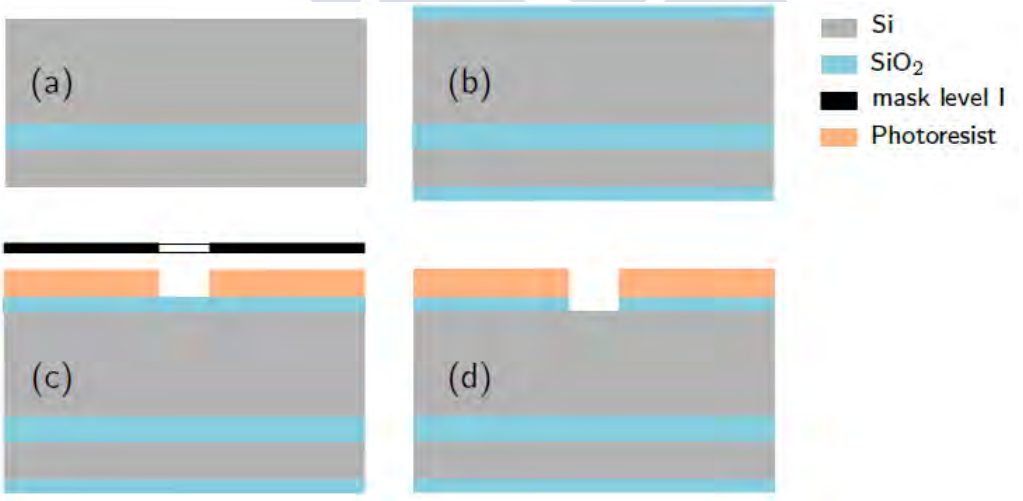

Figure 3.11: (a) SOI wafer ready for fabrication. (b) Wet oxidation process in which the wafer is covered by a layer of SiO_2. (c) Photolitography process. (d) SiO_2 etching.

2. Boron implantation using an ion beam is performed to create the 4 μm diameter p+ electrodes. To prevent channeling of boron ions in the silicon

bulk a 365 Å SiO_2 layer was grown beforehand. After the implantation, a 0.4μm SiO_2 layer was grown to protect the p+ from possible damage in the following steps. A photolithography process to define the n+ trench was done afterwards.

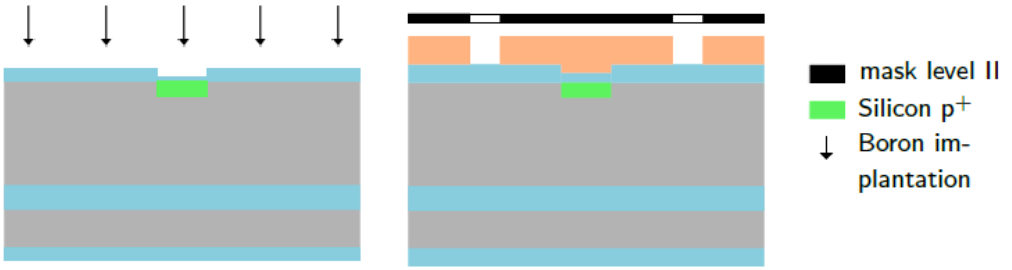

Figure 3.12: Boron implantation in the p+ electrode area and photolitography to define the trenches of the cylindrical annulus surrounding the active area.

3. Etching of exposed SiO_2 and DRIE in the silicon to create the n+ trenches is done. Depending on the final detector thickness, the DRIE process will etch a variable depth of silicon.

Figure 3.13: SiO_2 etching and DRIE process to create the trenches of the cylindrical annulus.

4. The etched cylindrical trench is partially filled with polysilicon and then doped with phosphorous atoms from a $POCl_3$ gas source, creating a PSG

layer acting as a source of donor impurities for the polysilicon. Then, the PSG is etched away from both sides of the wafer.

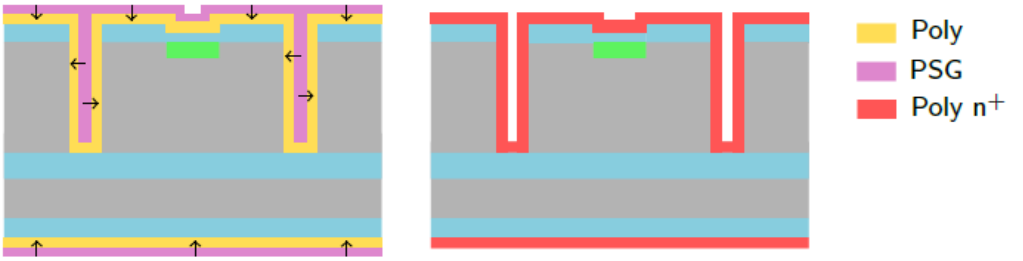

Figure 3.14: Polysilicon deposition in the trenches and doping with $POCl_3$.

5. A photolithography process is done to keep the n-doped polysilicon over the cylindrical trench and washed away from the rest of the wafer.

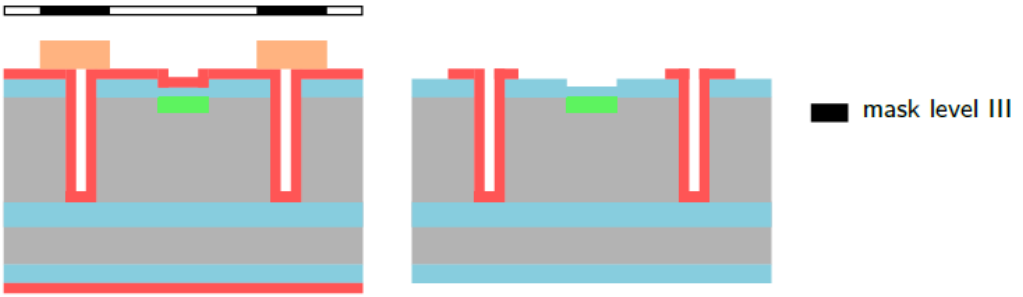

Figure 3.15: Photolithography process to clean the wafer of unwanted n^+ regions outside the trenches.

6. A Tetraethyl orthosilicate (TEOS) oxide layer is deposited filling the trenches and insulating the n-doped polysilicon. As the metal strip that will connect with the p-doped material will cross over the trench is very important to avoid any kind of shorting between the electrodes. A photolithography process is then done to open a contact between the doped regions (both p and n) and the metal that will be deposited in later steps.

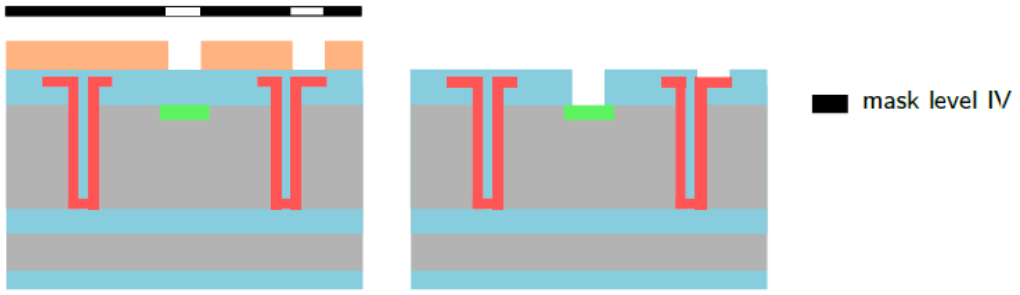

Figure 3.16: SiO_2 growing process followed by a photolithography process to prepare the electrical contacts that will be placed next.

7. A 0.7 μm Al/Cu metal layer is deposited to create the electrical contact for each one of the unit cells over the whole wafer and then a photolithography process was done to remove the material from the undesired regions. A passivation layer was then deposited to protect the active volumes from external exposure.

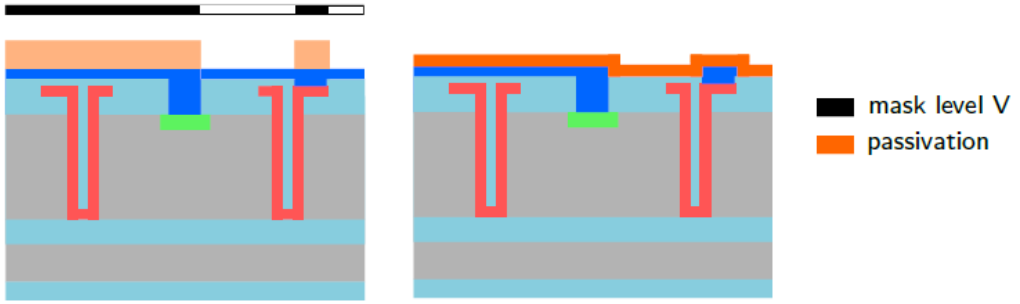

Figure 3.17: Metal deposition (dark blue) followed by a deposition of the passivation layer.

8. Passivation over contact pads is removed trough a photolithography process for signal output. The backside of the microcylinder can be etched in this step to remove the support silicon and avoid contribution by backscattered particles.

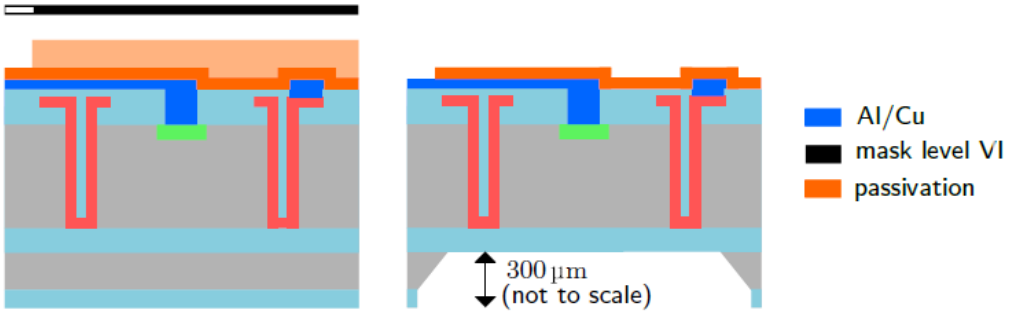

Figure 3.18: Final photolithography process to remove the passivation over the contact pads for signal output and etching of the support wafer in the backside of the detector.

The fabricated microcylinders will have a reduced active volume compared with its design values due to the low charge collection efficiency of the n+ doped volume that cannot be considered as a completely active volume. Also, a percentage of the active silicon is consumed due to the etching and oxidation processes with a loss of at least the 40% of the active silicon volume.

3.3 Detector readout

The process by which an ionising particle creates a signal in a semiconductor was described in section 2.5.2, but generally this signal is too small to be read as it leaves the detector. An amplification process is needed to correctly quantify the energy deposition in the detector.

This is done by adding several different stages to the detector system that adapt and shape the inbound signal in order to be read by a multi-channel analyser and provide a spectrum. Figure 3.20 shows the different stages of a detector system. These stages can be classified as pre-amplification, shaping or amplification stages.

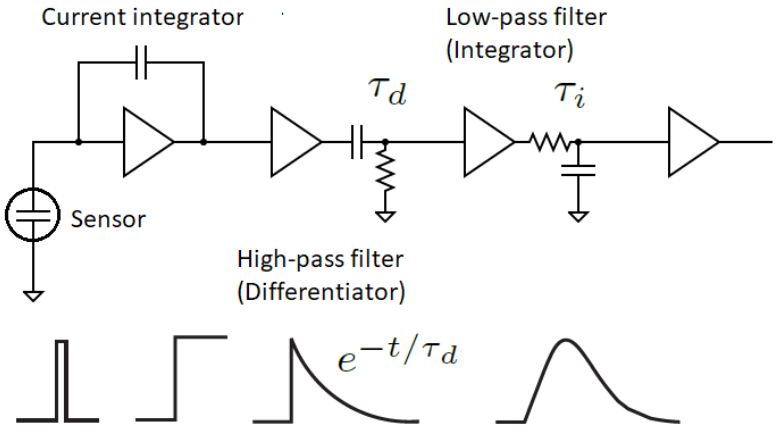

Figure 3.19: Sketch of the different readout stages in an ionising radiation detector system. In the lower part of the figure the signal output of each stage can be seen.

Once the sensor has converted the physical process into an electric signal it goes into the amplifier stage. The charge sensitive preamplifier works as a current integrator and converts the small current pulse into a large voltage pulse while keeping the noise levels at a minimum. On the next stage the signal goes through a high-pass CR filter that acts as a differentiator and then a RC low-pass filter acting as an integrator. With these two stages the decay, rise time, and bandwidth are set. The signal to noise ratio is also improved by eliminating the low and high frequency components of the signal with no useful information. During these processes the signal is shaped into a form that can be read by a multi-channel analyser, but also is attenuated, and an amplification stage is added afterwards to increase the amplitude of the output pulse. It is important that shaped signal recovers baseline level in a fast way in order to avoid signal pile-up. In this type of shaped signal, the pulse height is proportional to the energy imparted to the sensitive volume [91].

3.3.1 U3DTHIN detector

The U3DTHIN detectors were connected to a front-end AC coupled charge sensitive preamplifier with a typical response of 5V/MeV in silicon followed by a pulse shaping stage with a time constant of 2.5 μs. The analogue signal was connected to a multichannel analyser (AmptekMCA-8000A) at the experimental area control room controlled through a serial link from the DAQ computer. This readout system was developed by the IMB-CSIC using the Analog Devices ADA4817 ultrahigh speed voltage feedback amplifiers with FET input, and the sketch of the readout system is taken from [89]. This was the system employed for the GANIL experiments described in detail in the next chapter.

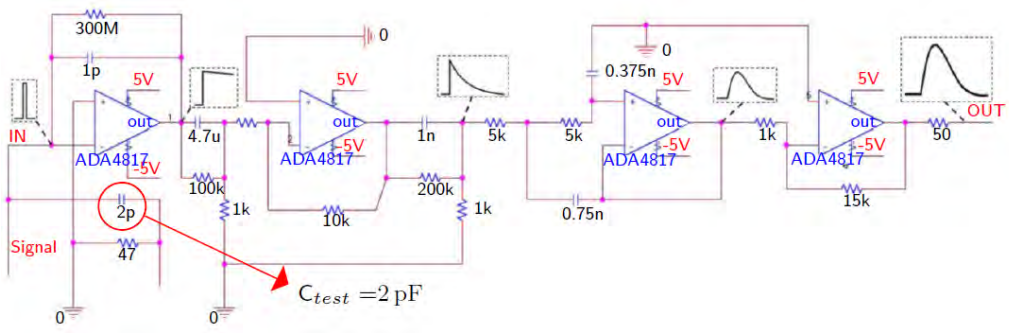

Figure 3.20: Sketch of the readout system for the U3DTHIN detectors. The circuit includes a test input to calibrate the system by injecting charge through a 2 pF capacitance that imitates the signal of an incident particle impinging on a solid state detector. Taken from [89]

.

3.3.2 3D Cylindrical microdosimeters

The first version of the 3D Cylindrical microdosimeters readout system consisted of a CAEN A1422H Hybrid charge sensitive preamplifier together with a NIM CAEN N968 spectroscopy shaping amplifie. The charge sensitive preamplifier had 400 mV/MeV sensitivity, thus allowing signal pulse height in excess of 10 V/MeV when combined with the NIM spectroscopy amplifier. Pulse height was digitized

through an Amptek MCA8000D multichannel analyser in the experimental room, connected via Ethernet to a computer where the spectra were stored. This system was used for the CNAO experiments described in detail in the next chapter, but it was too cumbersome to be easily carried throughout all the different experiments performed, so a new solution was designed by our group consisting of a more portable readout system.

Figure 3.21: Picture of the newest version of the 3D Cylindrical microdosimeter detector along the readout electronic system. The system is portable due to its reduced dimensions (170 x 35 mm)

The new electronics version consisted of two different printed circuit boards: the first one housed the detector and charge preamplifier far away from the rest of the components (10 cm) to avoid irradiation of the electronic system, and the second board includes shaping and amplification stages, allowing to get a high

signal to noise ratio with total dimensions of 170 x 35 mm. Figure 3.21 shows a picture of this portable detection system. The preamplifier employed was an OPA657, a device with a high-gain bandwidth, low-distortion, voltage-feedback operational amplifier with a low-voltage noise JFET-input stage offering a very high dynamic range amplifier suitable for the very low level signals that the detector provides [92]. Figure 3.22 shows the implementation of this circuit.

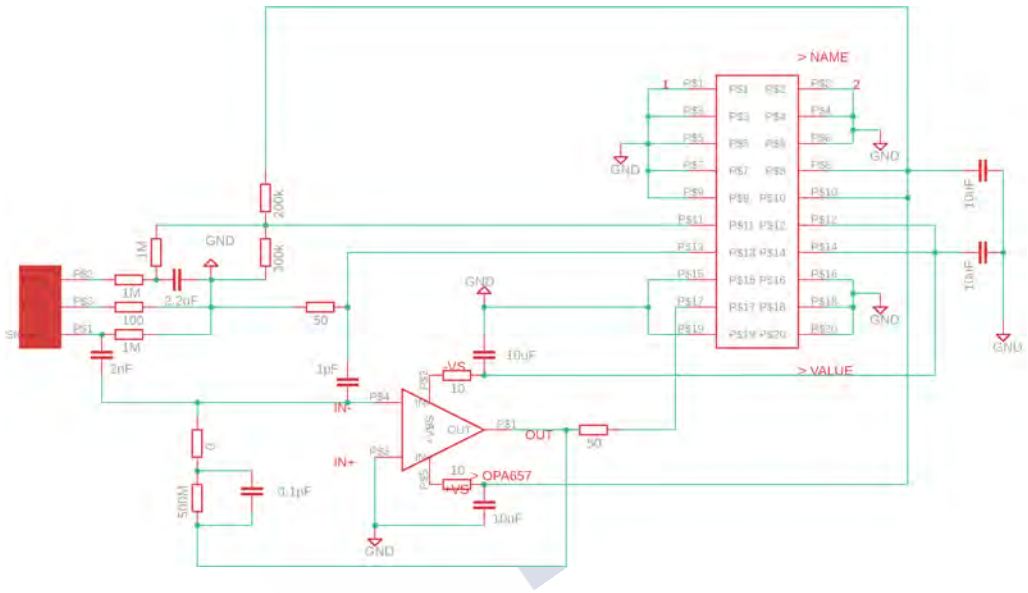

Figure 3.22: First stage of the new readout system containing the detector and a low-noise preamplifier. This board is connected to the shaping board through a 20 pin SAMTEC micro pitch connector (1.27 mm pitch)

The second part of the readout system has a more traditional setup, housing an inverter fixed gain amplifier (HFA1112). After the inverter, a CREMAT CR-200 Gaussian shaping amplifier and a CREMAT CR-210 baseline restorer followed by a HA-5002 current buffer amplifier to drive the output signal. Figure 3.23 shows the schematic of the shaper board of the readout system. The output from the system is connected to a multi-channel analyser (MCA).

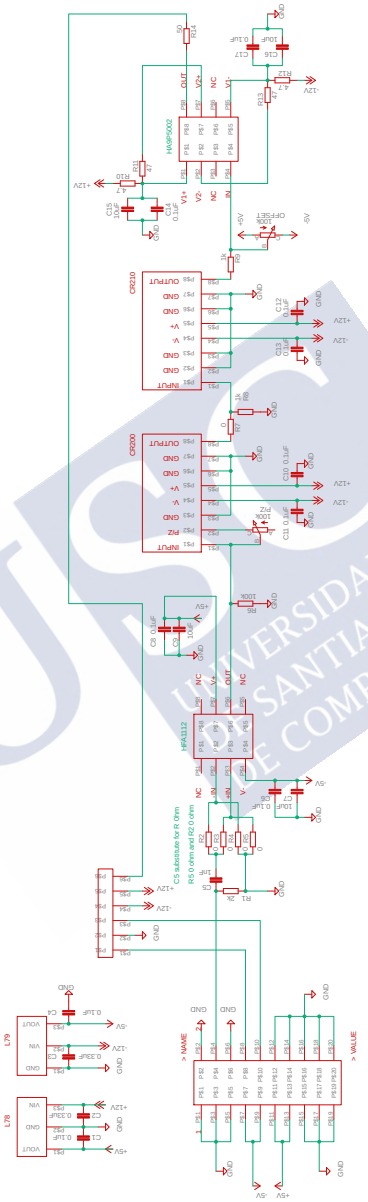

Figure 3.23: Second stage of the readout system containing the shaping amplifier and baseline restorer stages. The signal output goes to a multi-channel analyser.

3.3.3 Calibration

The principle of use of these devices assumes the proportionality between the electronics output voltage pulse height and the energy deposited in silicon. To establish a full system calibration, two kind of measurements were performed. First, a calibration through a voltage pulse applied to a test capacitor (1 pF) that allowed to measure the relationship between the silicon-equivalent energy of the charge injected at the input of the preamplifier and the MCA corresponding channel. Second, the measurement of the signal spectra recorded by the interaction of alpha particles either from ^{241}Am or ^{238}Pu decay was used to verify the performance of the full detector system. This calibration process is necessary to convert afterwards the pulse height spectrum into a microdosimetric one.

The charge injection through the test capacitor can simulate the radiation-matter interaction inside a detecting volume, with the charge collected by the readout system being proportional to the amplitude of the injected signal according to the following equation:

$$E = \Delta V \, C \, \frac{W}{e} \tag{3.1}$$

Where ΔV is the amplitude of the square pulse in volts, C the capacitance, W the energy required to produce an electron-hole pair in the material (in silicon, W=3.6 eV) and e the charge of the electron. The associated uncertainty depends on the accuracy of the capacitance value and the resolution of the multi-channel analyser. A negligible uncertainty on the position of the channel was asumed in these calculations. Figure 3.24 shows an example of a callibration curve obtained through this method using a 3D Cylindrical microdosimeter connected to a CAEN A1422H Hybrid charge sensitive preamplifier followed by a CAEN N968 spectroscopy shaping amplifier. The output was read using an Amptek MCA8000D multichannel analyzer.

In the second method, two different α-sources of ^{241}Am and Pu^{238} were placed over the detector to be tested and the energy deposition spectrum was recorded. Then, a Monte Carlo simulation of the same source and the same geometry as

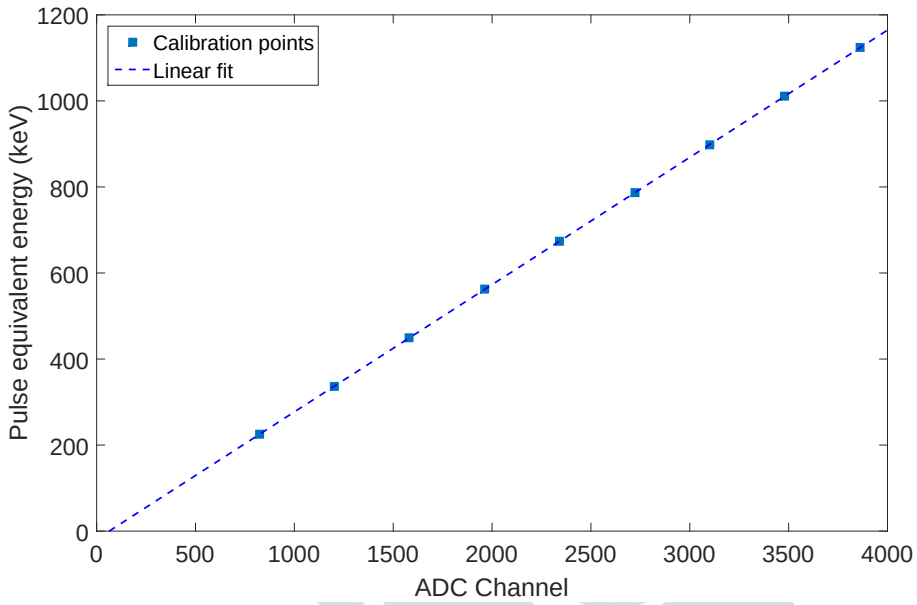

Figure 3.24: Calibration curve obtained with the injection of a test square pulse into the readout system consisting of a CAEN A1422H Hybrid charge sensitive preamplifier followed by a CAEN N968 spectroscopy shaping amplifier. The output was read with an Amptek MCA8000D MCA.

the laboratory experiment was executed, and the value for the most probable imparted energy was matched with the most probable ADC channel. Assuming the origin ordinate was null, a calibration using those two points (y = a x) to assign values of imparted energy to the MCA channels was done. This allowed to check whether the dynamic range of the detector was suitable to the experiment at hand or not. Figure 3.25 shows the calibration spectra recorded for an ^{241}Am source with a 3D Cylindrical microdosimeter and the same readout electronics employed for the first calibration method shown in figure 3.24 (blue crosses) along with a FLUKA Monte Carlo simulation of the energy deposition spectra (red line).

These two direct calibration methods gave different and incompatible results between them. For example, in the case of the 3D Cylindrical microdosimeters,

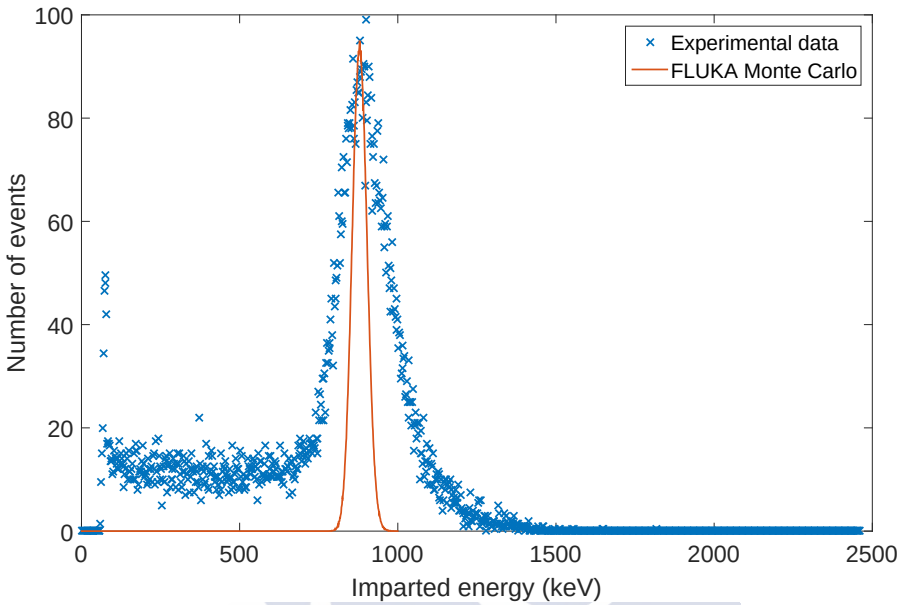

Figure 3.25: Experimental (blue crosses) ^{241}Am spectra taken with a 3D Cylindrical microdosimeter for calibration purposes along with the FLUKA Monte Carlo simulation results (red line).

the energy deposited by a 5.486 MeV α-particle (the most probable energy for the ^{241}Am α-decay) in 5.5 μm of silicon deposits around 880 keV according to FLUKA Monte Carlo with a detailed simulation of the setup. Supposing the MCA uses a full scale width of 4096 channels, according to the first method the channel for the most probable energy should be around channel number 3200, whereas the second method places this deposited energy around channel number 1500.

This discrepancy can be partially explained by the 25% tolerance of the test capacitor value and also the charge collection efficiency across the detector that provokes a reduced collected charge with respect to the Monte Carlo simulations that from our data (see next section) cannot account for more than 10%. Although this difference can be produced by partial depletion of the active volume, the results of IBIC tests indicate that this effect would only change the pulse

height at most a 8% between 0 V and 3 V bias voltage (see figure 8 in [93]). The rest of the discrepancy remains unaccounted for as of the writing of this dissertation. There are several hypothesis being worked on that will be discussed in the following paragraph.

In some production batches there was little control over some of the most external layers of the detector, and a difference on the thickness of some of those layers could greatly affect the Monte Carlo results due to the high ionisation density of the α-particles employed. Another possible source of uncertainty stemming from this last property of the α-particles is that if any particle enters into the detecting volume with an angle different from normal incidence the energy deposition will be larger, shifting the peak position to the right and smearing the energy deposition spectra.

Due to the incompatibility of these results a different, an indirect calibration method was employed for this detection system and will be described in the following chapter.

A new batch of the detectors was received by the end of 2018. These detectors had an increased thickness (nominal values of 10 μm and 20 μm) while keeping the same structure as the 3D Cylindrical Microdosimeters described in this work. The repetition of the electronics calibration and measurements with ^{238}Pu yielded a better agreement between experimental data and simulations. In this case, the expected signal was calculated using SRIM Monte Carlo and was compared with a pulse height spectrum calibrated from the test input of the read-out system. Due to the performance of the system, the data (shown in figure 3.26), exhibits low statistics corresponding to more than 20 hours of data acquisition.

3.4 Charge collection efficiency

During the study of the microdosimetric properties of the 3D Cylindrical microdosimeters some limitations to their operational capabilities were detected. A loss of collected charge produced from the track ionization due to recombination processes that affect the reconstruction of the imparted energy distributions was

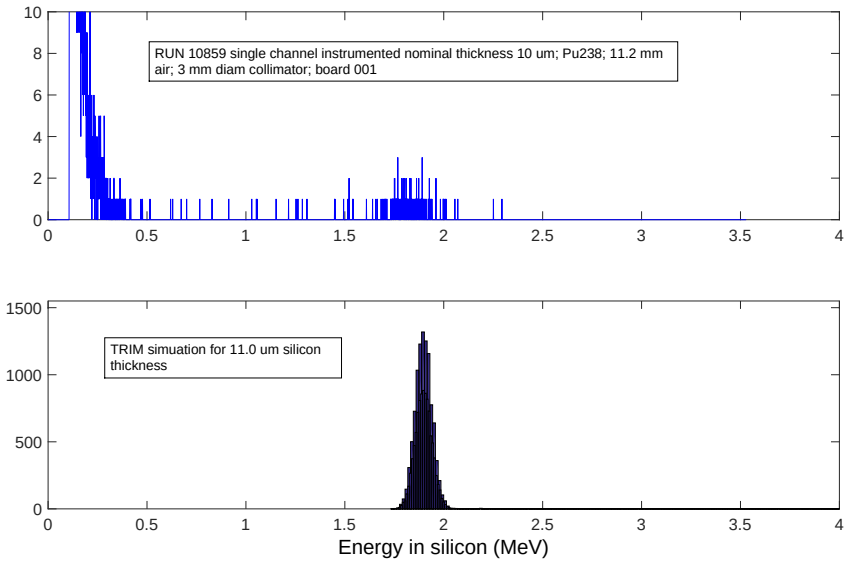

Figure 3.26: Up: Single channel spectrum from run 18059 with nominal thickness of 10 μm and diameter of 15 μm from ^{238}Pu corresponding to α-particles of 5.499 MeV (70.91%) and 5.456 MeV (28.98%) using electronics calibration (most probable deposited energy 1.8 MeV). Down: SRIM simulated energy deposition for 11 μm that gives a most probable deposited energy of 1.89 MeV.

found, provoking a modification of the microdosimetric spectra.

This effect is summarized usually through the charge collection efficiency dependence on the track impact position. The intrinsic field gradients present in the device together with the charge drift and diffusion provoke that in the microdosimeter cell periphery the charge collection efficiency exhibits a relatively fast decay to null values. Partially depleted silicon volumes present in the device lead to recombination of the ionization charge and partial charge collection. Due to the intrinsic technological limits in the microelectronics manufacturing processes, this charge collection transition is not negligible in general terms and can affect the reconstructed microdosimetric spectrum from the silicon micro-cell. This issue has been addressed in the present study to evaluate its significance and the limitation consequences for the actual microdosimeter geometries.

Furthermore, in the current state of the art, solid state microdosimeters lack of intrinsic amplification and this limits seriously the signal to noise for devices in the micrometer and sub-micrometer dimensions. The active volume and charge collection properties of IMB-CNM 3D Cylindrical microdosimeters were studied.

In the case of the microdetectors studied the output signal was taken as proportional to the imparted energy in the sensitive volume. From the spectra given by the detector signal, other microdosimetric quantities can be calculated. To evaluate the charge collection properties of the device, a model for the charge collection efficiency as a function of the distance to the centre of the active area was developed and then compared its results with experimental data from test runs done at the Fondazione CNAO (Pavia, Italy) synchrotron using a ^{12}C ion beam and also in a proton microbeam in CNA (Seville).

3.4.1 Materials and methods

Experimental set-up

The characterization of these devices with ion therapy beams were performed using an 115.23 MeV A^{-1} ^{12}C ion beam at Fondazione CNAO (Pavia, Italy) [94]. Several measurements were carried out placing the microdosimeter in front of a variable depth of polymethyl methacrylate (PMMA, density 1.186 g cm^{-3}). The depth was controlled using a motorized remote wedge system. The wedge system is formed by two 10° PMMA wedges allowing a variable depth of 3 mm to 40 mm with an uncertainty of the depth of around 30 μm. PMMA is a tissue-equivalent material, allowing to perform measurements in the fields of microdosimetry and radiobiology, the main scope of these detectors. The set of microdosimetric spectra obtained cover from the beam entrance plateau up to the Bragg peak. A more detailed study of these measurements is presented in section 4.2.1.

The microdosimeter was connected to a CAEN A1422H Hybrid charge sensitive preamplifier and to a CAEN N968 spectroscopy shaping amplifier. Then, the resulting pulse height was digitized through an Amptek MCA8000D multichannel analyser placed in the experimental room, connected via Ethernet to a computer

in the control room where the spectra were stored.

For the detailed evaluation of the Charge Collection Efficiency (CCE) we used the IBIC proton microbeam facility at CNA (Seville). During the irradiation the beam was scanned through the detector with a beam FWHM varying from 3.46 μm (X) up to 4.85 μm (Y) and the readout was performed through a synchronized amplifier and digitizer chain. The kinetic energy of the proton beam employed was 600 keV in different test runs conducted in vacuum. Figure 3.27 shows the pulse height spectra for 0 V and 3 V bias voltage in the IBIC proton beam.

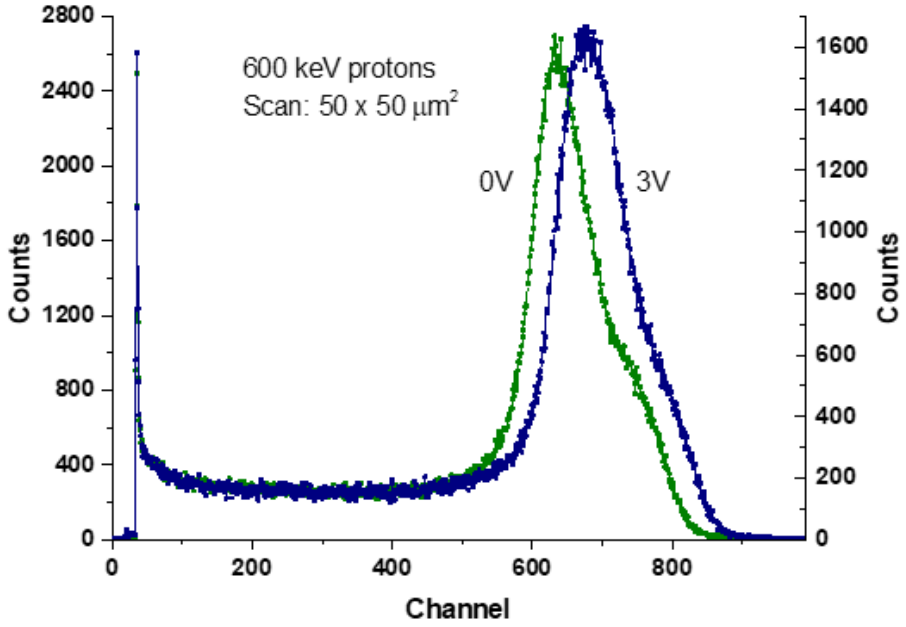

Figure 3.27: Pulse height spectrum for 600 keV proton beam in vacuum taken at the IBIC beam at CNA (Seville, Spain).

Electrical simulations

Electrical simulations were conducted with a Technological Computed Assist Design (TCAD) software, Sentaurus Synopsys. This software solves the Poisson equation for the studied geometry. Those simulations show in good detail the electrical field of the microdosimeter as also the transient of a heavy ion through any angle of the device, giving the charge collection. The simulated device is a 10 μm radius n-type (with a doping concentration of 8.61×10^{11} cm^{-3}) microdosimeter with a 5.3 μm thickness. The silicon dioxide charge surface density used is 1x10^{11} cm^{-2}.The electrical simulations were carried out with 0 V, 5 V and 10 V bias voltage. From capacitance measurement and simulation the microdosimeter is expected to be fully depleted at 5 V voltage bias. The transient simulations use the HevyIon software function, with particles that have a LET$_f$ in silicon (Linear Energy Transfer function) of 1.282x10^{-5} pC/μm impinging perpendicularly to the surface of the microdosimeter.

Monte Carlo simulations

The experimental work was benchmarked against a Monte Carlo simulation of the beam energy deposition in an individual cell of the detector. Monte Carlo simulations were performed using the FLUKA Monte Carlo code [80, 81], developed by CERN and INFN. The code is described in detail in section 2.6.1.

For each geometry a simulation with 10^5 histories in total was computed. The estimated relative statistical uncertainty for the simulation in the plateau region of the Bragg curve was of less than 2%. The code was commissioned against a water depth dose distribution of the same CNAO experimental beam measured with a Peakfinder variable water column and a PTW 34080 Bragg-peak chamber. This procedure is detailed in section 4.1.2.

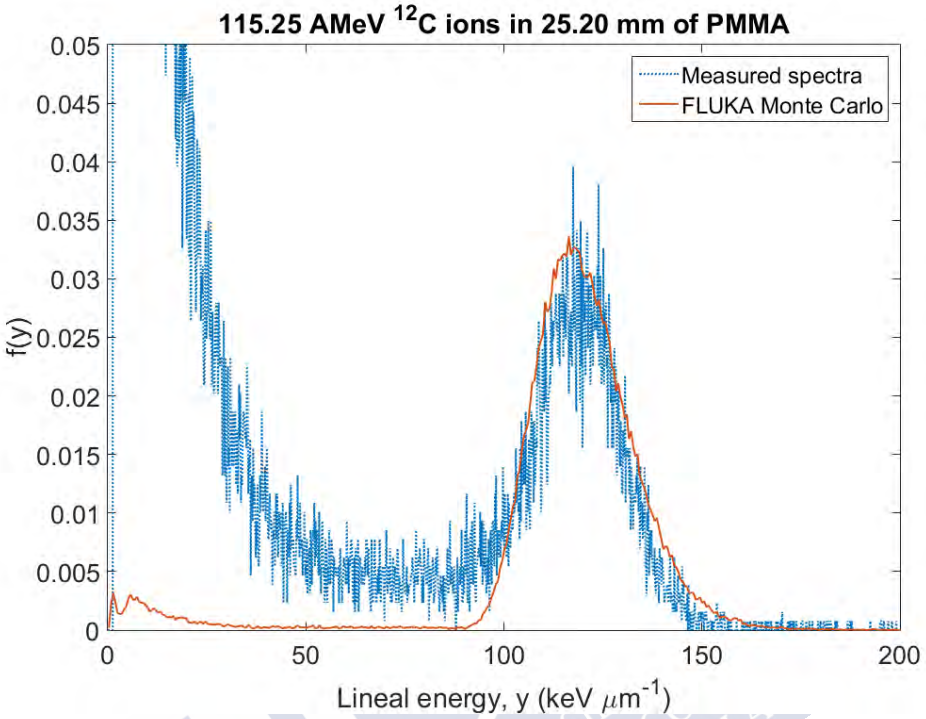

Figure 3.28: Original measured experimental spectrum (blue dotted line) and FLUKA Monte Carlo simulation (red solid line) for 115.25 MeV A^{-1} ^{12}C ions traversing 25.20 mm of PMMA.

3.4.2 Results

Charge Collection Efficiency

Clinical ^{12}C beam experimental spectra obtained with the new cylindrical microdosimeters exhibit a reasonable agreement with the expected results of the Monte Carlo simulations [94]. Nevertheless, experimental pulse height distributions always show a relevant tail with high number of counts in the low-energy part of the spectra and a small shift in the peak position when compared with the imparted energy distributions from simulation, as can be seen in figure 3.28. Electronic noise contribution, amplifier baseline shifts or pile-up events have not been found to be able to generate this distortion of the measured data from the

microdosimeters.

The effect of spectrometry distortion in silicon microsensors has been reported previously in different devices with high granularity readout [95, 96]. The main hypothesis is that this behaviour is produced by intrinsic field gradients and charge diffusion that modify the recorded spectra by the microsensor, provoking partially depleted volumes leading to recombination and partial charge collection in the periphery of the microcylinder. As a consequence of this, the measured microdosimetric spectra is modified, taking the form seen in the aforementioned figure when it is compared with a Monte Carlo simulation with the detailed geometry of the detector.

To study these effects a detailed electrical simulation of one cell of the microsensor was performed using Sentaurus TCAD. The figure 3.29 shows the electric

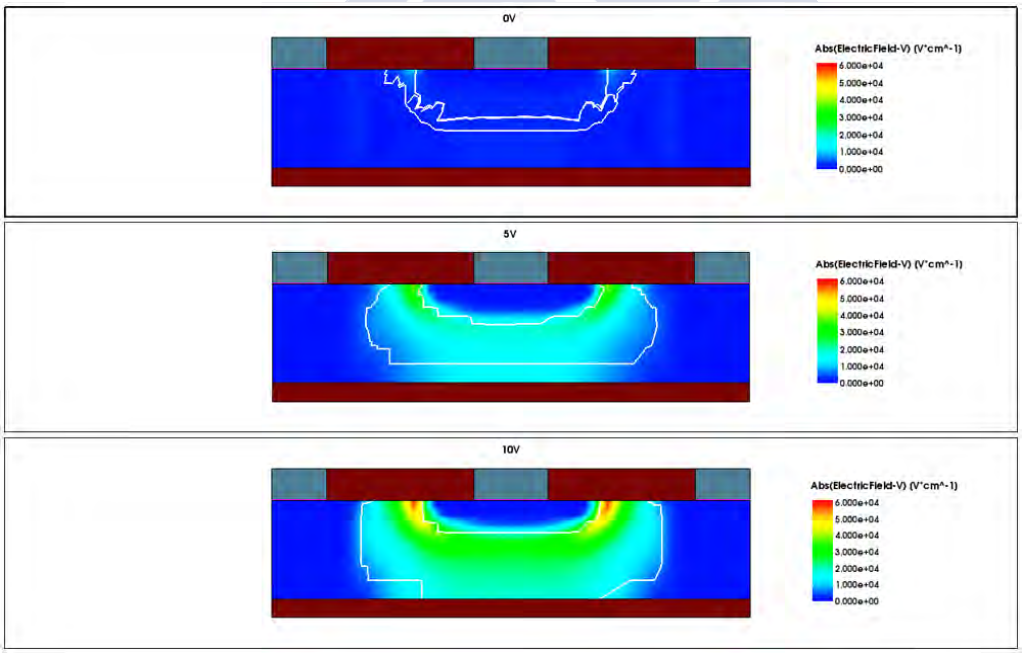

Figure 3.29: Electric field simulation using Sentaurus TCAD inside a microcylinder for biasing potential of 0 V (top), 5 V (center) and 10 V (bottom). The white line denotes the depletion volume inside the semiconductor

field simulations inside a unit cell of the detector for different biasing potentials. The sensor lenticular shape depletion volume is shown in this figure delimited by the white solid lines. The simulations additionally reproduce the transient electric signal associated to the particle ionization event. For that scope, taking into account the 3D depletion volume that depends on the electric field inside the device, the drift and diffusion of charge carriers were simulated leading to the charge signal induction according to the 3 μs shaping time of the electronic readout. Charge collection efficiency (CCE) was studied varying the particle track impact position within the geometry of the microdosimeter.

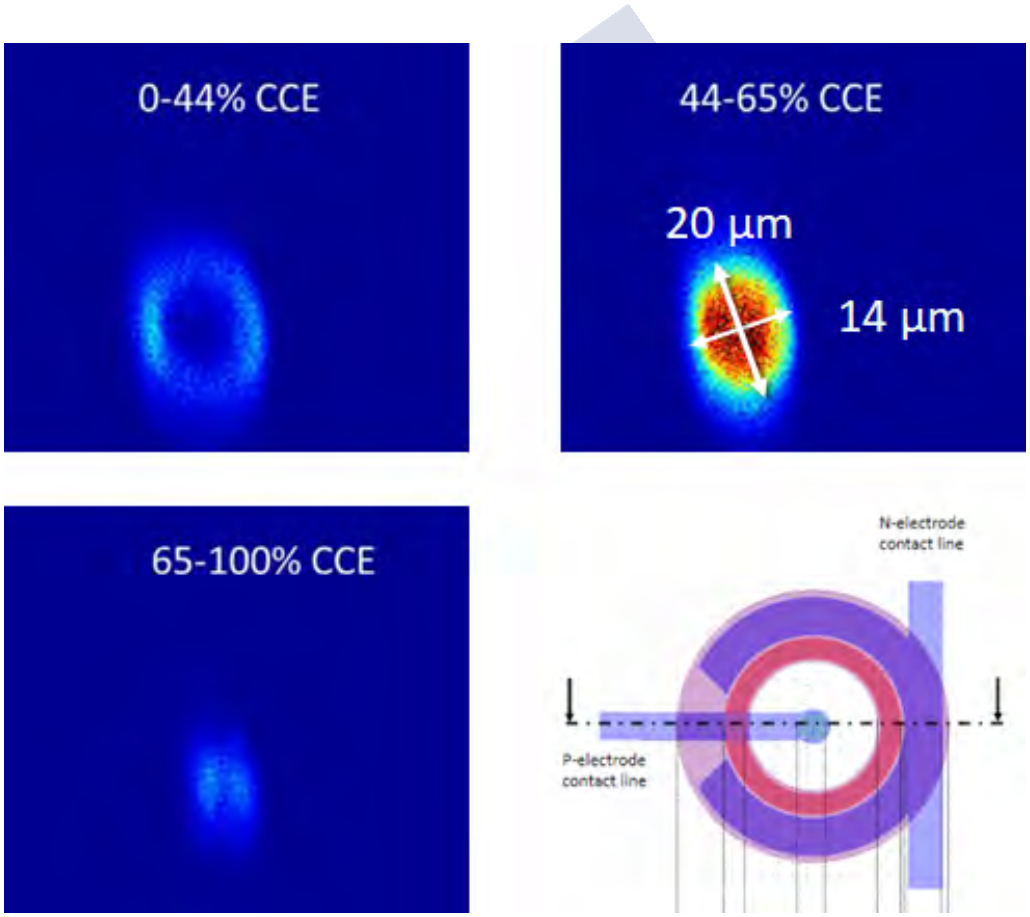

Figure 3.30: Maps of charge collection studies recorded at the IBIC test performed in CNA (Seville, Spain) with the IMB microcylindrical sensors.

Further experiments to verify the performance of the sensor and the CCE dependence were made with an IBIC test performed at the facilities of CNA in Seville, Spain, with protons of 600 keV kinetic energy. In those tests, the beam position was scanned following two-dimensional grid while the detector collected charge in each energy deposition event was recorded. A color coded two–dimensional graph with the position dependence of the signal is shown in figure 3.30. Normalised data is shown in figure 3.31. The charge collection efficiency (CCE) was calculated by normalizing the energy deposition values to the most probable energy deposition of the proton beam in the 5.5 μm silicon of the sensor and shown in this heat map, where blue indicates no counts and dark red indicates a large number of evens as shown in the scale in figure 3.30. It can be seen that most of the events apparently deposit less energy into the volume than expected, with a strong dependence on the position. Events with low charge collection efficiency occur in the periphery of the cylinder, whereas events with full CCE are more aggregated into the microsensor central region. These numerical results from the microbeam measurements and the CCE model are compared in next section.

Charge Collection Efficiency model

Considering the ^{12}C beam data, a first analytical model of the CCE was developed to try to reproduce and explain the experimental results together with the Monte Carlo simulations. To do that, in the simulations not only the imparted energy was recorded, but also the position and director cosines of the trajectory of the particles when they enter into the detector volume. The code is presented in appendix B. Ionization was generated in a 0.05 μm step voxel geometry, according to FLUKA distributions, along the straight line traversing the detector volume with an angle equal to the cosines of the particle. It was considered that for the particles and energy used the lateral straggling was negligible when compared with the dimensions of the detector [97]. Once the ionization cloud along the track is produced, each charge voxel is weighted with the point dependent model CCE function, and then all the weighted charge contributions are eventually added to obtain the expected signal of each event.

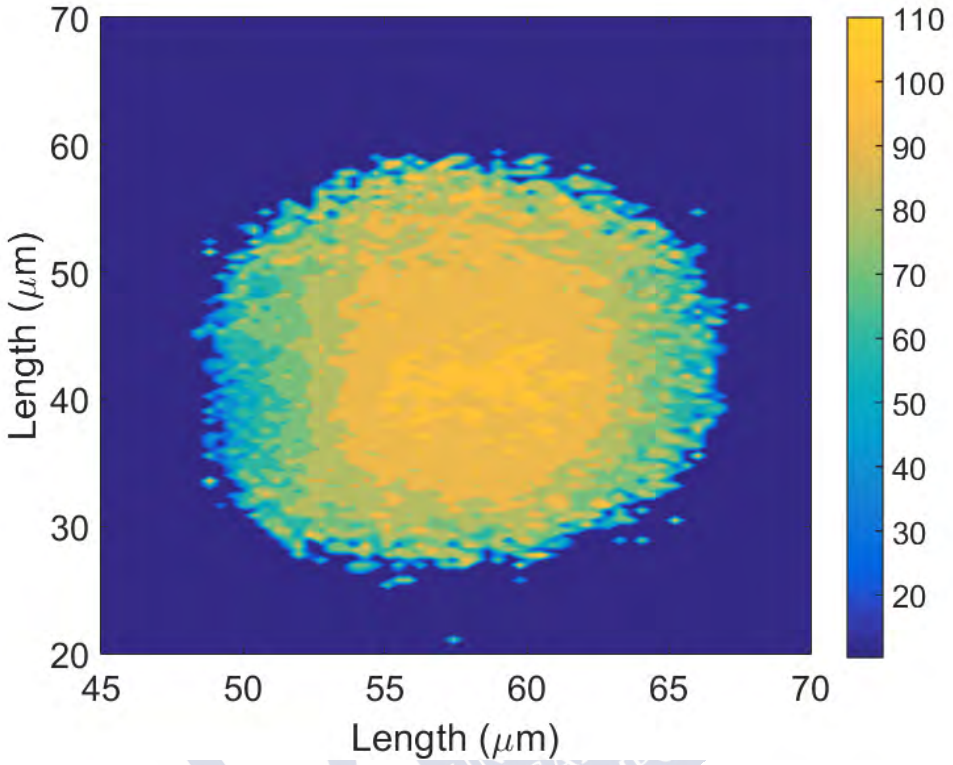

Figure 3.31: Normalised charge collection map recorded at the IBIC test performed in CNA (Seville, Spain) with the IMB 3D Cylindrical Microdosimeters. Legend shows the charge collection calculated for each pixel.

The phenomenological model constructed is based in exponential functions with dependence in both the distance to the central axis of the cylinder (r) and the depth traversed by the particle (h). Radial and vertical dependence are separated in the model. A six-parameter function was constructed as shown in the following equation:

$$F(r,z) = f(r) \otimes g(h) \tag{3.2}$$

$$f(r) = \left[\frac{1+e^{-g_r r_1}}{1-e^{-g_r r_2}}\right]\frac{1-e^{g_r(r-r_2)}}{1+e^{g_r(r-r_1)}} \tag{3.3}$$

$$g(h) = \left[\frac{1+e^{-g_h h_1}}{1-e^{-g_h h_2}}\right]\frac{1-e^{g_h(h-h_2)}}{1+e^{g_h(h-h_1)}} \tag{3.4}$$

where r and h are the values of the radius and height (from the geometrical centre of the cylinder), r_1 and h_1 are the points in which the CCE function reaches a value of 0.5, r_2 and h_2 are the points in which the function goes to zero, and g_r and g_z are the gradients of the exponential decay. Additionally, the vertical h component has a hard limit in h=2.75 μm due to the detector dimensions (thickness of 5.5 μm).

Parameter	**Value**
r_1	7.2 μm
r_2	20 μm
g_r	3.1 μm^{-1}
h_1	2.75 μm
h_2	10 μm
g_h	5.75 μm^{-1}

Table 3.1: Table showing the CCE parameter values for the model.

The values of the parameter models were obtained by a χ^2 minimization between the ^{12}C experimental data and the Monte Carlo smeared spectra, and its results are shown in table 3.1. Figure 3.32 shows the components of the charge collection efficiency model and its values as a function of the distance to the geometrical centre of the detector.

The model was then used to modify the response of the energy deposition along the ionizing particle tracks using the Monte Carlo simulations. Results are shown for several depths along the Bragg curve in figure 3.33. The smearing process provokes a shift on the peak position when compared with the un-smeared

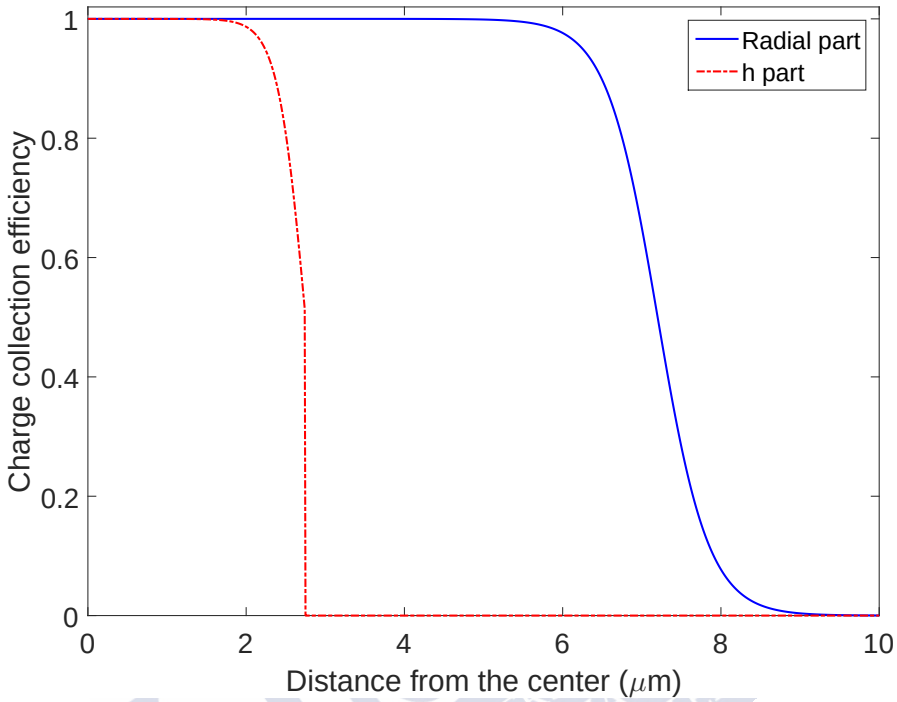

Figure 3.32: Graphic showing the behaviour of the two components of the CCE model with the parameters of table 3.1. All distances are from the geometrical centre of a 15 μm diameter and 5.5 μm width cylinder.

Monte Carlo spectra that varies in value all along the Bragg curve together with the appearance of a low pulse height tail due to events associated to low CCE regions in the sensitive volume. The lineal energy distribution peak shift and the charge collection efficiency varies depending on the ionization density along the track. After this correction was applied to the experimental spectra obtained in the CNAO experiment the smeared Monte Carlo and the experimental results agree significantly and the peak position discrepancy shown in figure 3.28 is corrected.

The peak shift corrections are proportional to lineal energy for all measured depths with the cylindrical microsensor up to the Bragg peak, as shown in figure

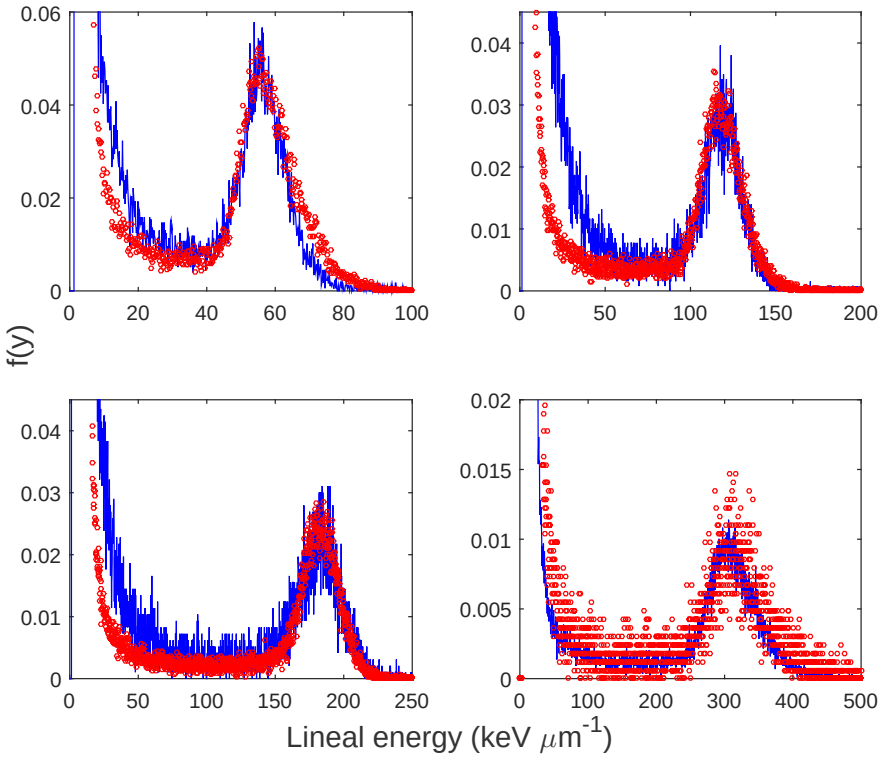

Figure 3.33: Comparison of smeared Monte Carlo simulations with experimental spectra. From top left, clockwise: 12.20, 25.20, 27.20 and 28.125 mm PMMA. Blue lines indicate smeared FLUKA Monte Carlo simulations, while red circles indicate the CNAO experimental measurements.

3.34. The uncertainties for all points in the figure is less than 5% (k=2). It remains unclear if this proportionality holds true for the low lineal energy region and more experiments with protons or other ion beams should be conducted to further understand the phenomena.

The model parametrization was also compared with both the TCAD simulations and experimental results from the IBIC test with proton ions in CNA. Figure 3.35 shows the comparison between the analytical model and the TCAD simulation whereas figure 3.36 shows the comparison between our model and the

IBIC experimental results. In the comparison with the IBIC beam its width was taken into account through a convolution between a Gaussian distribution with $\sigma = 2\mu$m and the analytical CCE model.

TCAD simulations shown in figure 3.35 have a significant agreement with the analytical model for distances bigger than $r = 2$ μm, whereas for smaller distances the TCAD simulation shows a relative difference of up to 12 % compared with the summarized model. This central charge collection deficit can be explained because in the simulation no charge is collected in the implant. This volume is typically dead to the charge collection and the analytical model in the simulation does not take it into account for its calculations. Nevertheless, this difference cannot be confirmed experimentally due to the limited sensitivity of the experimental data to the detailed actual charge collection behaviour in the

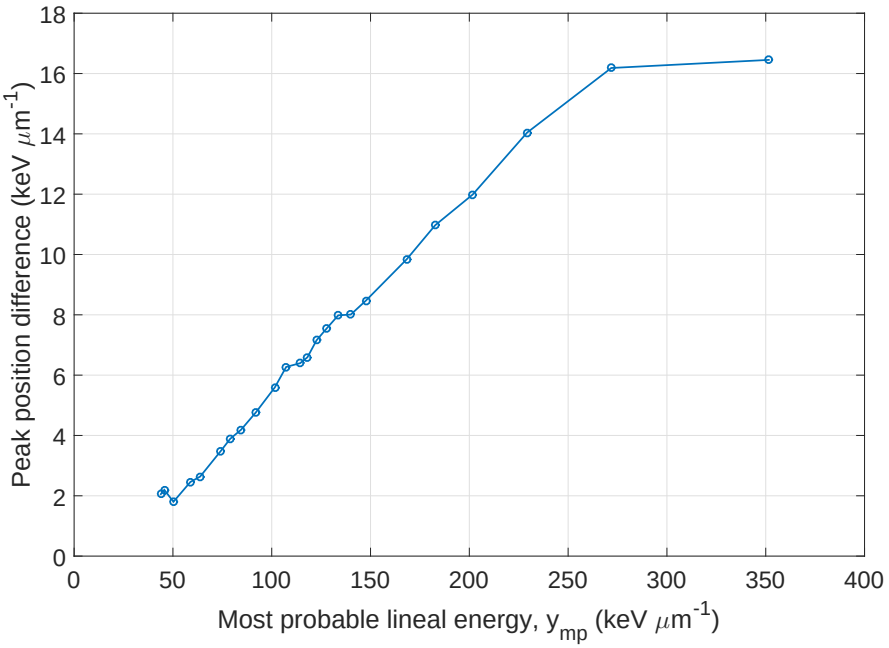

Figure 3.34: Peak shift in keV/μm for all measured points with the cylindrical microsensor along the Bragg curve as a function of the most probable lineal energy, y_{mp}.

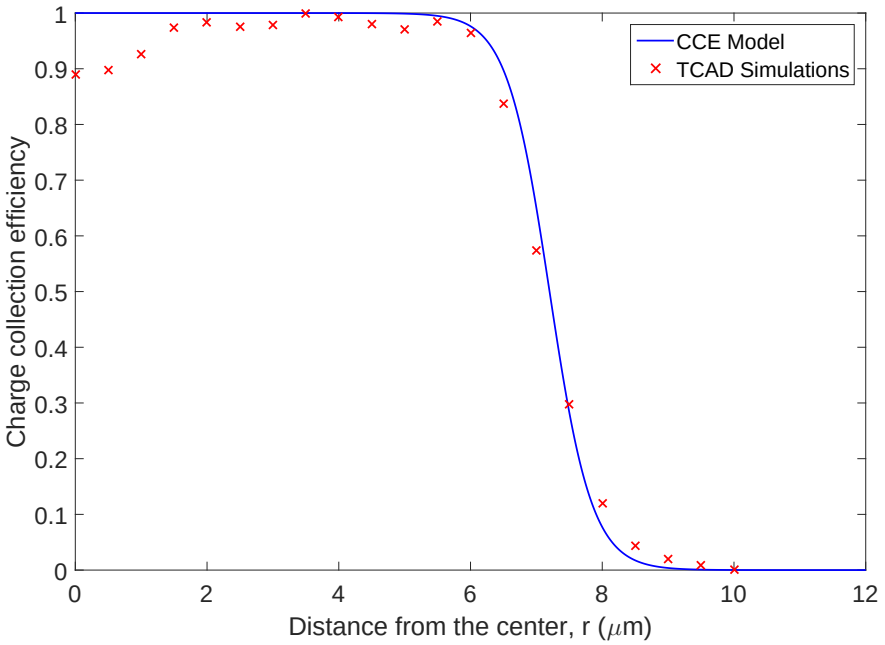

Figure 3.35: Comparison between the charge collection efficiency predicted from our model and from TCAD simulations results.

silicon microcylinder. In fact, the experimental results shown in figure 3.30 show additional effects as the lack of symmetry of CCE respect to the cylindrical sensor axis that was also varying between different individual cells.

The detectability problem

One of the main scopes in microdosimetry is the measurement of microdosimetric distributions at micrometric and submicrometric scale. In the case of submicron equivalent mass thickness devices, they would be sensitive to the track structure and charge cluster distributions in the material.

As we have seen previously the fidelity of reconstruction of microdosimetric spectra can be seriously compromised specially in the low lineal energy region by effects related to CCE in the small volume of the solid state microdosimeter. On

the other hand, as current devices have no intrinsic gain, there is additionally a physical limitation on the threshold of detection for low lineal energy. Although many possible designs are feasible, in terms of simplicity we have considered here a cylindrical geometry where the cylinder radius and its height are equal to certain dimension L. Considering a simple approach we have taken that the device capacitance and its leakage current depend linearly on the microdosimeter size parameter L. If we take a standard approximation for the ENC (rms of the noise charge) of the charge sensitive amplifier, this would have a behaviour

$$ENC = \sqrt{\frac{\alpha(C_{in}+\beta)^2}{\tau} + \gamma\tau(I_d+\delta) + \kappa}$$

whereas τ is the amplifier shaping time, C_{in} is the detector capacitance and I_d

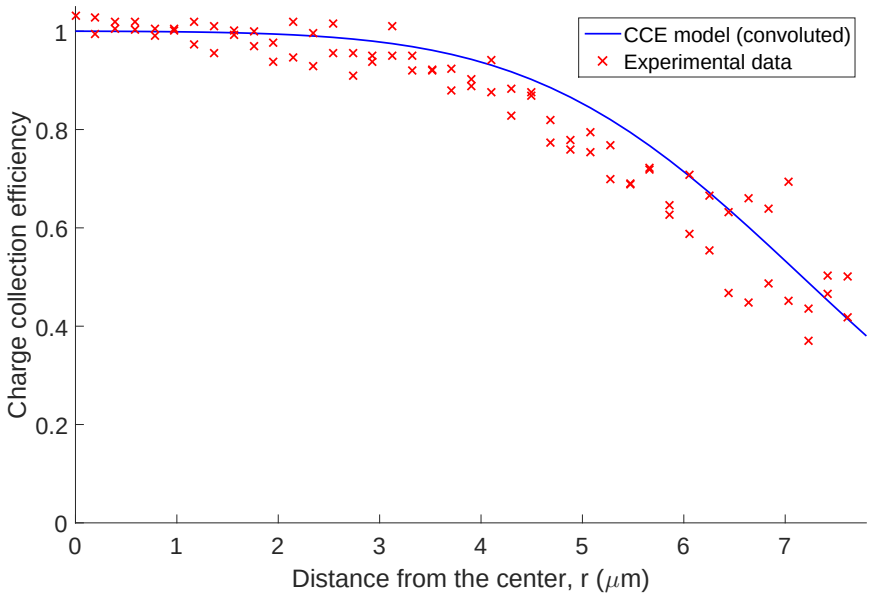

Figure 3.36: Comparison between charge collection efficiency results from the experimental test at CNA and from a convolution between a Gaussian distribution with $\sigma = 2\mu$m to take into account the finite width of the proton beam that contributes to smear the experimental CCE distribution.

the detector leakage current and α, β, γ, δ and κ are noise parameters associated to the electronic readout chain due to shunt and series resistance, sensor bias current and amplifier contributions [98, 99]. For this work we have considered sizes L of cylindrical microdetectors from 0.1 μm up to 40 μm with C_{in} ranging from 0.01 pF up to 5.3 pF and I_d from 0.3 pA up to 133 pA. These values were taken according to our experience with similar devices. We used the parameters from the state of the art electronics [100] to calculate that ENC would yield values between 250 up to 280 electrons for a shaping time of 1 μs respectively (α = 43 pF^{-2} μs e^2; β = 15 pF; γ = 8 μs^{-1} pA^{-1} e^2; δ = 800 pA; $\kappa = 5 \times 10^4$ e^2). We have restricted the track incidence to be parallel to the cylinder axis considered above, thus having $< l >= L$. For the noise separation we have assumed that the $FWHM$ equivalent noise energy would be 2.35 times the ENC multiplied by the average energy w per ion-electron pair, thus providing a threshold on the energy imparted detection taken as two times this $FWHM$ [98]

$$\varepsilon_{th} \geq 2 \times ENC \times 2.35 \times W$$

This provides also a corresponding limit on the lineal energy detection in the form of

$$y_{th} = \frac{\varepsilon_{th}}{< l >} \geq \frac{4.7 \times ENC \times W}{< l >}$$

Thus we can evaluate the corresponding limits for the detection of the lineal energy considering these cylindrical microdetectors of different size L. Figure 3.37 shows the limits on the detection of lineal energy as a function of the detector size with ENC values ranging from 250 to 280 electrons. In this Figure we have included both silicon and diamond sensors just to guide the reader in terms of the physical limits expected from the different characteristics of the sensitive media.

The capability to extend the detection range to 1 keV/μm would be achieved in silicon when the size of the microsensor is equal or bigger than 4.4 μm while in the case of diamond this would imply a sensor of 16 μm thickness. Additionally, it is clear that sub-micron microdosimeters would be only useful for highly ionizing

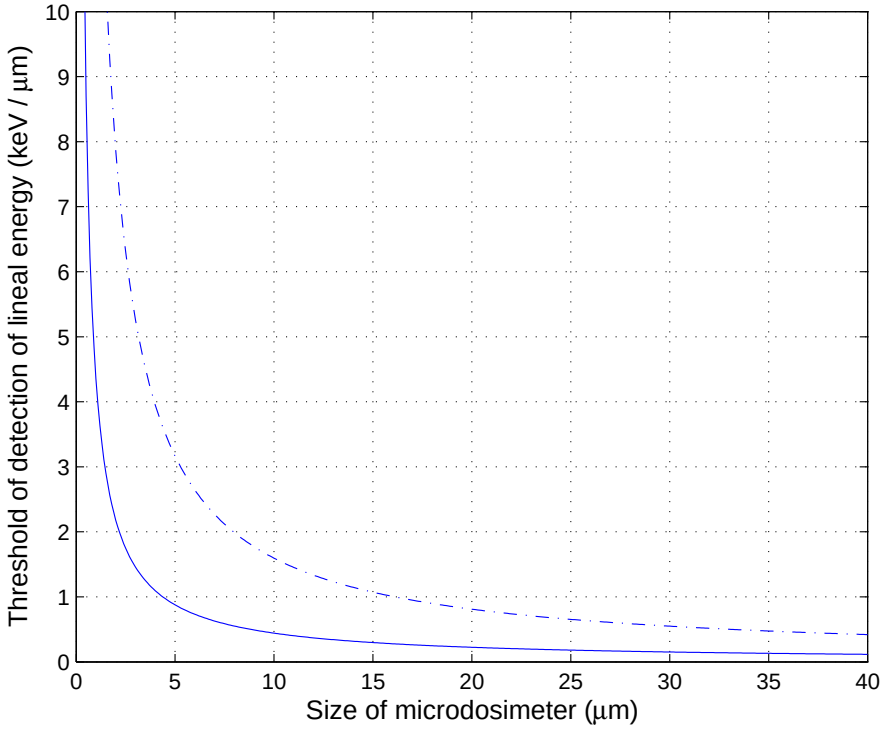

Figure 3.37: Limit of detectability for lineal energy in cylindrical micro–dosimeters with equal diameter and height L as a function of L. Continuous line is calculated for silicon and dashed line corresponds to diamond.

particles, since for silicon (diamond) devices of 1 μm we would only be able to detect radiation with lineal energy over 4.5 keV/μm (15.7 keV/μm). This conclusion tends to exclude the feasibility of solid state microdosimeters as adequate devices for track structure measurement in the region around 0.1 μm or below, at least for non intrinsic gain sensors. In fact the use of devices of tenths of microns would yield values closer to the Linear Energy Transfer (as a macroscopic magnitude) than the stochastic lineal energy considered in microdosimetric distributions. Of course, the results of this section could be recalculated considering the particular electronic noise considering the particular sensor characteristics and the readout under study.

Chapter 4

Experimental validation of the microstructured 3D thin silicon sensors

Summary of the chapter:

In this chapter the experimental results obtained with the thin microstructured silicon detectors described in the previous chapter are presented, showing how can they characterise monoenergetic ^{12}C ion beams. Results are compared with FLUKA Monte Carlo simulations, showing great agreement between them.

Several tests were performed to evaluate the performance of the microdosimeters described in the previous chapter in carbon ion beams.First, the U3DTHIN microdosimeters were tested with ^{12}C ions at GANIL (Caen, France) to check its behaviour under irradiation. Next, the following generation of microsensors (3D cylindrical microdosimeters) was tested with both proton and ^{12}C ion beams at the installations of Fondazione CNAO (Pavia, Italy), a public Italian particle therapy facility. For all tests, results were compared with Monte Carlo simulations using FLUKA.

4.1 Methods

4.1.1 Experimental set-up

The experimental set-up for each of the different experiments performed followed the same pattern. After the beam monitoring system, a motorized PMMA wedge and the microdosimeter detection system were placed in a plane perpendicular to the beam direction.

The wedge system was composed by two equal 10° angle wedges made of 1.186 g/cm^3 PMMA that provided a continuous variable thickness from 3 mm up to 30 mm (40 mm in the CNAO set-up) with an uncertainty of around 40 μm for the GANIL experiment and 80 μm for the CNAO one. The relation between wedge position and thickness was calculated using a second-order polynomial fit. Figure 4.1 shows the relation between wedge position and thickness for both the GANIL and CNAO measurements. Residuals for both quadratic fits are shown in figure 4.2. The root mean square of the residuals was employed to calculate the uncertainty of the wedge position.

Figure 4.3 shows a sketch of the experimental set-up.

In GANIL, the ^{12}C 94.983 MeV A^{-1} beam was delivered at the G4 experimental area of the facility. Beam profile was tuned to have an approximate FWHM of 7 mm at the beam pipe exit window to provide a uniform irradiation of the detector active area with an intensity around 10^4 particles per second with

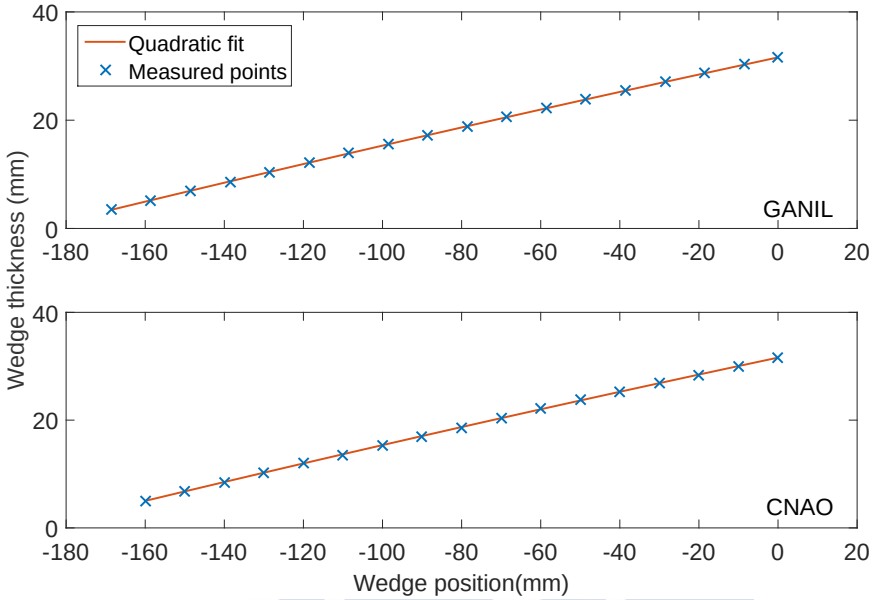

Figure 4.1: Second order polynomial fit between wedge position and thickness for the wedge systems employed in the GANIL and CNAO tests.

an average fluence rate at the detector of $2.4{\times}10^4$ s^{-1} cm^{-2}.

The expected longitudinal range of the carbon ions in PMMA was 20.5 mm, being sampled with steps of several mm in the stopping power plateau region and with sub-millimetric precision close to the Bragg peak. The low-level discrimination threshold for the signal was set approximately to 200 keV in silicon. For each depth, several spectra of the diode signal were acquired with a total integration time of 200 s each.

For the CNAO tests, ^{12}C particles with a kinetic energy of 115.23 MeV A^{-1} were used. The beam had an approximate diameter of 20 mm, with a Gaussian profile with a FWHM of 5.1 mm along the horizontal axis and 8.5 mm along the vertical axis at the nozzle providing full irradiation of the detector active area. The average fluence rate was 5×10^7 s^{-1} cm^{-2} and for each measurement a total number of approximately 10^9 carbon ions were delivered.

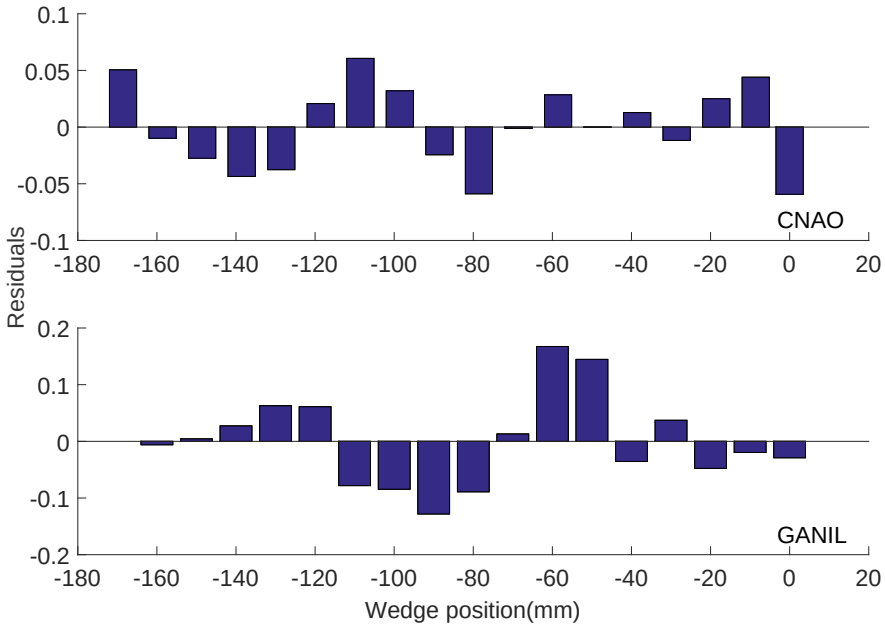

Figure 4.2: Residuals of both second order polynomial fits between wedge position and thickness for the wedge systems employed in the GANIL and CNAO tests.

The expected longitudinal range according to SRIM [29] for carbon ions in PMMA with the energy employed was 28.47 mm. The Bragg curve was sampled taking spectra in steps of several millimetres in the plateau region and sub-millimetre steps in the proximity of the Bragg peak.

4.1.2 FLUKA Monte Carlo

Analysis of the experimental work required a detailed simulation of the beam interactions and radiation transport. Although there are different choices for carbon ion beam Monte Carlo codes with very good agreement with the experimental data, there are still some uncertainties in the benchmarking of nuclear models [82]. Due to previous experience with that Monte Carlo code, FLUKA was employed to compare with experimental data, and a discussion on the cap-

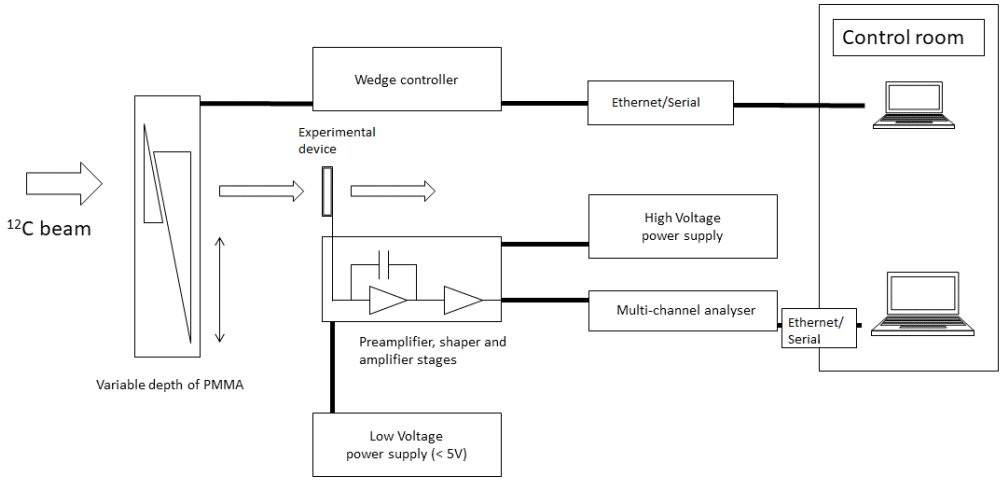

Figure 4.3: Schematic of the experimental setup used in all the experiments presented in this chapter.

abilities and settings employed for the simulations can be found in section 2.6.1.

The code was benchmarked against experimental results performed with a PTW Peakfinder variable water column and a PTW 34080 Bragg-Peak chamber in a monoenergetic 115.2 MeV A^{-1} ^{12}C ion beam with a detailed simulation of the ionisation chamber. The water mean ionisation potential was changed from the default value of 75 eV provided by FLUKA to 77 eV in order to match the water depth dose curve [21, 101]. Figure 4.4 shows the difference in the Bragg peak position in the depth dose profile measured by a Bragg-peak ionisation chamber arising from the change of the ionisation potential in the simulation settings.

Several runs were executed, changing the depth of water traversed by the primary particles in each one. The simulations were performed with five cycles of 2×10^4 particles each, amounting to 10^5 particles for each water depth. No variance reduction techniques were employed in any Monte Carlo simulation.

A comparison between Monte Carlo and measured ionisation chamber points is shown in figure 4.5. The local relative difference between experimental and simulation is less than 4% for all points along the Bragg curve, although the

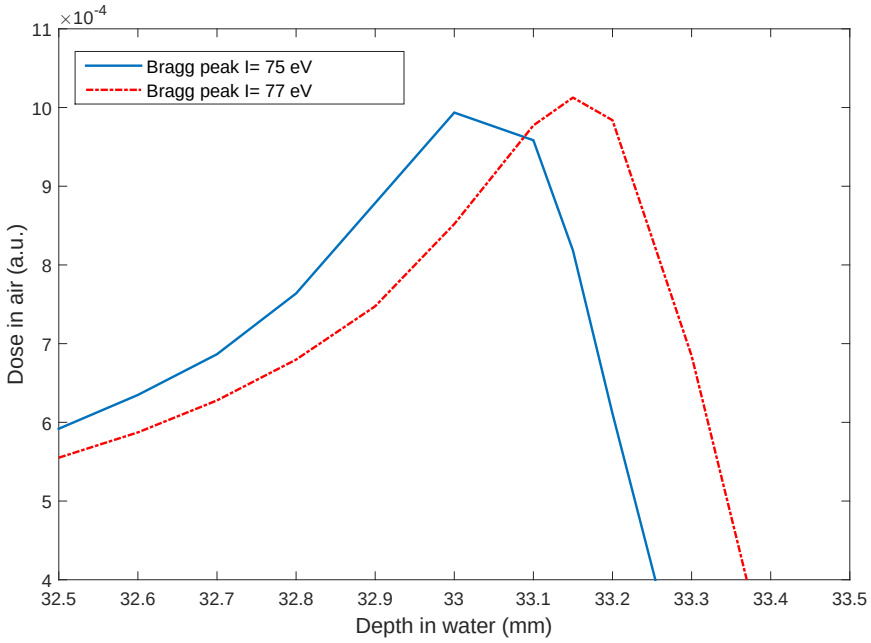

Figure 4.4: Change in the Bragg peak position due to the variation of the mean ionisation potential parameter in water for a 115.2 MeV A^{-1} ^{12}C ion beam.

difference is higher in the distal tail. It can be concluded that the benchmark of the code was successful and can be safely used for hadrontherapy applications for protons and heavy ions.

The same FLUKA Monte Carlo settings were used for the silicon microsensor simulations. The estimated statistic uncertainty for the simulation of the absorbed energy on 10 μm of silicon in the plateau region of the Bragg curve was less than 1% overall for the U3DTHIN detector, and less than 2.5% in 5.5 μm for the 3D cylindrical microsensors.

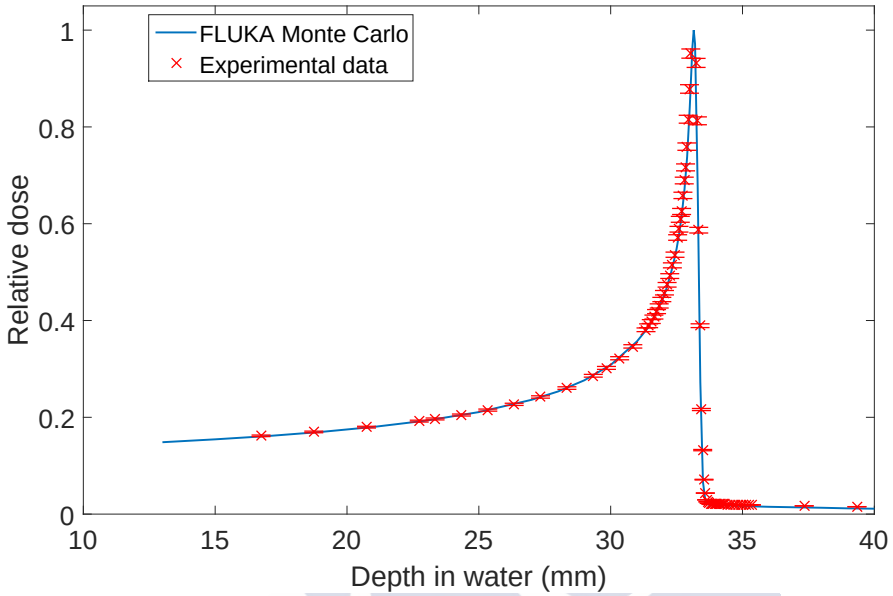

Figure 4.5: Commissioning of the FLUKA Monte Carlo against the water depth dose of a 115.2 MeV A^{-1} ^{12}C ion beam measured with a PTW 34080 Bragg-Peak chamber.

4.2 Experimental Results

4.2.1 Results and discussion

In all cases, data was analysed and compared with different Monte Carlo simulations made with FLUKA. The ion beam was propagated in PMMA in FLUKA with several depths to reconstruct a Bragg curve and then propagated in a detailed geometry of the detector electronic setup, with detector thickness of 10μm in the U3DTHIN case and 5 μm for cylindrical microdosimeters. Results from microdosimeters were not compared with a reference microdosimetric spectra from a standard TEPC for experimental validation.

The imparted energy ε is considered proportional to the silicon detector signal while the mean chord length $\bar{l}$ is approximately equal to the detector thickness for

frontal irradiation. This was further confirmed by evaluating the particle track length on the Monte Carlo simulations up to the Bragg Peak, resulting in values equal to the active area thickness with an error estimate of less than 1%.

GANIL test with U3DTHIN detectors

For the comparison of the data a three parameter minimization of a χ^2 type function was performed between the most probable value of the experimental lineal energy distribution $S_{exp}(z_i)$ at a certain depth z_i and that from Monte Carlo code $S_{MC}(z_i)$,

$$\chi^2(N,\Delta) = \sum_{i=1}^{n} \frac{(N \times S_{exp}(z_i) + \Delta - S_{MC}(z_i))^2}{U_i^2} \tag{4.1}$$

Where N corresponds to the ADC channel to lineal energy coefficient in keV μm^{-1} adc^{-1}, Δ is the signal pedestal in keV μm^{-1} and U$_i$ is the combined total uncertainty of each difference in the numerator.

The results exhibit an excellent agreement for N=(1.083±0.032) keV μm^{-1} adc^{-1} with Δ= (3.3±1.5) keV μm^{-1} and ζ=(0.012±0.074) mm, shown in figure 4.6 between data and FLUKA. The most probable value of the lineal energy distribution was employed in order to avoid possible effects of the experimental pulse height distribution. Local deviations between the experimental values and model prediction are below 2% for all points up to 19.875 mm depth in PMMA.

Frequency and microdosimetric distributions $f(y)$ and $y\ d(y)$, respectively, obtained from both Monte Carlo codes and experimental data for the depths of 7, 15, 19, and 20 mm are shown in figures 4.7 and 4.8.

It is easy to appreciate that experimental distributions for $y\ d(y)$ in the proximal Bragg peak area have lower peak values than Monte Carlo ones. This is due to the fact that experimental distributions exhibit higher spread of signals both at lower values of the peak region and also at higher values. There is also some fraction of pile-up events with double pulse height in the silicon detector with a statistical fraction that reaches 4% of the total event number.

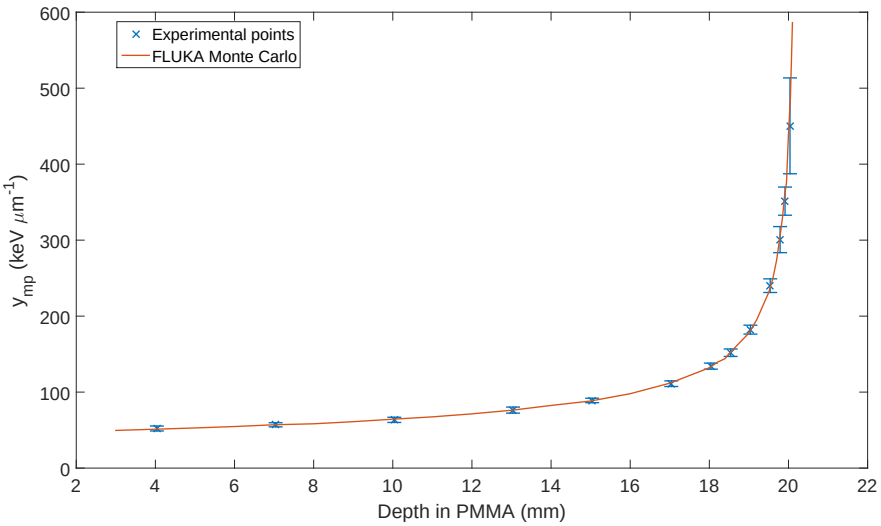

Figure 4.6: Comparison of the most probable lineal energy experimental (crosses) and FLUKA Monte Carlo (solid line) values in the silicon detector for the U3DTHIN detectors in GANIL.

This affects the actual normalization of the distribution and the scoring of the fluence averaged lineal energy. On the other hand, the Monte Carlo distributions and data for depths higher than 19 mm are hard to compare because close to the Bragg peak, small changes in the effective mean ionization potential, energy and range straggling and primary ionization fluctuations affect these distributions dramatically. Additionally, it is possible that the experimental data is affected by columnar recombination in the close-to-Bragg peak region.

If the dose averaged lineal energy $\bar{y}_D$ is calculated from our set of microdosimetric distributions a summarized behaviour of the different simulations and measurements can be obtained. It is important to understand that when energy-loss straggling and delta-ray escape from the studied volume are not very relevant, $\bar{y}_D$ value is very close to dose averaged LET [102]. Of course, this statement implies that the ionizing particle range is significantly higher than the scoring region. In general terms the agreement between the experimental data and Monte Carlo

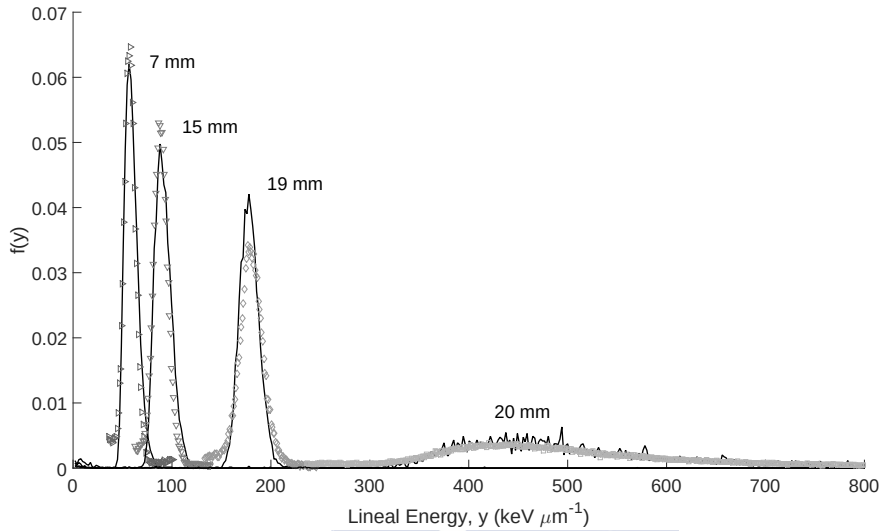

Figure 4.7: Probability distributions $f(y)$ in silicon from experimental data and FLUKA and at different depths in PMMA (see text) for the U3DTHIN detectors in GANIL. Solid lines represent Monte Carlo simulations, whereas the different symbols represent the experimental distributions.

shown in figure 4.9 is better than 5% (local) up to the Bragg-peak.

CNAO test with 3D Cylindrical microdosimeters

To compare the data and the simulations the same three parameter minimization of a χ^2 function employing the most probable value for a given PMMA depth (z_i) of both experimental ($S_{exp}(z_i)$) and Monte Carlo ($S_{MC}(z_i)$) distributions, as in the U3DTHIN case, was employed. Experimental distributions were corrected to avoid a systematic error in the alignment of the wedge system during the experiment, giving a large correction factor for thickness. Eq. 4.1 shows the relation between the parameters and the distributions.

The minimization yielded the following results for N = (0.856±0.021) keV μm^{-1} adc^{-1}, Δ = (-2.7±1.2) keV μm^{-1} and ζ=2.18 (16) mm. Figure 4.10 shows a remarkable agreement between the experimental and simulated data with those

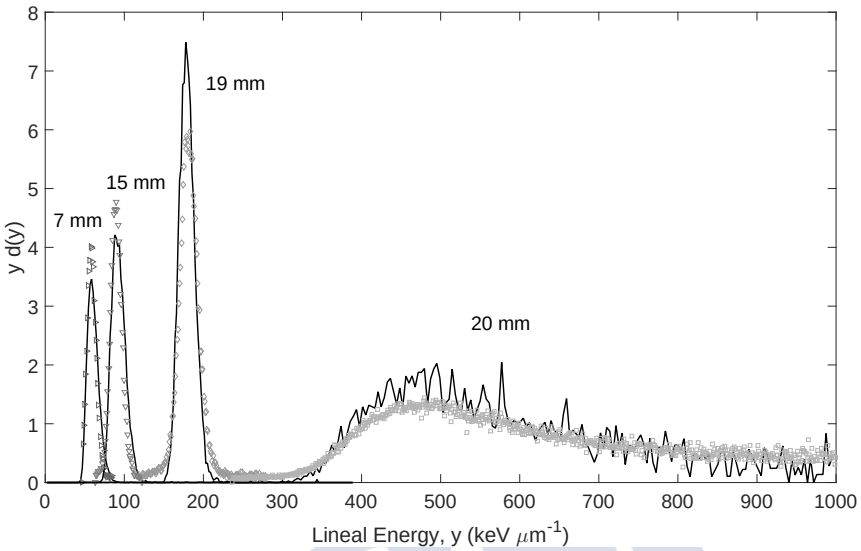

Figure 4.8: Microdosimetric distributions $y\ d(y)$ in silicon from experimental data and FLUKA Monte Carlo at different depths in PMMA (see text) for the U3DTHIN detectors in GANIL. Solid lines represent Monte Carlo simulations, whereas the different symbols represent the experimental distributions.

parameters.

In general, the agreement between the experimental points and the Monte Carlo curve is good, but some points showed pile-up effects that modified the experimental value. This was minimizing by applying cut-offs in the experimental distributions at high energies. These cut-off values were decided by evaluating the Monte Carlo distributions and comparing them with the experimental ones to assure no real data was being modified, approximately at twice the peak value.

A comparison between the experimental and Monte Carlo $f(y)$ distributions is presented in Fig. 4.11. In the figure are shown the spectra for depths of 12.2, 25.2, 27.2 and 28.125 mm respectively. Although the agreement between experimental and Monte Carlo most probable lineal energy is remarkable, the normalization of the experimental spectra presents some problems that affect the scoring of the fluence averaged lineal energy. Charge collection efficiency modifies

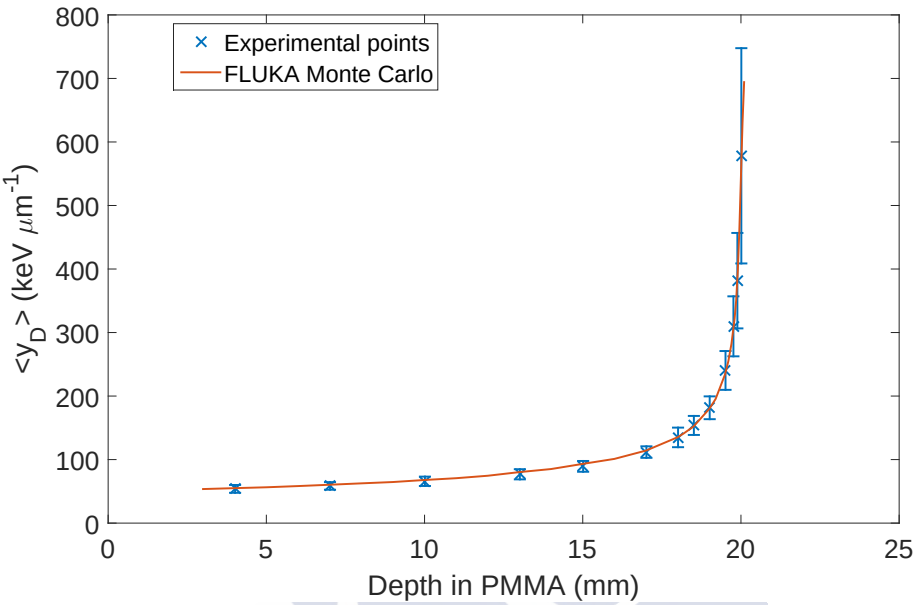

Figure 4.9: Dose averaged lineal energy experimental (crosses) and FLUKA Monte Carlo (solid line) computed values in the U3DTHIN silicon detector at GANIL.

the shape of the spectra and the position of the peak as discussed in section 3.4. In the case of spectra close to the Bragg peak (27.2 mm and 28.125 mm) the linear energy distribution peak position does not adjust very well as depths in the proximal Bragg peak area are difficult to compare since dependence on the effective mean ionization potential can modify the shape of the distributions at these depths [21, 101].

Microdosimetric spectra for the same PMMA depths as in figure 4.11 were also calculated. The results are shown in figure 4.12. Although the general agreement between measured and simulated most probable values is remarkable, there are differences in the shapes of the distributions due to partial charge collection in the active volume and pile-up events at high energies modifying the spectra due to the way $yd(y)$ is calculated, cross-talk from the other active areas and baseline shift at different energies, as well as noise added by the amplification

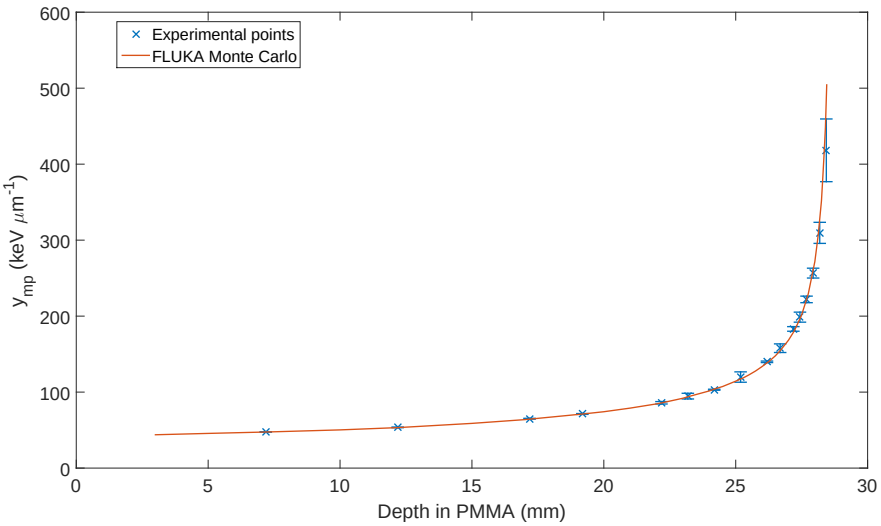

Figure 4.10: Most probable lineal energy comparison between experimental data (dots) and FLUKA Monte Carlo simulations (solid line) for the CNAO test with 3D cylindrical microdosimeters.

stage and differences between the simulation geometry and the real geometry of the experiment. To add to that, the same problems as figure 4.11 are also present here.

Dose averaged lineal energy distributions are presented in Fig. 4.13.

4.2.2 RBE Calculations with 3D cylindrical microdosimeters

In treatment planning, RBE is used to transform the physical dose delivered into a biological dose (or RBE-weighted dose) that considers the effects other than the radiation-matter interaction. Due to strong RBE dependence on both physical and biological parameters, RBE must be described by more or less complex models instead of using a simple factor. There are different models described in the literature [50–54] based on *in vitro* data.

An RBE calculation based on the microdosimetric kinetic model (MKM) was

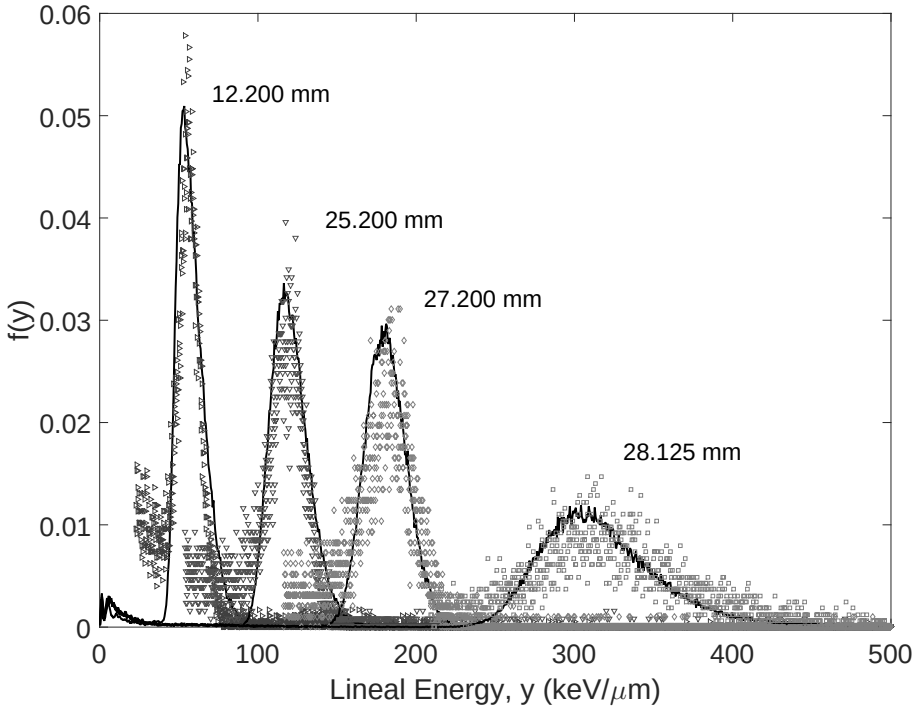

Figure 4.11: Probability distributions $f(y)$ in silicon from experimental data and FLUKA and at different depths in PMMA (see text) for the 3D Cylindrical microdosimeters in CNAO. Solid lines represent Monte Carlo simulations, whereas the different symbols represent the experimental distributions.

performed using the data acquired in CNAO. In this formulation the number of lethal events is modelled as proportional to the square of the specific energy, z, and the cell nucleus is supposed to be divided into small domains of finite size of cylindrical shape (with R_n being the radio of the cell nucleus and r_d the radius of the domain). The parameters of the linear-quadratic model obtained from the MKM corrected model [103,104] depend on a saturation corrected, dose weighted specific energy produced by a single event (z^*_{1D}).

The saturation correction considers the "overkill" effect observed when a cellular line is irradiated with high LET radiation. Under this assumption, a given

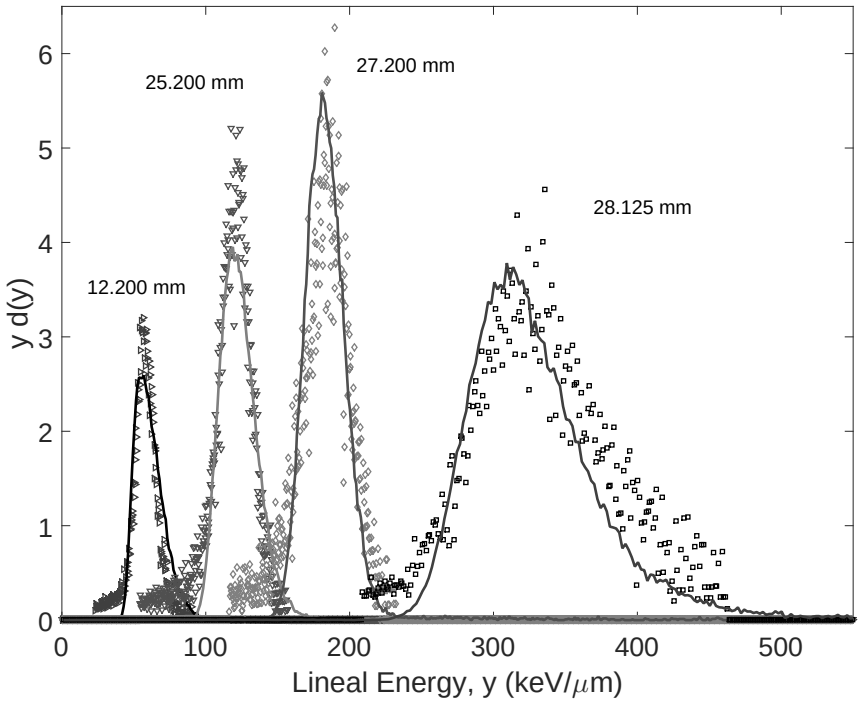

Figure 4.12: Microdosimetric distributions $y\ d(y)$ in silicon from experimental data and FLUKA and at different depths in PMMA (see text) for the 3D Cylindrical microdosimeters in CNAO. Solid lines represent Monte Carlo simulations, whereas the different symbols represent the experimental distributions.

dose of radiation is needed to kill the cell with total probability. If the cell is exposed to a higher dose of radiation, the remaining radiation is somehow wasted in a cell that is already dead and cannot affect other sites.

$$z^*_{1D} = \int_0^\infty z_{sat} z f(z) dz \tag{4.2}$$

where z_{sat} is given by

$$z_{sat} = \frac{z_0^2}{z}\left[1 - exp\left(-\frac{z^2}{z_0^2}\right)\right] \tag{4.3}$$

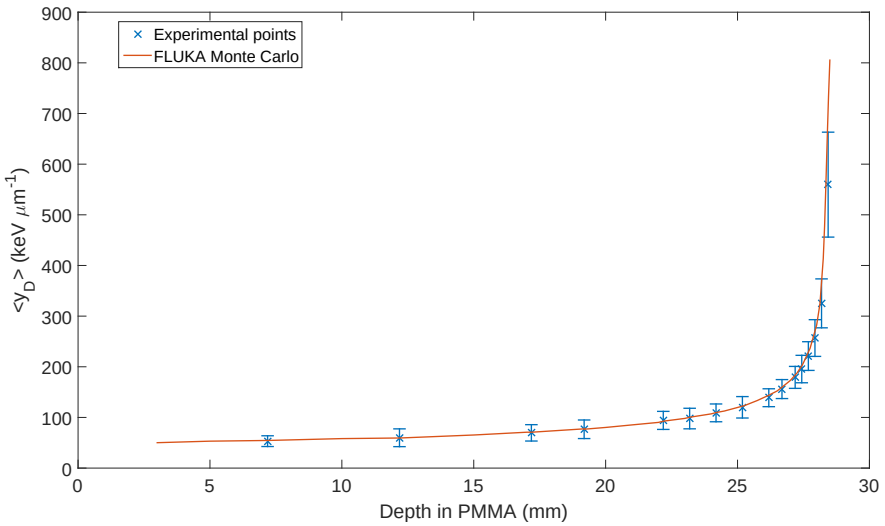

Figure 4.13: Dose averaged lineal energy experimental (crosses) and FLUKA Monte Carlo (solid line) computed values in the silicon detector for the 3D Cylindrical microdosimeters in CNAO.

And the characteristic saturation parameter, z_0

$$z_0 = \frac{(R_n/r_d)^2}{\sqrt{\beta[1+(R_n/r_d)^2]}} \tag{4.4}$$

The values for R_n and r_d have to be specified to get z^*_{1D}. In this work, the values for aerobic human salivary gland (HSG) cells were used, with $r_d = 0.32$ μm [104].

Considering that the quantity $\alpha_0 + \beta z^*_{1D}$ can be rewritten as α_{MKM} due to its resemblance to the α of the LQ model we can obtain the radiobiological efficiency using:

$$RBE = D_{ref}(S)\left[\frac{-\alpha_{MKM} + \sqrt{\alpha^2_{MKM} - 4ln(S)\beta}}{2\beta}\right]^{-1} \tag{4.5}$$

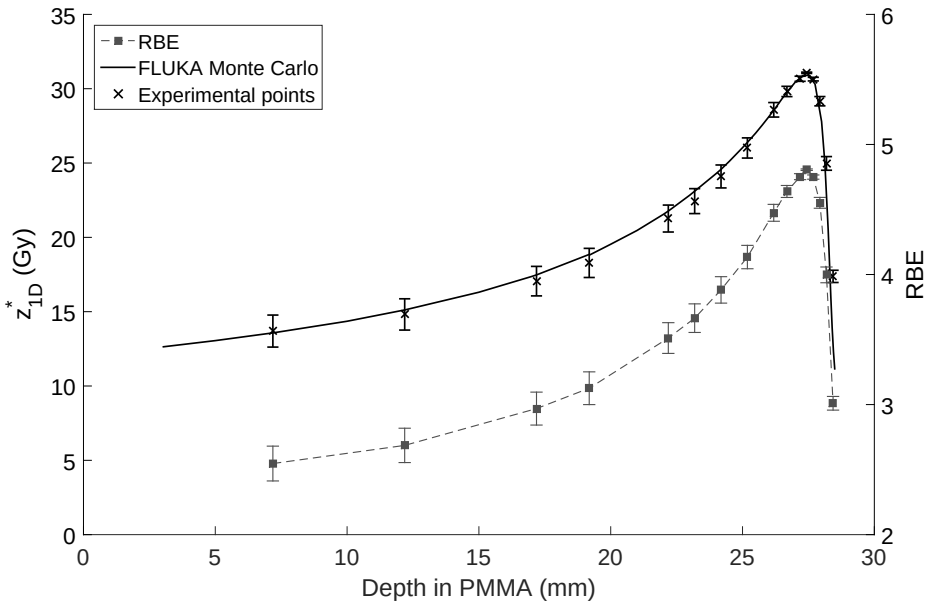

Figure 4.14: Experimental z^*_{1D} values from the CNAO ^{12}C ion beam (crosses) compared to FLUKA Monte Carlo (solid line). Additionally, RBE values for experimental points (squares and dashed line) are shown.

From the microdosimetric behaviour of the radiation in the energy transfer to cells, radiation weighting factors can be obtained. Lineal energy distributions can be benchmarked to a Monte Carlo model to aid experimental methods and perform beam characterization [18, 19]. To obtain the experimental data, adequate instrumentation for the measurement of the microdosimetric quantities is needed.

To evaluate RBE and z^*_{1D} from experimental data, the imparted energy values in the microdosimeter (silicon) were converted to imparted energy in water using a look-up table of stopping power values taken from [29]. The values used to calculate the radiation endpoint in order to get the RBE were the same as [104], coming from HSG cells. Figure 4.14 shows the comparison between experimental and Monte Carlo z^*_{1D}, and the RBE calculation for the experimental spectra.

Although experimental values agree in general with Monte Carlo, this agreement is limited. Events detected at high energies alter the average values, but these events can be explained due to pile-up in the detector volume. Additionally, cross-talk noise coming from other sensitive volumes, as all the sensitive volumes are connected to the same ground, and electronic noise coming from the amplification stage add further uncertainties. There is also a limitation in the dynamic range of the instrumental setup, partial charge collection and the need for the conversion from silicon measured specific energy to water. Thus, the evaluation of z^*_{1D} includes uncertainty components from experimental cut-off values and the limitation of the algorithm employed for this transformation.

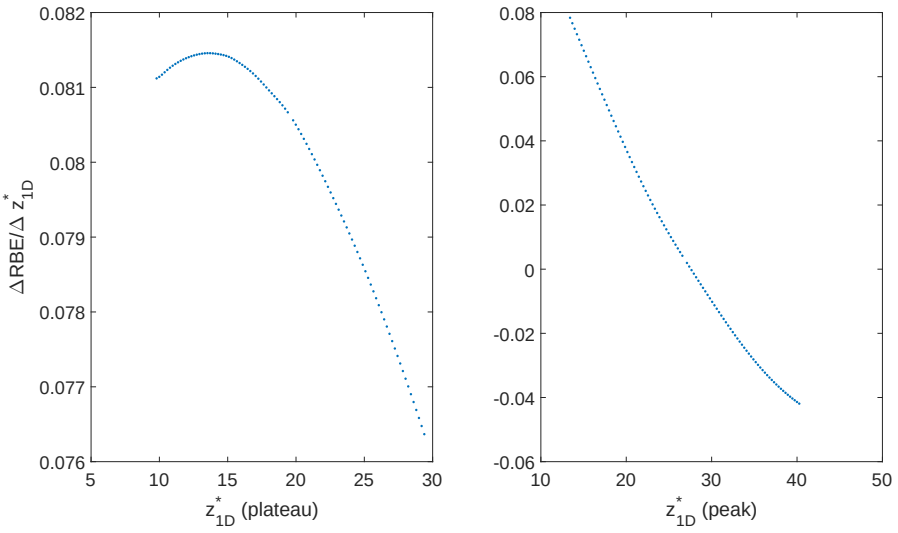

Figure 4.15: Sensitivity of the RBE function to changes in the saturated specific energy, z^*_{1D}. The figure shows the RBE sensibility in terms of the relative variation of the input parameter z^*_{1D}, for two different positions along the Bragg curve, the plateau (left), and the proximal Bragg peak area (right).

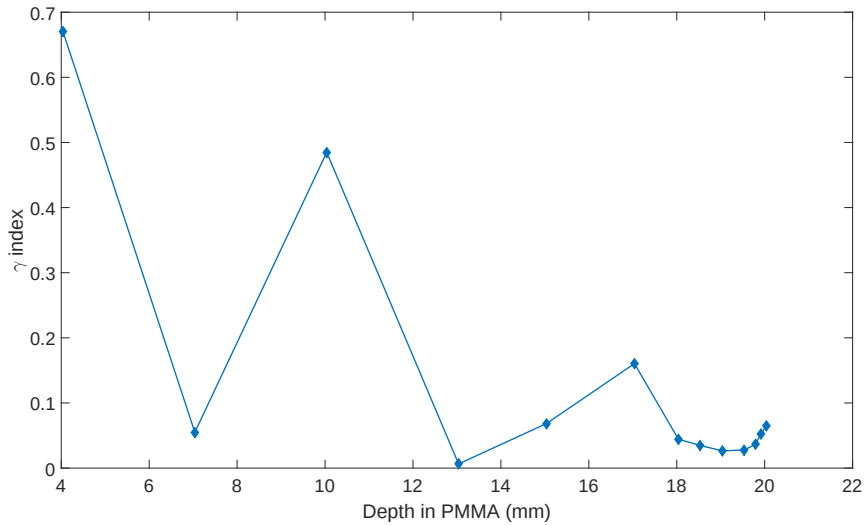

Figure 4.16: Gamma function for the most probable lineal energy obtained from experiment and FLUKA for the most probable values of lineal energy in the GANIL test. Tolerances are 2% of the most probable energy for each point and 0.5 mm.

4.2.3 Study of the uncertainty of RBE

The aim of measuring lineal energy in particle therapy is the evaluation of biological dose. Thus, the issue of knowing how the uncertainty of microdosimetric distributions translates to RBE uncertainty is important. Also, to evaluate the agreement between the experimental data and Monte Carlo distributions presented in this chapter a Gamma test [105] was employed. The tolerances were chosen attending to the clinical precision needed in particle therapy; in particular, tolerance for the PMMA thickness was chosen as 0.5 mm. To select the lineal energy tolerance, RBE sensitivity to microdosimetric spectra variation was studied by assessing the effect on RBE of the variations on imparted and specific energy.

By varying the input lineal energy used for the RBE calculation by a certain value (from 50 % to 150% of the experimental value) the variation in the RBE was evaluated. Due to the saturation effect applied in the RBE calculations, the

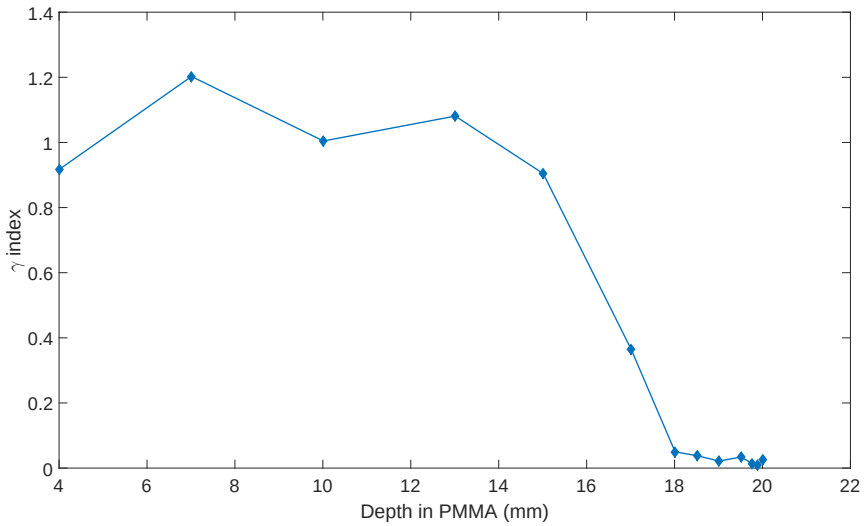

Figure 4.17: Gamma function for the dose-averaged lineal energy obtained from experiment and FLUKA for the dose averaged lineal energy in the GANIL test. Tolerances are 2% of the most probable energy for each point and 0.5 mm.

variation of the RBE values was more prominent in the plateau area of the Bragg curve than in the proximal peak area. Figure 4.15 shows the sensitivity of the variation as a function of the input lineal energy for the plateau and proximal Bragg peak areas. The thicknesses of the PMMA were 7.2 mm and 27.4 mm for the plateau and the proximal Bragg peak area, respectively, corresponding to the first (plateau) and maximum (Bragg peak) points in the plot of figure 4.14. Given an uncertainty of ∼10% in z^*_{1D}, a relative uncertainty of ∼6% is expected in RBE.

As the RBE varies greatly along the Bragg curve, and the effect of the variations in the lineal energy is so different depending on the point of the curve under evaluation, it was decided that each experimental point of the Bragg curve would have a different tolerance value, equal to 2% of the Monte Carlo lineal energy value at each point. This avoids the problem of choosing a value too small or too large for any one of the points along the Bragg curve.

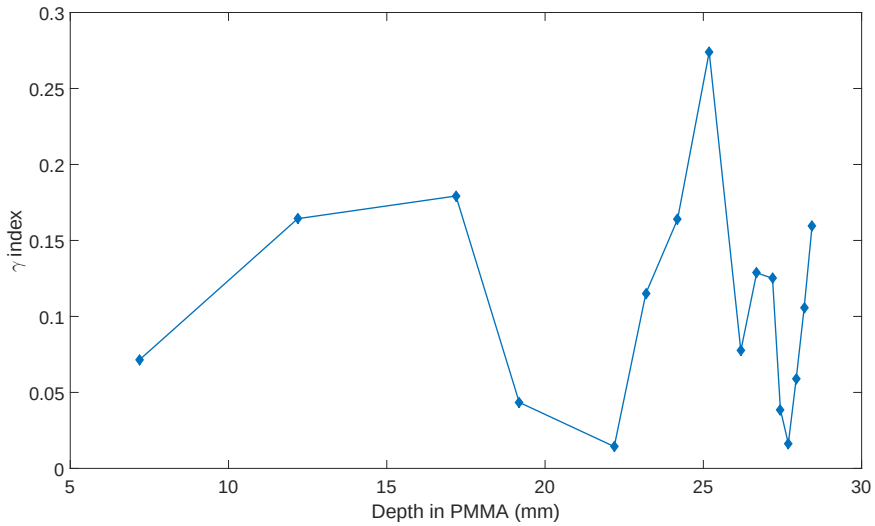

Figure 4.18: Gamma function for the most probable lineal energy obtained from experiment and FLUKA for the most probable values of lineal energy in the CNAO test. Tolerances are 2% of the most probable energy for each point and 0.5 mm.

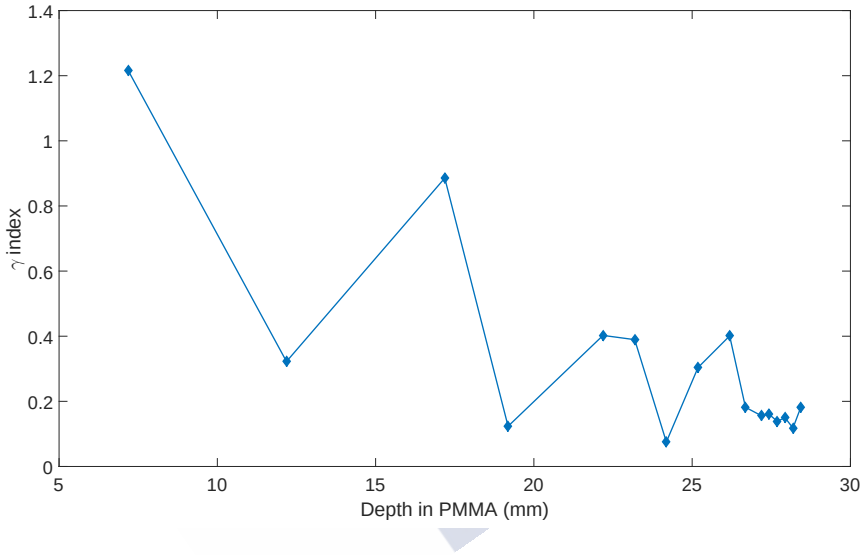

Figure 4.19: Gamma function for the dose-averaged lineal energy obtained from experiment and FLUKA for the dose averaged lineal energy in the CNAO test. Tolerances are 2% of the most probable energy for each point and 0.5 mm.

U3DTHIN detectors

The gamma test results for most probable lineal energy are shown in Figure 4.16 indicating the agreement of the experimental and Monte Carlo simulated data all along the Bragg curve, with gamma values of less than 0.65 for all points, and specially in the proximal Bragg peak area where the agreement is better, with gamma values less than 0.2.

If the same gamma test shown in figure 4.16 is performed to the dose-averaged values, the results of figure 4.17 are obtained.

The gamma values of the experimental results for $\bar{y}_D$ compared with FLUKA is better than 1.2 in the in the plateau region. In the proximal Bragg peak area the agreement is better with a descending trend in the gamma indices up to the Bragg peak. The differences observed with respect to the fluence-weighted values respond to the small shape variations of the microdosimetric distributions both from Monte Carlo and data. The presence of few counts for very large y values was also a source of uncertainty for the evaluation of $\bar{y}_D$.

The variability of the gamma values with respect to a change in the χ^2 parameters was also studied, showing a variation of the gamma values of up to 2 units in the plateau area and up to 1.5 units in the Bragg peak area for the fluence-averaged values with a change of the fit parameters within one standard deviation, assuming a Gaussian behaviour of the uncertainties.

3D Cylindrical microdosimeters

Figure 4.18 shows the result for the gamma test in most probable values of the CNAO beam, quantifying the excellent agreement between experimental data and simulations with this tolerances. Gamma index values are lower than 0.3 overall. In the proximal Bragg peak area, the differences between experimental points and simulations yield gamma index values less than 0.25.

The same gamma test as in figure 4.18 was performed for the dose-averaged values, presented in figure 4.19. The gamma test values take values below 1 in the proximal Bragg peak area and all values are less than 1.2. In this case there is a

higher fluctuation in the gamma values although a trend of lower values towards the Bragg peak can be observed. This can be caused due to some high-energy events in the distributions that alter the average value significantly.

A variation of the fit parameters within one standard deviation can change the gamma functions up to 2.5 units in some points in the plateau, although the gamma values are not significantly altered in the proximal Bragg peak area.

USC
UNIVERSIDADE
DE SANTIAGO
DE COMPOSTELA

Chapter 5

Future work and conclusions

Summary of the chapter:

This chapter presents the conclusions of this work along with some future improvements and possible experiments to be performed to improve the current technology of microstructured solid-state detectors for microdosimetry.

5.1 Conclusions

This thesis presents two different designs of microstructured silicon detectors for microdosimetric measurements. Performance and experimental validation of both kinds of silicon microsensors are covered in this work. The tasks performed were:

- **Study of the feasibility of the silicon based microstructured devices for microdosimetric applications.**

  In the case of the U3DTHIN silicon detectors, the tests in GANIL have shown the feasibility of the use of 3D diode silicon structures for the measurement of the microdosimetric distributions of ion beams. The possibility to perform actual measurements of these quantities allows a realistic analysis and commissioning of hadrontherapy beams. The silicon detectors tested were based in a novel production process that can yield thin diode three dimensional structures suitable for high fluence rate beams. The experimental setup included a PMMA motorized wedge that allowed the control of the effective thickness traversed by the beam with a precision of 40 μm in the case of the GANIL tests and 80 μm for the CNAO tests. The experimental results of the microdosimetric lineal energy spectra $y\ d(y)$ were compared to those obtained with FLUKA, obtaining excellent agreement for the most probable lineal energy value as a function of depth. For the evaluation of this agreement a gamma test [105] was performed with a variable tolerance for Δy equal to 10% of the most probable lineal energy for each point in the Bragg curve and a tolerance for $\Delta z = 0.5$ mm between FLUKA simulations and the experimental data. The experimental results have $\gamma < 0.65$. Considering the dose averaged lineal energy, the agreement between the silicon device data and the values computed from FLUKA is better than 1.2 in the gamma test. This results indicate that 3D ultra-thin silicon structures can be used to characterize the microdosimetric properties of ion beams. Nevertheless, U3DTHIN silicon detectors have some issues regarding the sensor response dynamical range and pile-up.

The other type of devices presented in the chapter were the silicon cylindrical microdosimeters. The test at the facilities of CNAO showed the good performance of the new silicon cylindrical microdosimeters for the measurement of microdosimetric distributions for hadrontherapy. The microdosimeters have a diameter of 15 μm and a thickness of 5.5 μm and an energy resolution of 12 % at an imparted energy of 650 keV. The detector is able to analyse LET or linear energy distributions of clinical beams, allowing the calculation of RBE and commissioning of said beams in clinical conditions, with a fluence rate of 5×10^7 s^{-1} cm^{-2} without saturation effects becoming apparent on the detector readout. Experimental spectra were compared with Monte Carlo simulation showing a great agreement between the most probable lineal energy, with gamma values between experimental points and Monte Carlo less than 0.25. This comparison was performed with the same gamma tolerances than the U3DTHIN detectors. Dose averaged lineal energy shows in general a good agreement, although pile-up and cross-talk events within the detector and CCE effects as described in this dissertation contribute to make this calculation less accurate than the most probable value discussed before. Gamma tests in this case takes values lower than 1.2 in general, with values lower than 0.3 in the proximity of the Bragg peak.

- **RBE calculation and uncertainty asessment.**

  RBE values through the use of the microdosimetric kinetic model (MKM) were also calculated from the transformation of imparted energy in silicon to saturation corrected dose-weighted specific energy, allowing the calculation of biological dose. These results indicate that the silicon cylindrical microdosimeters employed in this work can be used to characterize the microdosimetric and radiobiological properties of high LET beams as the ones used in hadrontherapy.

  The RBE values were also used to provide the tolerances to the gamma test done to the experimental measurements of both types of silicon detectors. By varying the input lineal energy used for the RBE calculation by a certain value the variation in the RBE was evaluated. It was estimated

that a relative uncertainty of the specific energy input parameters of $\sim 10\%$ provokes a RBE relative uncertainty of $\sim 6\%$.

- **From μ-randomness to clinical fluence**

  Historically different chord length distributions were used in the first formulation of microdosimetry such as μ-randomness derived from first principles in the so-called "geometrical probability". Actual chord length distributions in the practical proton and ion therapy clinical cases are significantly different from those general distributions.

  The probability distributions of the chord length inside the detector for a case of a beam of particles with almost parallel trajectories coming from a focal point outside the detector and with normal incidence were studied.

  It was found that the thickness of the detector can be used as the mean chord length of the particles due to the high directionality of the radiation field for the cases where the range of the particles was more than the thickness of the detector.

  A correction factor was calculated by Monte Carlo simulations to consider the divergence between the previous assumption and the real behaviour of the chord length distribution probabilities, although for the special case of protons those correction factors can be up to 10% in the Bragg peak, as shown in section 2.3.2.

- **Comissioning of Monte Carlo simulations.** The FLUKA Monte Carlo code developed for the simulation of the microdosimetric distributions measured with the silicon microstructured devices was benchmarked against experimental results performed with a PTW Peakfinder variable water column and a PTW 34080 Bragg-Peak chamber in a monoenergetic 115.2 MeV A^{-1} ^{12}C ion beam with a detailed simulation of the ionisation chamber in order to check its consistency.

  The local relative difference between experimental and simulation is less than 4% for all points along the Bragg curve, although the difference is higher in the distal tail. The results of this testing demonstrate that the

benchmark of the code was successful and can be safely used for hadrontherapy applications for protons and heavy ions.

- **Development and testing of discrete read out electronics for its use with silicon microdosimeters.** Throughout the course of this project the read out electronics were improved with the aim of getting portability, simple use, high signal to noise ratio, sensitivity and low noise levels. The last version of the readout electronics uses a tandem system of detector/pre-amplifying stage at approximately 5 cm the rest of the discrete electronic system that is housed outside the possible beam trajectory to avoid signal contamination by the event upset of the electronic components, followed by a fixed gain buffer amplifier, shaping stage, and baseline restorer. The electronics were optimized for the small input detector capacitance while providing AC readout of the detector to deal with its leakage current.

- **Assessment of the limitations of the detection system.**

  Although the microdetectors are capable of the measurement of microdosimetric distributions under clinical fluence rates, charge collection efficiency (CCE) and electronic noise pose limitations on their performance. For the cylindrical device studied in this work with 15 μm diameter and 5.5 μm thickness, the intrinsic field gradients and charge diffusion in the sensitive volume of the detector modify the recorded spectra by inducing a charge collection efficiency strongly dependent on the position of the energy deposition event. These perturbations modify the raw experimental microdosimetric spectra in a systematic way, producing an artificial enhancement of the low lineal energy region. In the present work this evidence was found in ^{12}C beam measurements at CNAO.

  In order to reproduce this systematic effect we constructed a first analytical model for the CCE by using exponential function and six parameters related to the physical dimensions of the microstructured detector. Electrical simulations using TCAD and proton beam IBIC tests performed to study the active volume inside the microdosimeters at different biasing voltages

were additionally used to validate the CCE model.

Monte Carlo simulations were modified by using this model to compute the partial charge collection in the simulated energy deposition events. Reconstructed spectra including CCE effect showed considerable agreement with the experimental results. The most probable lineal energy in these experimental spectra is shifted with respect to the expectation value from Monte Carlo. This shift along the Bragg curve holds a linear relationship with the lineal energy with a maximum of 16 keV/μm, about 6% of the most probable lineal energy at that point.

Additionally to the distortion of the low lineal energy spectra, the electronic noise contribution sets a theoretical limit on the smallest detectable lineal energy for microstructured solid state devices. Considering a cylindrical device with equal diameter and height L, the lineal energy threshold would be inversely proportional to this parameter. For example, for detecting events of 1 keV/μm, the dimension L should be greater than 4.4 μm whereas in diamond this size should be at least 16 μm.

5.2 Future work

There are several possible improvements to do in the solid-state microdosimetric detectors described in this work regarding their response and charge collection efficiency.

First, the structure of the microdosimeters could be improved to avoid as much as possible the modification of the microdosimetric spectra due to low charge collection efficiency in the periphery of the active volume of the detector.

This can be done by surrounding the current structure with new layers of detector material in a manner of a bullseye, adding further n and p doped regions in the periphery to enlarge the charge collection efficiency in the area. Currently this design is under development and this new version of the microdosimeter will be tested in the future.

The read-out electronics have been improved through the development of this

thesis. With the first designs of the read-out electronics a pre-assembled Amptek detector was employed, but a new design was made from scratch, employing CAEN first and then CREMAT modules in a customized printed circuit board that have better amplification than previous versions and an improved signal-to-noise ratio. These new versions can be further customised to take into account the energy deposition density of the measured radiation and provide a good full scale output.

The readout of multiple cells can also be improved. Currently, only one cell is read, and in order to provide spatial detection (one of the initial objectives thought for this device) the rest of the cells should also be evaluated. The cylindrical 3D microdosimeter array can be connected to a customised readout electronics system. One option under consideration is based on the use of a VATAGP7.1 chip [106]. This application-specific integrated circuit (ASIC) can provide a logic trigger signal and an analog output for 128 microsensors. Each of those channels features low noise, low-power buffered preamplifiers, a shaper with sample/hold, multiplexed analogue readout and calibration facilities. Moreover, each channel has a fast shaper that gives a trigger signal. The analogue value and the address of the triggering channels can be read out with a flexible serial or sparse readout mode. The VATAGP7.1 also offers input leakage current compensation automatically adjusted in each preamplifier channel. This ASIC can be chained to others VATAGP7.1 ASICs, sharing all output lines. This feature will allow to increase the number of channels and therefore the total area of the device.

Hence, the 3D microdetector array could be used as unit-cell for mimicking a cellular tissue-like piece (multiple arrays of that unit-cell) and to characterize the RBE in the hadrontherapy clinical centres. Further engineer and microfabrication developments could yield in a potential quality assurance (QA) system before patient treatment.

Finally, the 3D silicon cylindrical microdosimeters are going to be used in several research projects centred in novel hadrontherapy treatments capable of enhancing the quality of the current cancer treatments. With these new treatments new tools will be needed, either to spatially characterise a very small beam

(in the case of mini-beam radiation therapy) or to make a very fast read-out under very large dose rates (in the case of FLASH therapy). These new treatments pose new challenges in the fields of metrology.

The first of these projects is related with proton mini-beam radiation therapy (PMBRT). This technique combines small field sizes with a spatial fractionation of the dose, which increases the normal tissue resistance (and thus, more healthy tissue is spared from cell death due to ionising radiation) [107,108]. By employing sub-millimetre field sizes , with pencil beams with diameters of approximately 500-700 μm, the experiments on animals showed high resistance of the healthy tissue to very high doses of radiation, while achieving tumour control compared with a high dose irradiation through conventional means [109–113]. The spatial fractionation is made by means of a dose profile pattern consisting of peaks and valleys. The ratio between the maximum dose (at the peak) and the minimum (at the valley) is called peak-to-valley-dose-ratio (PVDR) and plays a very important role in the biological response [114]. The dose in the valleys should be kept to a minimum to preserve the normal tissue architecture and the survival of healthy cells for tissue repair.

The second research project where the microstructured silicon detectors are of interest is in FLASH radiotherapy. FLASH radiotherapy uses conventional X-ray, electron, and even proton beams to apply a very high dose in a very short time spam (dose rates $\geq$ 40 Gy/s). With this ultra-high dose rate the normal tissue complications are reduced while maintaining the tumour control level [115–118].

The tools and methods established for conventional radiotherapy cannot be used in FLASH therapy, as the ion collection efficiency of the air ionisation chambers employed in standard clinical practice is reduced up to 90% for the fluence rates used in FLASH therapy. By using the technology described in this thesis, the aim of the USC (and CNM-CSIC) will be to develop a prototype active dosimeter based on microstructured silicon technology and the characterisation of detectors in proton and electron FLASH beams.

USC
UNIVERSIDADE
DE SANTIAGO
DE COMPOSTELA

Appendix A

Proton test at CNAO ion beam

In this appendix an additional test of the 3D cylindrical microdosimeters with 66.34 MeV proton beam will be presented. The tests were done at the cyclotron of Fondazione CNAO (Pavia, Italy). As in the ^{12}C ion test, the results were compared with Monte Carlo simulations using the FLUKA Monte Carlo code.

The materials and methods employed are the same as in chapter 4.

A.1 Results and discussion

As in chapter 4, the data obtained was analysed and compared with Monte Carlo simulations made with FLUKA. The proton beam was propagated in a variable thickness of PMMA and then in a detailed geometry of the detector system, reconstructing a Bragg curve. The dimensions of the detector are the same as the ^{12}C ion test at CNAO, and were not compared with other measurements of the same beam with different detection systems (e.g. TEPCs).

As in the ^{12}C ion tests, the imparted energy ε is considered proportional to the silicon detector signal while the mean chord length $\bar{l}$ is approximately equal to the detector thickness for frontal irradiation. This was further confirmed by evaluating the particle track length on the Monte Carlo simulations up to the Bragg Peak, resulting in values equal to the active area thickness with an error

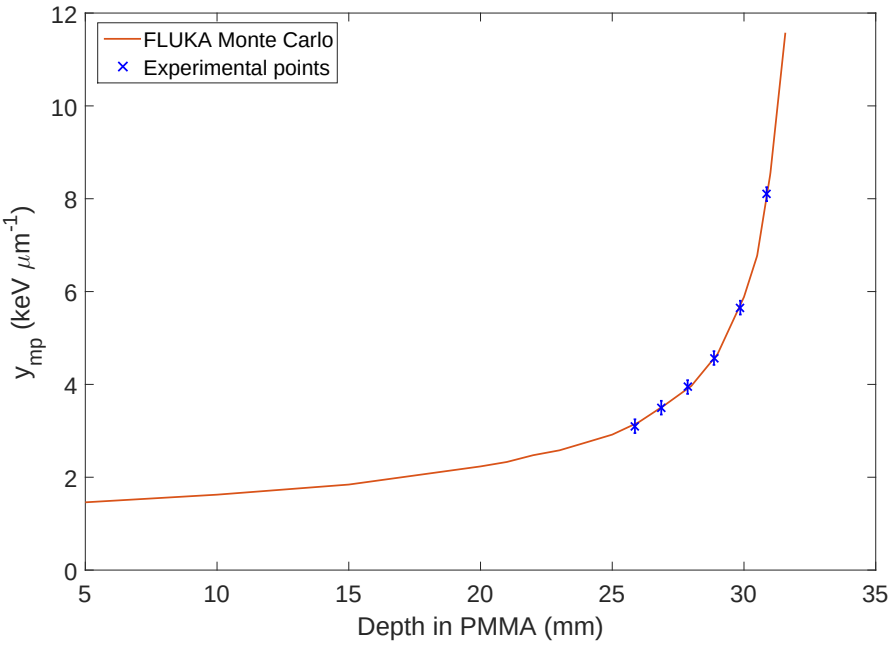

Figure A.1: Comparison of the most probable lineal energy experimental (crosses) and FLUKA Monte Carlo (solid line) values in the silicon detector for the 3D cylindrical microdosimeters in the CNAO proton test.

estimate of less than 1%.

The three parameter minimisation of a χ^2 type function shown in equation 4.1 was also employed here to obtain the ADC to lineal energy conversion parameters. The results in this case show an excellent agreement for N=(0.0137±0.0046) keV μm^{-1} adc^{-1} with Δ= (0.323±0.087) keV μm^{-1} and ζ=(1.750±0.069) mm, shown in figure A.1 between data and FLUKA.

The small number of experimental points shown here is due to the fact that there was a very high amount of noise stemming from the irradiation of the components of the detection system by the beam that could not be avoided at the time of the experiment. This provoked a high number of counts in the low-energy part of the spectrum. Since the detection system for protons was way

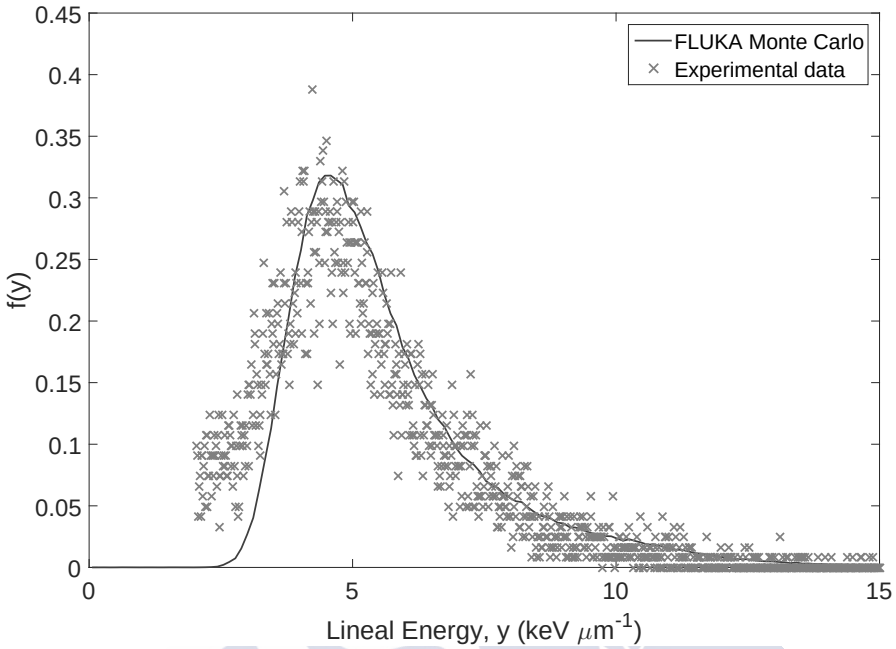

Figure A.2: Probability distributions f(y) in silicon from experimental data and FLUKA at a depth of 29 mm PMMA for the 3D cylindrical microdosimeter in the CNAO proton test. The black solid line represents the FLUKA Monte Carlo spectra, whereas the grey crosses show the experimental data.

more sensitive than the carbon one, the measurement of the points in the plateau of this particular Bragg curve (around 2-5 keV/μm) were not possible with that noise level.

A frecuency distribution, $f(y)$, for a depth of 29 mm PMMA is also shown in A.2. In this figure, there is a very good agreement between the measured and simulated spectra, although the usual difference in the shape of the distributions due to partial charge collection is also present here.

Finally, to evaluate the agreement between experimental points and Monte Carlo simulations a Gamma test [105] was employed. The tolerances chosen were the same as the ones selected in section 4.2.3, 0.5 mm in thickness and a 2% of the Monte Carlo lineal energy value at each point. The gamma test for most

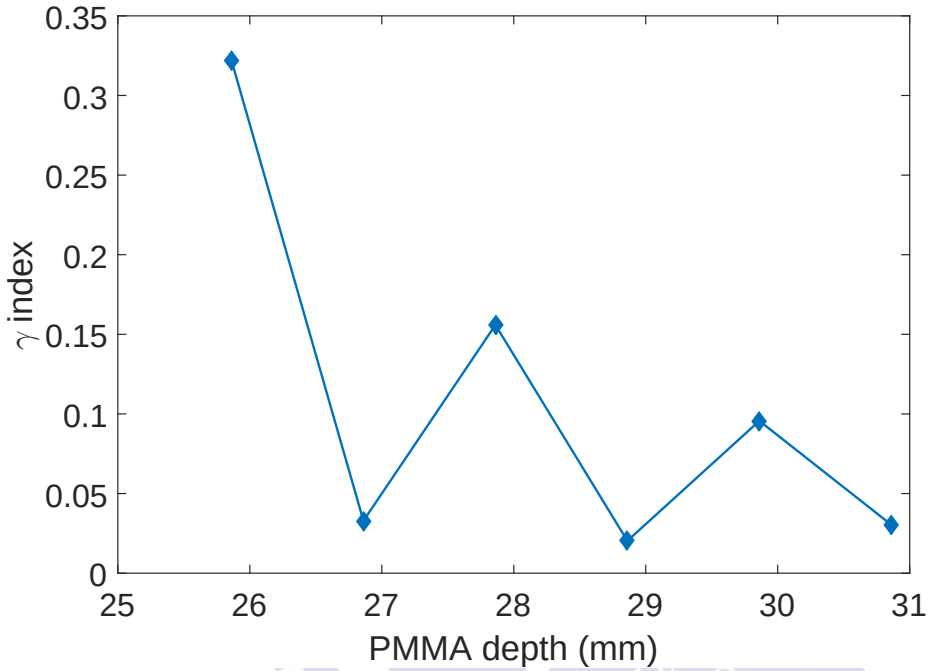

Figure A.3: Gamma function for the most probable lineal energy obtained from the proton experiment at CNAO and FLUKA Monte Carlo. Tolerances are 2% of the most probable energy for each point and 0.5 mm.

probable energy in this proton test is shown in figure A.3.

In the gamma test of figure A.3 it is shown a very good agreement between the experimental points and the simulations, with values less than 0.35 for all points and values less than 0.2 in all points except one. Additionaly, a variability study of the gamma values when a change in the minimisation parameters are change was also performed, showing variations of the gamma values in up to one unit at the beginning of the knee, with the values going down to 0.4 in the proximal Bragg area.

A.2 Conclusion

Although the results show a remarkable agreement between the experimental spectra and the Monte Carlo simulated ones, the geometry of the detection system proved to be not very useful for these types of experiment due to the accidental irradiation of some vital components that made impossible to evaluate most of the points in the Bragg curve. This experiment was very important to discover this important issue and since then the experimental device has been improved, protecting the most vital components and shielding them from the beam.

USC
UNIVERSIDADE
DE SANTIAGO
DE COMPOSTELA

Appendix B

FLUKA Monte Carlo code for boundary crossing particle tracking

The FLUKA code for calculating the necessary quantities employed in section 3.4 will be reproduced here. The code is written in FORTRAN77, the native language in which FLUKA Monte Carlo code is written.

```
*$ CREATE MGDRAW.FOR
*COPY MGDRAW
*                                                                     *
*=== mgdraw ===========================================================*
*                                                                     *
      SUBROUTINE MGDRAW ( ICODE, MREG )

      INCLUDE '(DBLPRC)'
      INCLUDE '(DIMPAR)'
      INCLUDE '(IOUNIT)'
*
```

```
*=====================================================================*
*                                                                     *
*     Routine based on MGDRAW by Alfredo Ferrari                      *
*                                                                     *
*     Created on   15 March 2019   by       Juan Prieto-Pena          *
*                                           USC-Santiago de Compostela *
*                                                                     *
*=====================================================================*
*
      INCLUDE '(CASLIM)'
      INCLUDE '(COMPUT)'
      INCLUDE '(SOURCM)'
      INCLUDE '(FHEAVY)'
      INCLUDE '(FLKSTK)'
      INCLUDE '(GENSTK)'
      INCLUDE '(MGDDCM)'
      INCLUDE '(PAPROP)'
      INCLUDE '(QUEMGD)'
      INCLUDE '(SUMCOU)'
      INCLUDE '(TRACKR)'
*
      LOGICAL PRTF
      INTEGER IONA, IONZ, IONM
      DOUBLE PRECISION EDEP, TRKL
*
*=====================================================================*
*                                                                     *
*     Icode = 1: call from Kaskad                                     *
*     Icode = 2: call from Emfsco                                     *
*     Icode = 3: call from Kasneu                                     *
*     Icode = 4: call from Kashea                                     *
*     Icode = 5: call from Kasoph                                     *
*                                                                     *
```

```
*--------------------------------------------------------------------*

      IF ( (MREG .GE. 21).AND.(MREG .LE. 142) ) THEN

               IONA = 0
               IONZ = 0
               IONM = 0

               CALL USRDCI( JTRACK, IONA, IONZ, IONM)

               do 40 I=1, MTRACK
                   EDEP=EDEP+DTRACK(I)
40             continue
               do 50 I=1, NTRACK
                TRKL=TRKL+
     &          SQRT( (XTRACK(I)-XTRACK(I-1))**2 +
     &          (YTRACK(I)-YTRACK(I-1))**2 + (ZTRACK(I)-ZTRACK(I-1))**2)
50     continue
               PRTF=.TRUE.

      END IF

      RETURN
*
*====================================================================*
*                                                                    *
*     Boundary-(X)crossing DRAWing:                                  *
*                                                                    *
*     Icode = 1x: call from Kaskad                                   *
*             19: boundary crossing                                  *
*     Icode = 2x: call from Emfsco                                   *
*             29: boundary crossing                                  *
*     Icode = 3x: call from Kasneu                                   *
```

```
*             39: boundary crossing                                    *
*     Icode = 4x: call from Kashea                                     *
*             49: boundary crossing                                    *
*     Icode = 5x: call from Kasoph                                     *
*             59: boundary crossing                                    *
*                                                                      *
*======================================================================*
*                                                                      *
      ENTRY BXDRAW ( ICODE, MREG, NEWREG, XSCO, YSCO, ZSCO )

      CALL USRDCI( JTRACK, IONA, IONZ, IONM)

      IF((NEWREG .GE. 21).AND.(NEWREG .LE. 142)) THEN
         IF(ETRACK.GT.AM(JTRACK)) THEN
              WRITE(41, * ) '---'
              WRITE(41,'(
     &        A3,4X,I2,14X,I2,11X,D17.7,/,
     &        A3,1X,D17.7,1X,D17.7,1X,D17.7,/,
     &        A3,1X,D17.7,1X,D17.7,1X,D17.7)')
     &        'PRT',IONA,IONZ,ETRACK-AM(JTRACK),
     &        'POS',XSCO,YSCO,ZSCO,
     &        'COS',CXTRCK,CYRCK,CZTRCK
              ENDIF
      ENDIF

      RETURN
*
*======================================================================*
*                                                                      *
*     Event End DRAWing:                                               *
*                                                                      *
*======================================================================*
*                                                                      *
```

```
      ENTRY EEDRAW ( ICODE )
      IF(PRTF .EQV. .TRUE.) THEN
         PRTF=.FALSE.
         IF((ETRACK.GT.AM(JTRACK))) THEN
            IF((EDEP.GT.1.0E-9)) THEN
               WRITE(41,'(A3,1X,D17.7,/,A3,1X,D17.7)')
     &              'EDP', EDEP,
     &              'TRK', TRKL
            END IF
*            ELSE
*               WRITE(41,'(A3,5X,A3)')
*     &              'EDP', '0.0'
         END IF
      END IF
      EDEP=0
      TRKL=0
      RETURN
*
*=======================================================================*
*                                                                       *
*     ENergy deposition DRAWing:                                        *
*                                                                       *
*     Icode = 1x: call from Kaskad                                      *
*             10: elastic interaction recoil                            *
*             11: inelastic interaction recoil                          *
*             12: stopping particle                                     *
*             13: pseudo-neutron deposition                             *
*             14: escape                                                *
*             15: time kill                                             *
*     Icode = 2x: call from Emfsco                                      *
*             20: local energy deposition (i.e. photoelectric)          *
*             21: below threshold, iarg=1                               *
*             22: below threshold, iarg=2                               *
```

```
*             23: escape                                               *
*             24: time kill                                            *
*     Icode = 3x: call from Kasneu                                     *
*             30: target recoil                                        *
*             31: below threshold                                      *
*             32: escape                                               *
*             33: time kill                                            *
*     Icode = 4x: call from Kashea                                     *
*             40: escape                                               *
*             41: time kill                                            *
*             42: delta ray stack overflow                             *
*     Icode = 5x: call from Kasoph                                     *
*             50: optical photon absorption                            *
*             51: escape                                               *
*             52: time kill                                            *
*                                                                      *
*======================================================================*
*                                                                      *
      ENTRY ENDRAW ( ICODE, MREG, RULL, XSCO, YSCO, ZSCO )
      IF ( (MREG .GE. 21).AND.(MREG .LE. 142) ) THEN
          EDEP=EDEP+RULL
          PRTF=.TRUE.
      END IF
      RETURN
*
*======================================================================*
*                                                                      *
*     SOurce particle DRAWing:                                         *
*                                                                      *
*======================================================================*
*
      ENTRY SODRAW
      RETURN
```

```
*
*=====================================================================*
*                                                                     *
*     USer dependent DRAWing:                                         *
*                                                                     *
*     Icode = 10x: call from Kaskad                                   *
*             100: elastic   interaction secondaries                  *
*             101: inelastic interaction secondaries                  *
*             102: particle decay  secondaries                        *
*             103: delta ray  generation secondaries                  *
*             104: pair production secondaries                        *
*             105: bremsstrahlung  secondaries                        *
*             110: radioactive decay products                         *
*     Icode = 20x: call from Emfsco                                   *
*             208: bremsstrahlung secondaries                         *
*             210: Moller secondaries                                 *
*             212: Bhabha secondaries                                 *
*             214: in-flight annihilation secondaries                 *
*             215: annihilation at rest   secondaries                 *
*             217: pair production        secondaries                 *
*             219: Compton scattering     secondaries                 *
*             221: photoelectric          secondaries                 *
*             225: Rayleigh scattering    secondaries                 *
*             237: mu pair     production secondaries                 *
*     Icode = 30x: call from Kasneu                                   *
*             300: interaction secondaries                            *
*     Icode = 40x: call from Kashea                                   *
*             400: delta ray  generation secondaries                  *
*  For all interactions secondaries are put on GENSTK common (kp=1,np) *
*  but for KASHEA delta ray generation where only the secondary elec-  *
*  tron is present and stacked on FLKSTK common for kp=npflka         *
*                                                                     *
*=====================================================================*
```

```
*
      ENTRY USDRAW ( ICODE, MREG, XSCO, YSCO, ZSCO )
      RETURN
*
*=== End of subrutine Mgdraw ==========================================*
      END
```

Resumen en castellano

Nota: Para la realización de esta tesis doctoral se ha recibido financiación del antiguo Ministerio de Economía y Competitividad (MINECO) a través de un proyecto RETOS MINECO DPI2014-57645-R. También se ha recibido financiación de la Fundación Barrié mediante una beca de estancia predoctoral realizada en Turín (Italia) entre los meses de septiembre y diciembre de 2016.

El término conocido como "cáncer" es en realidad un término muy genérico que designa a un gran número de enfermedades diferentes y relacionadas entre sí caracterizadas por ciertos rasgos comunes [1, 2]: Autoestimulación del crecimiento, insensibilidad a las señales inhibidoras del crecimiento, evasión de la apoptosis, potencial ilimitado de replicación, angiogénesis continuada en el tiempo, invasión de tejidos vecinos y metástasis, reprogramación del metabolismo energético del cuerpo y mecanismos para evitar la respuesta inmune del cuerpo en el que se encuentran.

La IARC (siglas en inglés de la Agencia Internacional para la Investigación del Cáncer, dependiente de la Organización Mundial de la Salud de las Naciones Unidas) en su informe sobre el cáncer 2014 [3] estima que el esta enfermedad es una de las mayores causas de mortalidad a nivel mundial, con casi 14 millones de casos registrados y 8 millones de muertes directamente atribuíbles sólo en el año 2012.

Se estima que en los países desarrollados, el número proyectado de casos se incrementará entre un 20 y un 60% en el año 2030 [4], dependiendo del tipo de cáancer estudiado. Esto se debe principalmente al constante incremento de la

esperanza de vida y el incremento de la calidad en el tratamiento sanitario.

Tradicionalmente se ha venido tratando el cáncer de tres maneras diferentes, generalmente combinándose entre ellas. Estas modalidades tradicionales de lucha contra el cáncer son tres: Cirugía, quimioterapia y radioterapia (RT). Actualmente se están desarrollando nuevos tratamientos, como la hormonoterapia o la inmunoterapia. El método escogido por el especialista depende del tamaño y localización del área tumoral, el estadio del cáncer u otros factores.

El tipo de tratamiento más común a día de hoy, ya sea como tratamiento principal o coadyuvante, es la radioterapia. Se estima que alrededor de la mitad de todos los tratamientos contra el cáncer usan algún tipo de radioterapia [5, 6]. Este tipo de tratamiento ha demostrado ser una herramienta muy efectiva y eficiente para lograr el control tumoral [7].

En los tratamientos de radioterapia se trata de suministrar una cierta cantidad de radiación para que se deposite en el volumen tumoral con exactitud y precisión, evitando todo el daño posible al tejido sano.

Para realizar esta tarea se emplean los dosímetros, que son los aparatos que miden la cantidad de radiación proporcionada por una fuente externa y que permiten cerciorarse de que la dosis que llega a la zona tumoral sea igual a la prescrita. El mecanismo de función de los distintos tipos de dosímetro es muy variado, dependiendo en el efecto físico o químico que la radiación ionizante provoca sobre ellos. Conociendo los procesos que la radiación produce sobre un determinado tipo de dosímetro se puede cuantificar el efecto de la radiación y, por tanto, la dosis que ha recibido el dosímetro y extrapolarla a la dosis que recibe el paciente. Para realizar esta extrapolación existen programas de control de calidad que describen como medir la dosis correctamente [8, 9].

Debido a que el tejido tumoral es generalmente menos radiorresistente que el tejido sano, mediante la radioterapia se puede dañar más el volumen tumoral, mientras que los tejidos de alrededor no son afectados signficativamente. La radiación ionizante no puede discriminar entre tejido sano y tumoral, excepto en algunas modalidades exóticas de radioterapia, como la terapia por captura de neutrones (BNCT, por sus siglas en inglés), en los que se aplica un fármaco

que se adhiere al tumor y que incluye ^{10}B antes de la irradiación por neutrones. Debido a que el ^{10}B tiene una sección eficaz de captura de neutrones muy alta, la radiación interactúa más con el tejido afectado por el fármaco.

En los tratamientos de radioterapia es necesario evitar daño innecesario al paciente que pueda afectar a su calidad de vida. Hay diferentes maneras de conseguirlo dependiendo de las particularidades de la enfermedad. Como se ha dicho antes, el cáncer es un término muy extenso y el tumor puede ser de distintos tipos (diferentes líneas celulares, tumores líquidos o sólidos, un área tumoral bien definida o no, etc.). La dosis de radiación puede ser suministrada de manera externa (mediante aceleradores lineales) o internamente (braquiterapia). Las partículas empleadas pueden ser también de diferentes tipos (electrones, fotones, neutrones, protones o incluso iones de núcleos atómicos). En esta tesis nos centraremos en los efectos de protones y núcleos atómicos en tejidos tumorales. Esta modalidad de radioterapia se denomina terapia de partículas (PT, en sus siglas en inglés) o hadronterapia.

La radioterapia externa, por su propia naturaleza, siempre dañará el tejido sano colindante al tumor, debido a que suministra la dosis sobre su trayectoria de propagación sin discriminar entre tejido sano o tumoral, pero estos efectos se pueden mitigar gracias a diferentes desarrollos tecnológicos basados en tecnologías de imagen médica. También se emplea el fraccionamiento del tratamiento en varias sesiones con menor dosis para ayudar al tejido sano a recuperarse y poder afectar al tejido tumoral en diferentes etapas de su ciclo celular.

Otra posible manera de evitar daños al tejido sano es mediante la superposición de varios haces entrando desde diferentes partes del cuerpo del paciente, haciéndoles converger en la región de interés, depositando la dosis prescrita en el volumen tumoral. La forma del haz puede ajustarse para hacerla coincidir con la forma de la sección del volumen tumoral, ayudando aún más a minimizar el daño al tejido sano. Esta técnica se conoce como ''conformación de haz".

La forma más común de radioterapia emplea fotones para irradiar el tejido tumoral. Hoy en día esta modalidad de radioterapia está muy avanzada [7] gracias al uso de técnicas de radioterapia guiada por imagen (IGRT), como la radioter-

apia de intensidad modulada (IMRT) o la radioterapia esterotáctica de cuerpo completo (SBRT), permitiendo una confomación de dosis al tejido tumoral muy alta. Combinando estas técnicas con la de hipo-fraccionamiento en algunos tipos espcíficos de tumores, el tiempo de tratamiento puede ser reducido en gran medida, llegando incluso a depositar la dosis prescrita en una única sesión, permitiendo a las técnicas de radioterapia competir directamente con la cirugía en algunos casos.

Debido a la naturaleza de la interacción radiación-materia, especialmente el decaimiento exponencial de la intensidad en función de la profundidad en el caso de los rayos X, se hace necesario irradiar el tejido sano que rodea al área tumoral, incrementando la probabilidad de complicaciones en el paciente. Robert Wilson propuso una manera diferente de abordar este problema. En su artículo seminal de 1946 [10] Wilson propuso el uso de iones en radioterapia, especialmente núcleos atómicos, postulando diferentes ventajas de este tipo de particulas frente a los tratamientos más tradicionales, dando nacimiento al campo de la terapia de partículas.

La justificación se basa en que el núcleo atómico provoca un mayor daño tanto a niveles celulares como sub-celulares que los tratamientos con fotones y electrones y una mayor conformación de la dosis. Usando nucleones se pueden obtener ventajas adicionales debido a la mayor deposición de energía por unidad de longitud (Transferencia lineal de energía, o LET) y el diferente comportamiento de las células a diferentes tipos de radiación. Usando protones o núcleos atómicos el tejido sano se irradia con radiación de bajo LET, de manera más o menos similar a los rayos X, mientras que el volumen tumoral se irradia con radiación de alto LET. Las partículas cargadas atraviesan el medio en una línea recta, y el alcance de estas partículas es altamente dependiente en la energía cinética inicial y el potencial de ionización medio del medio. Las partículas cargadas depositan la mayor parte de su energía en el final de su trayectoria, y una mínima cantidad de energía a la entrada del cuerpo. Usando una mezcla de energías, el volumen tumoral puede ser cubierto por completo. La figura 1.1 muestra los perfiles de dosis en función de la profundiad de fotones, protones e iones de carbono.

El número de instalaciones de terapia de partículas ha crecido de manera

gradual a lo largo de la pasada década [12]. En el caso de Europa, la terapia de partículas comenzó a usarse en Uppsala, Suecia, en el año 1953. De acuerdo con la organización científica PTCOG [13] hay actualmente 80 centros en operación a fecha de enero de 2019 y 67 centros en fase de planificación o construcción. En el caso de España hay dos hospitales privados construyendo centros de protonterapia en Madrid, con fechas planeadas de apertura en 2019 y 2020.

No existe una evidencia significativa a favor del uso de protones u otro tipo de partículas más pesadas en el tratamiento de tumores [14], aunque existen pruebas de que para algunos tipos de tumores el uso de terapia de partículas resulta en un menor número de complicaciones secundarias [15]. Esto significa que se necesita más investigación, tanto básica como aplicada, en este campo para estimar la validez de estas nuevas técnicas y su efectividad contra el cáncer.

Para estudiar los procesos biológicos que resultan de la deposición de energía mediante radiación ionizante en áreas de tamaño micrométrico o sub-micrométrico (esto es, a nivel celular y sub-celular) se ha creado una nueva disciplina relacionada con la dosimetría llamada microdosimetría [16, 17], debido a la naturaleza estocástica de la interacción entre radiación y materia a esas escalas. A partir del comportamiento microdosimétrico de la radiación y del modo en el que depositan energía a esas escalas se pueden establecer factores pesados de radiación. Las distribuciones de energía lineal se pueden yuxtaponer a modelos computacionales por método de Monte Carlo para caracterizar los haces de radiación [18, 19].

Los contenidos de esta tesis doctoral son los resultados de la investigación en el campo de la microdosimetría y el desarrollo de detectores de silicio para hadronterapia realizados en el Grupo de Imagen Molecular y Física Médica perteneciente a la universidad de Santiago de Compostela entre los años 2014 y 2019. Durante este tiempo se realizó una estancia de tres meses (septiembre-diciembre 2016) en la Universidad de Turín con el objetivo de desarrollar diferentes experimentos de microdosimetría en los haces clínicos de protones e iones de carbono de la Fundación CNAO (Pavía, Italia) para comprobar el funcionamiento de los detectores de silicio 3D fabricados por el Instituto de Microelectrónica de Barcelona (Instituto Nacional de Microelectrónica-CSIC) en colaboración con nuestro grupo.

Esta tesis se divide en cuatro capítulos bien diferenciados, que serán resumidos a continuación:

El primer capítulo consta de una introducción en inglés al resto de la tesis, siendo muy parecido a la primera parte de este resumen.

A continuación, el segundo capítulo consta de una breve introducción teórica que describe los términos empleados en este trabajo y la teoría bajo la que se sostienen el resto de capítulos, con explicaciones sobre interacción entre radiación y materia, tanto con partículas cargadas como con partículas neutras, la física de la radiación con la descripción de las diferentes magnitudes dosimétricas que se emplearán en este trabajo, una breve introducción a la microdosimetría y sus magnitudes, añadiendo también una breve discusión sobre el concepto de la longitud de cuerda, una magnitud estocástica relacionada con la longitud de las trazas que realiza una partícula sobre un volumen determinado.

Tradicionalmente, la dosimetría se encarga del estudio de deposición de energía mediante radiación ionizante a volúmenes grandes (a nivel tisular). La cantidad empleada para describir la cantidad de radiación absorbida por un volumen se llama dosis absorbida y se define en términos de energía absorbida por unidad de masa que recibe la radiación (en J/Kg, en unidades del S.I.) [21].

Sin embargo, la dosis por sí sola no es suficiente para determinar el efecto biológico de un tipo de radiación. Las modificaciones que la radiación realiza sobre medios biológicos dependen también de las propias condiciones físicas de la irradiación y de otros parámetros químicos y biológicos, como la calidad de haz y la distribución temporal de deposición de energía. La calidad de haz se define como aquellas características de la distribución espacial de transferencias de energía que influyen en la efectividad de la irradiación de producir un cambio discernible en el volumen cuando otros factores físicos como energía total disipada, dosis absorbida, tasa de dosis absorbida o fraccionamiento de la dosis total se mantienen constantes [40].

La calidad de haz se describe generalmente mediante la transferencia lineal de energía o LET [21]. Esta cantidad describe la densidad de deposición de energía en el medio debida a las partículas incidentes. El LET de un material para

partículas cargadas de un tipo y energía determinados se define como el cociente entre la energía media perdida por partículas cargadas debido a interacciones electrónicas en el medio y el camino recorrido por la traza en el material. Existe un modo de restringir el LET mediante la discriminación de partículas con un alcance superior a un alcance umbral (LET restringido). Si no hay restricción el LET se denota con la letra L mayúscula, se denomina LET sin restringir y es igual al poder de frenado electrónico, S_{el}.

Existen algunas limitaciones en el análisis dosimétrico de los haces de radiación usando el LET. El LET no es suficiente para caracterizar dosimétricamente un haz de radiación y especificar su eficiencia radiobiológica (que describiremos más adelante). El LET es sólo un valor promedio de la pérdida de energía de una partícula a lo largo de su traza [41, 42]. Las limitaciones del LET fueron el punto de partida del campo de la microdosimetría por Rossi y Kellerer en la década de los 70. Esto no significa que la noción del LET deba ser descartada por completo. En algunos casos es necesaria una evaluación aproximada de la calidad de radiación para comparar diferentes calidades de haz y el análisis de las distribuciones de LET puede encargarse de ello.

En dosimetría, tradicionalmente se ha empleado el agua como material de referencia equivalente a tejido y las magnitudes empleadas suelen referirse a este material para permitir una mejor intercomparación de resultados. Es posible obtener factores de conversión de equivalencia a agua a partir de tablas de alcance-energía o el ratio de poderes de frenado. Sin embargo, si un material es muy diferente en número atómico efectivo al del agua esta conversión se vuelve más complicada. En el caso de energías y materiales empleados tradicionalmente en microdosimetría existen multitud de referencias en la literatura que permitirían convertir espectros microdosimétricos a espectros microdosimétricos en agua.

En el caso del silicio, debido a la diferencia de poderes de frenado entre éste material y el agua el proceso de conversión se torna más complicado, especialmente a bajas energías. Actualmente existen procesos usando diferentes factores de conversión que permiten realizar esta tarea con precisión [45, 46].

¿Qué pasaría si el volumen de estudio fuese tan pequeño (del tamaño de

una célula, o una molécula) que las fluctuaciones estadísticas de la energía impartida media fuesen demasiado importantes como para poder realizar un análisis dosimétrico? Aunque la energía impartida media es un buen indicador de la deposición de energía sobre un volumen la distribución microscópica de deposición de energía es muy importante para evaluar el daño biológico producido por radiación ionizante. Los efectos de la radiación dependen de la distribución espacial de la deposición de energía en el medio. La microdosimetría considera las fluctuaciones estadísticas de las cantidades dosimétricas debido a la naturaleza estocástica de la interacción entre radiación y materia. La materia y la radiación (átomos y cuantos, respectivamente) pueden describirse como estructuras discretas que pueden causar fluctuaciones, a nivel individual, en procesos físicos. Normalmente, los valores anómalos muy alejados de la media pueden ignorarse debido a que no son significativos, pero en el caso de la radiación, donde un solo cuanto puede provocar la muerte del volumen de estudio las fluctuaciones estadísticas son una parte muy importante que debe ser considerada en el estudio. La microdosimetría usa la aproximación de que todas las cantidades dosimétricas siguen una cierta distribución de probabilidad [17].

Existen ciertos equivalentes microdosimétricos de cantidades empleadas en dosimetría. Por ejemplo, el equivalente microdosimétrico de la dosis se denomina energía específica y se denota con la letra z. La energía específica se describe de la misma manera que la dosis absorbida, esto es, energía impartida por unidad de masa. En el límite de volúmenes grandes, la energía específica, z, tiende al valor medio de dosis absorbida, $\bar{D}$. Por otro lado, el análogo microdosimétrico del LET se denomina energía lineal y se define como la energía depositada por un único evento dividida por la longitud de traza media recorrida por las partículas dentro del volumen.

Los momentos de las distribuciones de probabilidad de energía específica y energía lineal pueden ser calculados a partir de las distribuciones de probabilidad de energía impartida o energía lineal. El primer momento de las distribuciones se denominan promedios pesados en fluencia. El cociente entre el segundo y el primer momento de las distribuciones microdosimétricas de probablidad se denominan promedios pesados en dosis.

Anteriormente mencionábamos que el equivalente microdosimétrico del LET es igual a la energía impartida en un solo evento dividida entre la longitud de traza media. La longitud de traza es otra distribución microdosimétrica que describe la longitud del recorrido de las partículas dentro del volumen de interés. En el caso de cuerpos convexos la longitud de traza media puede ser de varios tipos distintos [47], siendo la más importante para el caso que nos ocupa la aleatoriedad de camino libre medio, o μ-randomness.

En este caso la traza de un cuerpo convexo K se define por la intersección de este cuerpo con una línea recta definida por un punto en el espacio euclídeo y una dirección, con el punto y la dirección obtenidos a partir de distribuciones uniformes de probabilidad independientes. Este tipo de aleatoriedad se da cuando el cuerpo convexo está expuesto a un campo uniforme de radiación formado por infinitas trazas rectilíneas. Mediante la convolución de la distribución de energía impartida en el volumen y la distribución de longitud de trazas, es posible obtener una distribución de LET (o, en el caso en el que tomemos el valor medio de la longitud de traza, la energía lineal) [43].

Aunque, en el caso que nos ocupa (muy alejado de la condición de μ-randomness), es posible suponer que debido al poco grosor del detector estudiado en este trabajo y a la incidencia normal sobre éste se pueda tomar la longitud de traza media como el valor del grosor, aplicando adicionalmente factores de corrección de ser necesario. Estos factores de corrección son aproximadamente iguales a la unidad en toda la curva de Bragg. Esto se ha comprobado mediante el estudio de las longitudes de trazas de protones de 50 MeV en un volumen cilíndrico de agua definido por un parámetro L igual al diámetro y la altura del cilindro. En el caso del estudio, $L = 20$ μm. También se ha estudiado la dependencia angular de la distribución de longitud de traza en condiciones de irradiaciones diferentes a la irradiación normal.

El estudio de las distribuciones microdosimétricas es necesario para el cálculo de variables radiobiológicas como el RBE, o eficiencia biológica relativa. El RBE permite comparar la efectividad de un cierto tipo de radiación frente a una calidad estándar, como ^{60}Co o rayos X de 250 keV [48]. Se calcula como el cociente entre la cantidad de dosis necesaria para provocar un efecto dado en la calidad de

radiación a estudiar y la calidad de radiación estándar. El RBE es una cantidad muy compleja que no sólo depende de las características físicas de la radiación empleada, sino también de características biológicas del objeto irradiado tales como el tipo de célula irradiada, la concentración de oxígeno en el tejido o la etapa celular [12].

Para el cálculo de las distribuciones de LET/Energía lineal se han venido usando tradicionalmente cámaras proporcionales equivalentes a tejido (TEPC). Estos detectores funcionan midiendo la ionización en un volumen macroscópico de gas que simula un sitio microscópico mediante la variación de la densidad del gas dentro de la cámara. La mayor desventaja de este tipo de detectores es que las paredes provocan distorsiones en la medida debido a la dispersión de partículas atravesando ese muro debido a la diferencia de densidades entre pared y gas en el interior, alterando el equilibro de partículas cargadas y modificando los espectros microdosimétircos. Las TEPC, debido a su gran tamaño, también tienen una baja resolución espacial y no pueden operar en condiciones de alta tasa de fluencia. Recientemente ha habido mejoras en este sentido, con la miniaturización de este tipo de detectores (miniTEPC) y su capacidad para trabajar en entornos con alta tasa de fluencia.

Otra posible manera de medir las distribuciones microdosimétricas, y la razón principal de esta tesis, es mediante el uso de detectores de estado sólido. Los detectores de estádo sólido ofrecen particularidades muy favorables a la hora de su uso como detectores. No sólo tienen una alta resolución en energía y un tamaño reducido, pero también son más fáciles de usar que las TEPC (no necesitan fuentes de alto voltaje) y su respuesta es más rápida. Las principales desventajas son que debido a lo complicado de su proceso de fabricación no pueden obtenerse detectores de gran tamaño y que el material es altamente susceptible al daño por radiación.

Para terminar el capítulo se describe el principal código Monte Carlo que se ha empleado en el transcurso de esta tesis para comparar los resultados experimentales con los modelos teóricos. Dicho código ha sido FLUKA, un código multipropósito de historia condensada desarrollado por el CERN en colaboración con el INFN (Italia) basado en FORTRAN77. Se usa para el cálculo de trans-

porte de partículas e interacciones con la materia y es empleado en gran cantidad de campos diferentes, incluyendo el de la física médica.

El siguiente capítulo de la tesis describe los microdosímetros de silicio empleados en la tesis. Tradicionalmente se ha empleado una geometría planar en los detectores de silicio, aunque este tipo de geometría provocaba que en condiciones de alta tasa de fluencia de partículas los pares electrón-hueco creados inducían un crecimiento de espacio negativo de carga en las regiones de vaciado del detector. Esto hacía necesario el uso de voltajes elevados para poder superar ese efecto, generando una corriente de fuga elevada que reducía la relación señal-ruído. A todo esto se añade el elevado tiempo de colección de carga.

Sin embargo, Parker y Kenney propusieron el uso de una arquitectura tridimensional para evitar esos efectos con el objeto de usar detectores de silicio en aplicaciones de física de altas energías e imagen médica [83]. En la configuración de Parker y Kenney el detector consiste de una matriz tridimensional de electrodos penetrando en el seno del silicio, siendo los conductores de carga colectados por electrodos cilíndricos de signo opuesto. Las distancias de deriva y los tiempos de colección se verían reducidos debido a esta configuración. Asimismo, el voltaje necesario para producir un vaciado completo en el silicio sería mucho menor debida a la ubicuidad de electrodos en todo el volumen.

El Instituto de Microelectrónica de Barcelona (IMB) desarrolló un detector de acuerdo con la filosofía de Parker y Kenney. Originalmente, los detectores del IMB (U3DTHIN) se emplearon en física del plasma y detección de neutrones, pero debido a su reducido tamaño y volumen activo se estimó su uso en el campo de la microdosimetría.

Estos detectores son diodos PIN fabricados en obleas de silicio sobre aislante con grosores de 10 o 20 μm, con capas de óxido de 1 μm. El sistema está montado sobre un soporte de silicio de 300 μm de grosor. Las columnas tienen un diámetro de 5 μm y están rellenas de silicio dopado (p o n), con cada tipo conectado a un electrodo de colección diferente, obteniendo, por tanto, un solo canal de lectura. Las columnas tienen un pitch de 80 μm entre dos columnas del mismo tipo. El área total del detector es de 1024 $\times$ 1024 μm^2. Puede verse un esquema del

detector en la figura 3.1.

Una de las ventajas de este tipo de geometría, como se mencionó antes, es que el volumen de vaciado del detector no depende en el grosor del silicio, sino en la longitud y radio de los electrodos columnares dado que la región de vaciado crecerá transversalmente, a diferencia de la geometría planar donde crece longitudinalmente. Esto permite capacitancias más bajas que en detectores planares para geometrías por debajo de 50 μm, obteniendo señales de ruido mucho más bajas. A continuación, en la tesis se describe el proceso de fabricación de este tipo de detectores.

El segundo tipo de detector descrito en la tesis es una mejora del modelo original, denomindo "3D Cylindrical microdosimeter", capaz de realizar lecturas individuales de cada uno de los píxeles de los que se compone. Esta mejora se diseñó exclusivamente para su uso en microdosimetría y se basa en todo el conocimiento obtenido con el U3DTHIN por parte del IMB. Este sistema se basa en una matriz de diferentes volúmenes cilíndricos de lectura que imita células mamíferas [90]. El volumen unidad del detector es una estructura cilíndrica con un electrodo p+ implantado que colecta la carga y rodeado de una trinchera tridimensional n+. El eje de este cilindro es perpendicular al plano de la oblea del silicio. Hay 11 x 11 celdas en el detector, formando una matriz cuadrada. El diámetro y separación entre los electrodos puede tomar diferentes valores dependiendo del model, con diámetros de 9, 10, 15, 20 y 25 μm y pitches de 25, 50, 200 y 200 μm. En la figura 3.10 puede verse un esquema del dispositivo.

En el caso del detector empleado en esta tesis, el diámetro del electrodo central es de 4 μm y la anchura de la trinchera es de 3 μm. Cada una de las celdas está conectada individualmente a un pad a través de conductores metálicos, permitiendo la operación independiente de cada una de las células y ofreciendo resolución espacial en la medida. Los electrodos n de todas las celdas están conectados a un único pad. El grosor del detector es de (5.50$\pm$0.50) μm y el sustrato bajo el detector se eliminó para evitar la retrodispersión de las partículas. En la tesis se detalla también en este caso el proceso de fabricación de los detectores.

A continuación se detalla el procedimiento de lectura de los detectores y se

describe el sistema eléctrico empleado para obtener la señal, mostrando los esquemáticos de los circuitos empleados para tal fin. Se detalla también el proceso de calibración de los detectores y finalmente se describe uno de los posibles factores limitantes del sistema: la eficiencia de colección de carga.

Una de las desventajas del uso de este tipo de sistemas para la detección de radiación es que existen fenómenos de deriva y difusión de carga que provocan una colección parcial de carga en la periferia del volumen de vaciado, modificando los espectros microdosimétricos leídos. Este efecto de colección parcial de carga produce una perturbación en la reconstrucción de la distribución de altura de pulso (como por ejemplo, la energía impartida) respecto de las distribuciones microdosimétricas reales. La importancia de esta perturbación depende de la geometría del detector, las condiciones de operación y el ruído del sistema de lectura.Se ha evaluado este fenómeno en los microdosímetros cilíndricos tridimensionales del IMB (3D Cylindrical Microdosimeter). Para parametrizar la eficiencia de colección de carga por parte de los volúmenes activos se realizó un test IBIC en las instalaciones del Centro Nacional de Aceleradores (CNA, Sevilla, España) y los resultados se compararon con simulaciones TCAD del volumen activo. Una vez realizada la parametrización de la colección parcial de carga se modificaron espectros microdosimétricos obtenidos con el software FLUKA Monte Carlo y se compararon con espectros obtenidos experimentalmente en las instalaciones de la Fundación CNAO (Pavía, Italia), obteniendo un acuerdo siginificativo entre los espectros Monte Carlo modificados y los tomados experimentalmente.

También se realizó un estudio del umbral de energía lineal mínimo detectable en dispositivos sin ganancia intrínseca mediante un modelo general de la señal en función de la densidad másica pesada en fluencia de microdosímetros de estado sólido.

En el siguiente capítulo se describen las pruebas realizadas para evaluar el comportamiento de los microdosímetros descritos en el capítulo anterior. Los microdosímetros U3DTHIN se testaron con iones de ^{12}C en las instalaciones de GANIL (Caén, Francia), mientras que la siguiente generación de detectores se testó tanto con protones como iones de ^{12}C en las instalaciones de la Fundación CNAO (Pavía, Italia), una institución pública italiana de terapia de partículas.

Los resultados se compararon con simulaciones por Monte Carlo realizadas con FLUKA.

En el caso de los detectores de silicio U3DTHIN, las pruebas en GANIL muestran que es posible el uso de este tipo de estructuras tridimensionales de silicio para la medida de distribuciones microdosimétricas en haces de iones. La posibilidad de poder realizar este tipo de medidas permitiría un análisis realista a la hora de comisionar haces de terapia de partículas. El dispositivo experimental incluía una cuña motorizada de PMMA que permitió el control del grosor efectivo atravesado por el haz con una precisión de alrededor de 30 μm. Los resultados experimentales de las distribuciones microdosimétricas de energía lineal y $d(y)$ se compararon con las obtenidas en FLUKA, obteniendo un acuerdo excelente para los valores de energía lineal más probable en función del grosor de PMMA. Para evaluar este acuerdo se empleó un test gamma [105] con tolerancias Δy igual al 10 % de la energía lineal más probable en cada punto de la curva de Bragg y una tolerancia $\Delta z = 0{,}5$ mm entre las simulaciones por FLUKA y los datos experimentales, obteniendo valores de $\gamma < 0{,}65$. En el caso de valores de energía lineal promediados en dosis el acuerdo es mejor que 1,2 en el test γ . Los resultados indican que las estructuras ultrafinas de silicio 3D pueden usarse para caracterizar las propiedades microdosimétricas de haces de iones. Sin embargo, existen algunos problemas que limitan el rango dinámico del detector y existen fenómenos de apilamiento.

En cuanto al otro tipo de detectores descritos (3D Cylindrical Microdosimeters) testados en CNAO se ha comprobado su correcto funcionamiento con tasas de fluencia clínicas de hasta 5×10^7 s^{-1} cm^{-2} sin existir fenómenos de saturación. Con el mismo montaje experimental que en el caso de los detectores testados en GANIL se ha comprobado que se muestra un gran acuerdo entre los espectros obtenidos experimentalmente y aquellos calculados mediante simulaciones por Monte Carlo, con valores en el test gamma menores a 0,25, con las mismas tolerancias que en el experimento anterior para valores más probables de energía lineal. En el caso de valores de energía lineal promediados en dosis se muestra un acuerdo bueno, aunque siguen existiendo fenómenos de apliamiento y cross-talk entre células vecinas. Existía un poco de ruido proveniente de la etapa

de amplificación que emborronaba ligeramente los resultados, especialmente si se compara con el resultado de valores más probables. Los test gamma en este caso toman valores menores a 1,2 en general; y menores a 0,3 en las proximidades del pico de Bragg. En general, los espectros microdosimétricos se ajustan correctamente a los simulados por Monte Carlo.

También se calcularon valores de RBE utilizando el modelo MKM mediante la conversión de energía impartida en silicio a energía específica corregida por saturación y promediada en dosis, permitiendo el cálculo de dosis biológica. Estos resultados indican que los microdosimétros cilíndricos de silicio empleados en esta tesis se pueden usar para caracterizar propiedades radiobiológicas y microdosimétricas de haces de alto LET como los empleados en hadronterapia. Los valores de RBE se usaron también para evaluar las tolerancias a usar en los test gamma realizados a las medidas experimentales descritas en esta tesis para ambos tipos de detectores de silicio.

Finalmente, en el último capítulo se detallan las conclusiones del trabajo y se hace una discusión sobre posible trabajo futuro para mejorar el detector. Las conclusiones pueden ser resumidas en los siguientes puntos:

- **Se ha demostrado la posibilidad del uso de detectores de silicio microestructurados para aplicaciones de microdosimetría.**
- **Es posible calcular el RBE de las distribuciones microdosimétricas y la estimación de incertidumbres en base a dichos valores de RBE.**
- **Se han realizado estimaciones de la longitud media de traza de las partículas primarias que atraviesan el detector, pasando de un paradigma basado en la μ-*randomness* a uno basado en fluencia clínica.**
- **Se ha comisionado el software de Monte Carlo FLUKA para su uso en aplicaciones de microdosimía a través de una comparación con datos tomados con una cámara de pico de Bragg PTW 34080 sita en una columna variable de agua PTW Peakfinder en un**

haz de iones de ^{12}C con una energía de 115,2 MeV A^{-1} en las instalaciones de la Fundación CNAO.

- **Se ha desarrollado y testeado un sistema de lectura basado en electrónica discreta diseñado para su uso en los microdosímetros de silicio empleados en este trabajo.**

- **Se han estudiado y evaluado las limitaciones del sistema de detección empleado en esta tesis.**

En cuanto al trabajo futuro a realizar, es necesario mejorar la eficiencia de colección de carga. Entre las posibles mejoras que podrían evitar el problema está el hecho de replicar la estructura para añadir una segunda y una tercera trincheras imitando la forma de una diana de dardos añadiendo regiones p entre las trincheras n para hacer más grande la eficiencia de colección de carga en las regiones periféricas. Esta mejora está en fase de diseño en estos momentos. Otra cosa que se puede mejorar es la lectura de múltiples células a la vez. En los experimentos descritos en la tesis sólo se ha leído una célula. Para poder tener un sistema que permita detección espacial el resto de células deberían ser elídas. Una opción en consideración está basada en el uso de FPGAs VATAGP7.1.

Los detectores se emplearán en diferentes proyectos a nivel europeo relacionados con la terapia de partículas y radiobiología. Las posibles aplicaciones son la terapia de protones mediante mini-beam (PMBRT) en la que se emplean campos pequeños de radiación con un fraccionamiento espacial de la dosis, lo cual incrementa la resistencia del tejido sano a los efectos de la radiación durante el tratamiento. El segundo proyecto tiene que ver con terapia FLASH. En este tipo de terapia se usan rayos X, electrones o protones para depositar una dosis muy elevada de radiación en tiempos muy cortos. Las herramientas usadas tradicionalmente en radioterapia no pueden usarse en FLASH debido a la alta tasa de fluencia. Se está investigando la idoneidad de los detectores de silicio descritos en esta tesis para su uso en PMBRT y FLASH.

Finalmente, en los apéndices se muestran los resultados parciales de las pruebas con protones y un ejemplo del código empleado en la modificación de los

espectros de Monte Carlo debido a la eficiencia de colección parcial de carga.

USC
UNIVERSIDADE
DE SANTIAGO
DE COMPOSTELA

USC
UNIVERSIDADE
DE SANTIAGO
DE COMPOSTELA

USC
UNIVERSIDADE
DE SANTIAGO
DE COMPOSTELA

Bibliography

[1] D. Hanahan and R. A. Weinberg, "The hallmarks of cancer," *Cell*, vol. 100, no. 1, pp. 57–70, 2000.

[2] D. Hanahan and R. A. Weinberg, "Hallmarks of cancer: the next generation," *Cell*, vol. 144, no. 5, pp. 646–674, 2011.

[3] S. McGuire, "World cancer report 2014. geneva, switzerland: World health organization, international agency for research on cancer, WHO press, 2015," 2016.

[4] B. D. Smith, G. L. Smith, A. Hurria, G. N. Hortobagyi, and T. A. Buchholz, "Future of cancer incidence in the united states: burdens upon an aging, changing nation," *Journal of clinical oncology*, vol. 27, no. 17, pp. 2758–2765, 2009.

[5] G. Delaney, S. Jacob, C. Featherstone, and M. Barton, "The role of radiotherapy in cancer treatment: estimating optimal utilization from a review of evidence-based clinical guidelines," *Cancer: Interdisciplinary International Journal of the American Cancer Society*, vol. 104, no. 6, pp. 1129–1137, 2005.

[6] M. B. Barton, S. Jacob, J. Shafiq, K. Wong, S. R. Thompson, T. P. Hanna, and G. P. Delaney, "Estimating the demand for radiotherapy from the evidence: a review of changes from 2003 to 2012," *Radiotherapy and Oncology*, vol. 112, no. 1, pp. 140–144, 2014.

[7] J. Thariat, J.-M. Hannoun-Levi, A. S. Myint, T. Vuong, and J.-P. Gérard, "Past, present, and future of radiotherapy for the benefit of patients," *Nature Reviews Clinical Oncology*, vol. 10, no. 1, pp. 52–60, 2013.

[8] *Absorbed Dose Determination in External Beam Radiotherapy.* No. 398 in Technical Reports Series, Vienna: IAEA, 2001.

[9] G. J. Kutcher, L. Coia, M. Gillin, W. F. Hanson, S. Leibel, R. J. Morton, J. R. Palta, J. A. Purdy, L. E. Reinstein, G. K. Svensson, *et al.*, "Comprehensive qa for radiation oncology: report of AAPM radiation therapy committee task group 40," *Medical physics*, vol. 21, no. 4, pp. 581–618, 1994.

[10] R. R. Wilson, "Radiological use of fast protons," *Radiology*, vol. 47, no. 5, pp. 487–491, 1946.

[11] E. Fokas, G. Kraft, H. An, and R. Engenhart-Cabillic, "Ion beam radiobiology and cancer: Time to update ourselves," *Biochimica et Biophysica Acta (BBA) - Reviews on Cancer*, vol. 1796, no. 2, pp. 216 – 229, 2009.

[12] J. S. Loeffler and M. Durante, "Charged particle therapy: optimization, challenges and future directions," *Nature Reviews Clinical Oncology*, vol. 10, no. 7, p. 411, 2013.

[13] Particle Therapy Co-Operative Group, "PTCOG home page," 2019.

[14] M. Brada, M. Pijls-Johannesma, and D. De Ruysscher, "Current clinical evidence for proton therapy," *The Cancer Journal*, vol. 15, no. 4, pp. 319–324, 2009.

[15] P. Fang, Y. Shiraishi, V. Verma, W. Jiang, J. Song, B. P. Hobbs, and S. H. Lin, "Lymphocyte-sparing effect of proton therapy in patients with esophageal cancer treated with definitive chemoradiation," *International Journal of Particle Therapy*, vol. 4, no. 3, pp. 23–32, 2017.

[16] M. Zaider and H. H. Rossi, "Microdosimetry and its application to biological processes," in *Radiation dosimetry*, pp. 171–242, Springer, 1986.

[17] M. Zaider and H. H. Rossi, *Microdosimetry and its Applications*. Springer, 1996.

[18] V. Semenenko and R. Stewart, "Fast monte carlo simulation of DNA damage formed by electrons and light ions," *Physics in Medicine & Biology*, vol. 51, no. 7, pp. 1693–1706, 2006.

[19] Z. Francis, S. Incerti, V. Ivanchenko, C. Champion, M. Karamitros, M. Bernal, and Z. El Bitar, "Monte carlo simulation of energy-deposit clustering for ions of the same LET in liquid water," *Physics in Medicine & Biology*, vol. 57, no. 1, pp. 209–224, 2011.

[20] E. B. Podgoršak *et al.*, *Radiation physics for medical physicists*. Springer, 2006.

[21] International Commission on Radiation Units and International Commission on Radiological Units, *ICRU report 90: Key Data for Ionizing-Radiation Dosimetry: Measurement Standards and Applications*. Oxford University Press, 2014.

[22] H. Paganetti, *Proton therapy physics*. CRC press, 2018.

[23] M. Tanabashi, K. Hagiwara, K. Hikasa, K. Nakamura, Y. Sumino, F. Takahashi, J. Tanaka, K. Agashe, G. Aielli, C. Amsler, *et al.*, "Review of particle physics," *Phys. Rev. D*, vol. 98, p. 030001, Aug 2018.

[24] S. M. Seltzer and M. J. Berger, "Evaluation of the collision stopping power of elements and compounds for electrons and positrons," *The International Journal of Applied Radiation and Isotopes*, vol. 33, no. 11, pp. 1189–1218, 1982.

[25] R. M. Sternheimer, "The density effect for the ionization loss in various materials," *Physical Review*, vol. 88, no. 4, p. 851, 1952.

[26] M. J. Berger, M. Inokuti, H. H. Andersen, H. Bichsel, D. Powers, S. M. Seltzer, D. Thwaites, and D. E. Watt, "Stopping powers and ranges for protons and alpha particles, 1993," *International Commission on Radiation Units and Measurements ICRU Report 49*.

[27] J. J. Bevelacqua and B. Resources, "Systematics of heavy ion radiotherapy."

[28] P. Marmier and E. Sheldon, *Physics of Nuclei and Particles*, vol. 1. Academic Press, 1969.

[29] J. F. Ziegler, M. D. Ziegler, and J. P. Biersack, *SRIM: the stopping and range of ions in matter*. Cadence Design Systems, 2008.

[30] V. L. Highland, "Some practical remarks on multiple scattering," *Nuclear Instruments and Methods*, vol. 129, no. 2, pp. 497–499, 1975.

[31] G. R. Lynch and O. I. Dahl, "Approximations to multiple coulomb scattering," *Nuclear Instruments and Methods in Physics Research Section B: Beam Interactions with Materials and Atoms*, vol. 58, no. 1, pp. 6–10, 1991.

[32] G. Moliere, "Theorie der streuung schneller geladener teilchen ii mehrfach- und vielfachstreuung," *Zeitschrift für Naturforschung A*, vol. 3, no. 2, pp. 78–97, 1948.

[33] H. A. Bethe, "Moliere's theory of multiple scattering," *Physical review*, vol. 89, no. 6, p. 1256, 1953.

[34] E. B. Podgorsak *et al.*, *Radiation oncology physics*. International Atomic Energy Agency, 2005.

[35] J.-E. García-Ramos, C. E. Alonso, M. V. Andrés, and F. Pérez-Bernal, *Basic Concepts in Nuclear Physics: Theory, Experiments and Applications*. Springer, 2015.

[36] H. Paganetti, "Nuclear interactions in proton therapy: dose and relative biological effect distributions originating from primary and secondary particles," *Physics in Medicine & Biology*, vol. 47, no. 5, p. 747, 2002.

[37] E. Haettner, H. Iwase, M. Krämer, G. Kraft, and D. Schardt, "Experimental study of nuclear fragmentation of 200 and 400 mev/u 12c ions in water for applications in particle therapy," *Physics in Medicine & Biology*, vol. 58, no. 23, p. 8265, 2013.

[38] C. J. Malmer, "ICRU report 63. nuclear data for neutron and proton radiotherapy and for radiation protection," *Medical Physics*, vol. 28, no. 5, pp. 861–861, 2001.

[39] F. H. Attix, *Introduction to radiological physics and radiation dosimetry*. John Wiley & Sons, 2008.

[40] International Commission on Radiation Units, *ICRU Report 16: Linear energy transfer*, vol. 16. ICRU, 1970.

[41] H. H. Rossi and W. Rosenzweig, "Measurements of neutron dose as a function of linear energy transfer," *Radiation Research*, vol. 2, no. 5, pp. 417–425, 1955.

[42] K. S. J. Wilson and S. B. Field, "Measurement of LET spectra using a spherical tissue-equivalent proportional counter," *Physics in Medicine & Biology*, vol. 15, pp. 657–666, oct 1970.

[43] A. M. Kellerer, "An algorithm for LET-analysis," *Physics in Medicine & Biology*, vol. 17, pp. 232–240, mar 1972.

[44] P. D. Bradley, *The development of a novel silicon microdosimeter for high LET radiation therapy. PhD thesis.* University of Wollongong, 2000.

[45] D. Bolst, S. Guatelli, L. T. Tran, L. Chartier, M. L. Lerch, N. Matsufuji, and A. B. Rosenfeld, "Correction factors to convert microdosimetry measurements in silicon to tissue in 12c ion therapy," *Physics in Medicine & Biology*, vol. 62, no. 6, p. 2055, 2017.

[46] G. Magrin, "A method to convert spectra from slab microdosimeters in therapeutic ion-beams to the spectra referring to microdosimeters of different shapes and material," *Physics in Medicine & Biology*, vol. 63, no. 21, p. 215021, 2018.

[47] R. Coleman, "Random paths through convex bodies," *Journal of Applied Probability*, vol. 6, no. 2, pp. 430–441, 1969.

[48] M. C. Joiner and A. Van der Kogel, *Basic clinical radiobiology*. CRC press, 2016.

[49] B. S. Sørensen, J. Overgaard, and N. Bassler, "In vitro RBE-LET dependence for multiple particle types," *Acta Oncologica*, vol. 50, no. 6, pp. 757–762, 2011.

[50] C. P. Karger and P. Peschke, "RBE and related modeling in carbon-ion therapy," *Physics in Medicine & Biology*, vol. 63, no. 1, pp. 01–02, 2017.

[51] J. F. Fowler, "The linear-quadratic formula and progress in fractionated radiotherapy," *The British Journal of Radiology*, vol. 62, no. 740, pp. 679–694, 1989.

[52] T. Kanai, Y. Furusawa, K. Fukutsu, H. Itsukaichi, K. Eguchi-Kasai, and H. Ohara, "Irradiation of mixed beam and design of spread-out bragg peak for heavy-ion radiotherapy," *Radiation research*, vol. 147, no. 1, pp. 78–85, 1997.

[53] G. Kraft, M. Krämer, and M. Scholz, "LET, track structure and models," *Radiation and environmental biophysics*, vol. 31, no. 3, pp. 161–180, 1992.

[54] R. Hawkins, "A microdosimetric-kinetic model of cell death from exposure to ionizing radiation of any let, with experimental and clinical applications," *International journal of radiation biology*, vol. 69, no. 6, pp. 739–755, 1996.

[55] H. H. Rossi and W. Rosenzweig, "A device for the measurement of dose as a function of specific ionization," *Radiology*, vol. 64, no. 3, pp. 404–411, 1955.

[56] L. De Nardo, V. Cesari, G. Donà, G. Magrin, P. Colautti, V. Conte, and G. Tornielli, "Mini-TEPCs for radiation therapy," *Radiation Protection Dosimetry*, vol. 108, no. 4, pp. 345–352, 2004.

[57] D. Srdoč, "Experimental technique of measurement of microscopic energy distribution in irradiated matter using rossi counters," *Radiation Research*, vol. 43, no. 2, pp. 302–319, 1970.

[58] F. R. Shonka, "Conducting plastic equivalent to tissue, air and polystyrene," *Progress in Nuclear Energy, Series*, vol. 12, pp. 184–187, 1958.

[59] P. Kliauga, A. Waker, and J. Barthe, "Design of tissue-equivalent proportional counters," *Radiation Protection Dosimetry*, vol. 61, no. 4, pp. 309–322, 1995.

[60] S. B. Guetersloh, T. B. Borak, P. J. Taddei, C. Zeitlin, L. Heilbronn, J. Miller, T. Murakami, and Y. Iwata, "The response of a spherical tissue-equivalent proportional counter to different ions having similar linear energy transfer," *Radiation Research*, vol. 161, no. 1, pp. 64–71, 2004.

[61] T. Nunomiya, E. Kim, T. Kurosawa, S. Taniguchi, S. Yonai, T. Nakamura, Y. Nakane, Y. Sakamoto, and S. Tanaka, "Measurement of lineal-energy distributions for neutrons of 8 kev to 65 mev by using a tissue-equivalent proportional counter," *Radiation Protection Dosimetry*, vol. 102, no. 1, pp. 49–59, 2002.

[62] S. Chiriotti, A. Parisi, F. Vanhavere, M. De Saint-Hubert, C. Vandevoorde, J. Slabbert, P. Beukes, E. de Kock, and J. Symons, "Microdosimetric measurement of secondary radiation in the passive scattered proton therapy room of ithemba labs using a tissue-equivalent proportional counter," *Radiation Protection Dosimetry*, vol. 182, no. 2, pp. 252–257, 2018.

[63] J. Shinn, G. Badhwar, M. Xapsos, F. Cucinotta, and J. t. Wilson, "An analysis of energy deposition in a tissue equivalent proportional counter onboard the space shuttle," *Radiation Measurements*, vol. 30, no. 1, pp. 19–28, 1999.

[64] P. Colautti, V. Conte, A. Selva, S. Chiriotti, A. Pola, D. Bortot, A. Fazzi, S. Agosteo, and M. Ciocca, "Microdosimetric study at the cnao active-scanning carbon-ion beam," *Radiation Protection Dosimetry*, vol. 180, pp. 157–161, 10 2017.

[65] M. Farahmand, A. Bos, L. De Nardo, and C. Van Eijk, "First microdosimetric measurements with a tepc based on a gem," *Radiation Protection Dosimetry*, vol. 110, no. 1-4, pp. 839–843, 2004.

[66] K. G. McKay, "Electron-hole production in germanium by alpha-particles," *Physical Review*, vol. 84, pp. 829–832, Nov 1951.

[67] N. Tsoulfanidis, *Measurement and detection of radiation*. CRC press, 2010.

[68] G. F. Knoll, "Semiconductor diode detectors," in *Radiation detection and measurement*, ch. 11, John Wiley & Sons, 2010.

[69] A. Owens and A. Peacock, "Compound semiconductor radiation detectors," *Nuclear Instruments and Methods in Physics Research Section A: Accelerators, Spectrometers, Detectors and Associated Equipment*, vol. 531, no. 1-2, pp. 18–37, 2004.

[70] H. Spieler, *Semiconductor detector systems*. Oxford university press, 2005.

[71] C. A. Klein, "Semiconductor particle detectors: A reassessment of the fano factor situation," *IEEE Transactions on Nuclear Science*, vol. 15, no. 3, pp. 214–225, 1968.

[72] R. Alig, S. Bloom, and C. Struck, "Scattering by ionization and phonon emission in semiconductors," *Physical Review B*, vol. 22, no. 12, p. 5565, 1980.

[73] J. Hammersley, *Monte carlo methods*. Springer Science & Business Media, 2013.

[74] N. Metropolis and S. Ulam, "The Monte Carlo method," *Journal of the American statistical association*, vol. 44, no. 247, pp. 335–341, 1949.

[75] J. E. Gentle, *Random number generation and Monte Carlo methods*. Springer Science & Business Media, 2013.

[76] S. Agostinelli, J. Allison, K. a. Amako, J. Apostolakis, H. Araujo, P. Arce, M. Asai, D. Axen, S. Banerjee, G. . Barrand, *et al.*, "Geant4 - a simulation toolkit," *Nuclear Instruments and Methods in Physics Research Section A: Accelerators, Spectrometers, Detectors and Associated Equipment*, vol. 506, no. 3, pp. 250–303, 2003.

[77] C. Werner, J. Bull, S. Solomon, *et al.*, "MCNP6.2 release notes," tech. rep., LA-UR-18-20808, Los Alamos National Laboratory, 2018.

[78] I. Kawrakow and D. Rogers, "The EGSnrc code system," 2000.

[79] F. Salvat, J. M. Fernández-Varea, and J. Sempau, "Penelope-2008: A code system for monte carlo simulation of electron and photon transport," in *Workshop proceedings*, vol. 4, Nuclear Energy Agency, Organization for Economic Co-operation and Development, 2006.

[80] A. Ferrari, P. Sala, A. Fasso, and J. Ranft, "FLUKA: a multi-particle transport code, cern 2005-10 (2005)," tech. rep., INFN/TC_05/11, SLAC, 2005.

[81] T. Böhlen, F. Cerutti, M. Chin, A. Fassò, A. Ferrari, P. Ortega, A. Mairani, P. R. Sala, G. Smirnov, and V. Vlachoudis, "The FLUKA code: developments and challenges for high energy and medical applications," *Nuclear data sheets*, vol. 120, pp. 211–214, 2014.

[82] T. T. Böhlen, F. Cerutti, M. Dosanjh, A. Ferrari, I. Gudowska, A. Mairani, and J. Quesada, "Benchmarking nuclear models of FLUKA and GEANT4 for carbon ion therapy," *Physics in Medicine & Biology*, vol. 55, no. 19, pp. 5833–5847, 2010.

[83] S. I. Parker, C. J. Kenney, and J. Segal, "3d-a proposed new architecture for solid-state radiation detectors," *Nuclear Instruments and Methods in Physics Research Section A: Accelerators, Spectrometers, Detectors and Associated Equipment*, vol. 395, no. 3, pp. 328–343, 1997.

[84] G. Pellegrini, M. Lozano, M. Ullan, R. Bates, C. Fleta, and D. Pennicard, "First double-sided 3-d detectors fabricated at cnm-imb," *Nuclear Instruments and Methods in Physics Research Section A: Accelerators, Spectrometers, Detectors and Associated Equipment*, vol. 592, no. 1-2, pp. 38–43, 2008.

[85] F. García, G. Pellegrini, M. Lozano, J. Balbuena, C. Fleta, C. Guardiola, and D. Quirion, "Ultra thin 3D silicon detector for plasma diagnostics at

the ITER tokamak," in *2011 IEEE Nuclear Science Symposium Conference Record*, pp. 199–201, IEEE, 2011.

[86] C. Guardiola, F. Gómez, C. Fleta, J. Rodríguez, D. Quirion, G. Pellegrini, A. Lousa, L. Martínez-de Olcoz, M. Pombar, and M. Lozano, "Neutron measurements with ultra-thin 3D silicon sensors in a radiotherapy treatment room using a siemens PRIMUS linac," *Physics in Medicine & Biology*, vol. 58, no. 10, p. 3227, 2013.

[87] C. Guardiola, C. Fleta, M. Lozano, and G. Pellegrini, "Silicon planar detectors adapted to slow neutron detection," *International Journal of Numerical Modelling: Electronic Networks, Devices and Fields*, vol. 23, no. 4-5, pp. 324–331, 2010.

[88] L. T. Tran, D. A. Prokopovich, M. Petasecca, M. L. Lerch, C. Fleta, G. Pellegrini, C. Guardiola, M. I. Reinhard, and A. B. Rosenfeld, "Ultra-thin 3D detector: Charge collection characterization and application for microdosimetry," *IEEE Transactions on Nuclear Science*, vol. 61, no. 6, pp. 3472–3478, 2014.

[89] S. Esteban Martí, "Development of advanced silicon sensors for neutron detection and microdosimetry," 2016.

[90] C. Guardiola, D. Quirion, G. Pellegrini, C. Fleta, S. Esteban, M. Cortés-Giraldo, F. Gómez, T. Solberg, A. Carabe, and M. Lozano, "Silicon-based three-dimensional microstructures for radiation dosimetry in hadrontherapy," *Applied Physics Letters*, vol. 107, no. 2, p. 023505, 2015.

[91] G. F. Knoll, "Pulse processing and shaping," in *Radiation detection and measurement*, ch. 16, John Wiley & Sons, 2010.

[92] *OPA657 reference sheet.* Accessed: 2019-07-30.

[93] C. Fleta, S. Esteban, M. Baselga, D. Quirion, G. Pellegrini, C. Guardiola, M. Cortés-Giraldo, J. G. López, M. J. Ramos, F. Gómez, *et al.*, "3d cylindrical silicon microdosimeters: fabrication, simulation and charge collection study," *Journal of Instrumentation*, vol. 10, no. 10, p. P10001, 2015.

[94] J. Prieto-Pena, F. Gómez, C. Fleta, C. Guardiola, G. Pellegrini, M. Donetti, S. Giordanengo, D. M. González-Castaño, and J. Pardo-Montero, "Microdosimetric spectra measurements on a clinical carbon beam at nominal therapeutic fluence rate with silicon cylindrical microdosimeters," *IEEE Transactions on Nuclear Science*, vol. 66, pp. 1840–1847, July 2019.

[95] E. N. Gimenez, R. Ballabriga, M. Campbell, I. Horswell, X. Llopart, J. Marchal, K. J. S. Sawhney, N. Tartoni, and D. Turecek, "Study of charge-sharing in MEDIPIX3 using a micro-focused synchrotron beam," *Journal of Instrumentation*, vol. 6, pp. C01031–C01031, jan 2011.

[96] M. Campbell, E. Heijne, T. Holý, J. Idárraga, J. Jakubek, C. Lebel, C. Leroy, X. Llopart, S. Pospísil, L. Tlustos, and Z. Vykydal, "Study of the charge sharing in a silicon pixel detector by means of α-particles interacting with a Medipix2 device," *Nuclear Instruments and Methods in Physics Research Section A: Accelerators, Spectrometers, Detectors and Associated Equipment*, vol. 591, no. 1, pp. 38 – 41, 2008. Radiation Imaging Detectors 2007.

[97] M. J. Berger, J. Coursey, M. Zucker, J. Chang, *et al.*, *Stopping-power and range tables for electrons, protons, and helium ions*. NIST Physics Laboratory Gaithersburg, MD, 1998.

[98] V. Radeka, "Signal, noise and resolution in position-sensitive detectors," *IEEE Transactions on Nuclear Science*, vol. 21, no. 1, pp. 51–64, 1974.

[99] G. Bertuccio and A. Pullia, "A method for the determination of the noise parameters in preamplifying systems for semiconductor radiation detectors," *Review of Scientific Instruments*, vol. 64, no. 11, pp. 3294–3298, 1993.

[100] *CR-110 reference sheet*. Accessed: 2019-06-03.

[101] J. Soltani-Nabipour, D. Sardari, and G. Cata-Danil, "Sensitivity of the bragg peak curve to the average ionization potential of the stopping medium," *Romanian Journal of Physics*, vol. 54, no. 3/4, pp. 321–330, 2009.

[102] A. M. Kellerer, "Fundamentals of microdosimetry," *The dosimetry of ionizing radiation*, vol. 1, pp. 77–162, 1985.

[103] R. B. Hawkins, "A microdosimetric-kinetic model for the effect of non-poisson distribution of lethal lesions on the variation of RBE with LET," *Radiation research*, vol. 160, no. 1, pp. 61–69, 2003.

[104] T. Inaniwa, T. Furukawa, Y. Kase, N. Matsufuji, T. Toshito, Y. Matsumoto, Y. Furusawa, and K. Noda, "Treatment planning for a scanned carbon beam with a modified microdosimetric kinetic model," *Physics in Medicine & Biology*, vol. 55, no. 22, pp. 6721–6737, 2010.

[105] D. A. Low, W. B. Harms, S. Mutic, and J. A. Purdy, "A technique for the quantitative evaluation of dose distributions," *Medical physics*, vol. 25, no. 5, pp. 656–661, 1998.

[106] IDEAS, "ALIVATA product page page," 2019.

[107] Y. Prezado, G. Jouvion, A. Patriarca, C. Nauraye, C. Guardiola, M. Juchaux, C. Lamirault, D. Labiod, L. Jourdain, C. Sebrie, *et al.*, "Proton minibeam radiation therapy widens the therapeutic index for high-grade gliomas," *Scientific reports*, vol. 8, no. 1, p. 16479, 2018.

[108] C. Peucelle, C. Nauraye, A. Patriarca, E. Hierso, N. Fournier-Bidoz, I. Martínez-Rovira, and Y. Prezado, "Proton minibeam radiation therapy: Experimental dosimetry evaluation," *Medical Physics*, vol. 42, no. 12, pp. 7108–7113, 2015.

[109] Y. Prezado, P. Deman, P. Varlet, G. Jouvion, S. Gil, C. Le Clec'H, H. Bernard, G. Le Duc, and S. Sarun, "Tolerance to dose escalation in minibeam radiation therapy applied to normal rat brain: Long-term clinical, radiological and histopathological analysis," *Radiation Research*, vol. 184, no. 3, pp. 314 – 321 – 8, 2015.

[110] F. A. Dilmanian, Z. Zhong, T. Bacarian, H. Benveniste, P. Romanelli, R. Wang, J. Welwart, T. Yuasa, E. M. Rosen, and D. J. Anschel, "Interlaced x-ray microplanar beams: A radiosurgery approach with clinical potential,"

Proceedings of the National Academy of Sciences, vol. 103, no. 25, pp. 9709–9714, 2006.

[111] P. Deman, M. Vautrin, M. Edouard, V. Stupar, L. Bobyk, R. Farion, H. Elleaume, C. Rémy, E. L. Barbier, F. Estève, *et al.*, "Monochromatic minibeams radiotherapy: from healthy tissue-sparing effect studies toward first experimental glioma bearing rats therapy," *International Journal of Radiation Oncology, Biology, Physics*, vol. 82, no. 4, pp. e693–e700, 2012.

[112] Y. Prezado, S. Sarun, S. Gil, P. Deman, A. Bouchet, and G. Le Duc, "Increase of lifespan for glioma-bearing rats by using minibeam radiation therapy," *Journal of Synchrotron Radiation*, vol. 19, pp. 60–65, Jan 2012.

[113] W. Calvo, J. W. Hopewell, H. S. Reinhold, and T. K. Yeung, "Time- and dose-related changes in the white matter of the rat brain after single doses of x rays," *The British Journal of Radiology*, vol. 61, no. 731, pp. 1043–1052, 1988. PMID: 3208008.

[114] F. A. Dilmanian, T. M. Button, G. Le Duc, N. Zhong, L. A. Pena, J. A. Smith, S. R. Martinez, T. Bacarian, J. Tammam, B. Ren, P. M. Farmer, J. Kalef-Ezra, P. L. Micca, M. M. Nawrocky, J. A. Niederer, F. P. Recksiek, A. Fuchs, and E. M. Rosen, "Response of rat intracranial 9L gliosarcoma to microbeam radiation therapy," *Neuro-Oncology*, vol. 4, pp. 26–38, 01 2002.

[115] M. Durante, E. Bräuer-Krisch, and M. Hill, "Faster and safer? flash ultra-high dose rate in radiotherapy," *The British Journal of Radiology*, vol. 91, no. 1082, p. 20170628, 2018.

[116] V. Favaudon, L. Caplier, V. Monceau, F. Pouzoulet, M. Sayarath, C. Fouillade, M.-F. Poupon, I. Brito, P. Hupé, J. Bourhis, *et al.*, "Ultrahigh dose-rate flash irradiation increases the differential response between normal and tumor tissue in mice," *Science Translational Medicine*, vol. 6, no. 245, pp. 245ra93–245ra93, 2014.

[117] P. Montay-Gruel, K. Petersson, M. Jaccard, G. Boivin, J.-F. Germond, B. Petit, R. Doenlen, V. Favaudon, F. Bochud, C. Bailat, *et al.*, "Irradiation

in a flash: Unique sparing of memory in mice after whole brain irradiation with dose rates above 100 gy/s," *Radiotherapy and Oncology*, vol. 124, no. 3, pp. 365–369, 2017.

[118] V. Favaudon, C. Fouillade, and M. Vozenin, "Ultrahigh dose-rate," flash" irradiation minimizes the side-effects of radiotherapy," *Cancer Radiotherapie: Journal de la Societe Francaise de Radiotherapie Oncologique*, vol. 19, no. 6-7, pp. 526–531, 2015.

List of Figures

List of Tables

USC
UNIVERSIDADE
DE SANTIAGO
DE COMPOSTELA

List of publications of J. Prieto-Pena

The following is the list of already published works authored by Juan Prieto-Pena related to this thesis, presenting investigations of silicon devices for microdosimetry:

- J Prieto-Pena, F Gómez, C Fleta, S Esteban, D Quirion, G Pellegrini, M Lozano, Y Prezado, M Dos Santos, C Guardiola, G Montarou, Juan Pardo-Montero, *Microdosimetry with micro-pattern silicon devices*, 2016 Global Medical Engineering Physics Exchanges/Pan American Health Care Exchanges (GMEPE/PAHCE) (2016).
- F Gómez, C Fleta, S Esteban, D Quirion, G Pellegrini, M Lozano, Y Prezado, M Dos Santos, C Guardiola, G Montarou, J Prieto-Pena, Juan Pardo-Montero, *Measurement of carbon ion microdosimetric distributions with ultrathin 3D silicon diodes*, Phys. Med. Biol., 4036-4047, 61-11 (2016).
- Juan Prieto-Pena, Faustino Gómez, Celeste Fleta, Consuelo Guardiola, Giulio Pellegrini, Marco Donetti, Simona Giordanengo, Diego M González-Castaño, Juan Pardo-Montero, *Microdosimetric spectra measurements on a clinical carbon beam at nominal therapeutic fluence rate with silicon cylindrical microdosimeters*, IEEE Trans. Nucl. Sci., 1840-1847, 66-07 (2019).

The following is the list of already published works authored by Juan Prieto-

Pena, with no relations to the topic of the thesis:

- Luis Brualla-González, Aurelio Vázquez-Luque, Martín Zapata, Diego Miguel González-Castaño, Víctor Luna-Vega, Jacobo Guiu-Soto, Juan Prieto-Pena, Trinitat García, Domingo Granero, Aurora Vicedo, Joan Rosellò, Miguel Pombar, Faustino Gómez, Juan Pardo-Montero, *Development and clinical characterization of a novel 2041 liquid-filled ionization chambers array for high-resolution verification of radiotherapy treatments*, Med. Phys., 1771-1781, 45-4 (2018).

- J Prieto-Pena, F Gómez, DM Gonzalez-Castano, MT Flores-Arias, J Arines, C Bao-Varela, F Cambronero-López, A Martínez Maqueira, *Radiation characterisation and dosimetric measurements of a femtosecond pulsed laser ablation system*, J. Radiol. Prot., 716, 38-2 (2018).

- Luis Brualla-González, Aurelio Vázquez-Luque, Martín Zapata, Diego Miguel González-Castaño, Víctor Luna-Vega, Jacobo Guiu-Soto, Juan Prieto-Pena, Trinitat García, Domingo Granero, Aurora Vicedo, Joan Rosellò, Miguel Pombar, Faustino Gómez, Juan Pardo-Montero, *Erratum: Development and clinical characterization of a novel 2041 liquid-filled ionization chambers array for high-resolution verification of radiotherapy treatments*, Med. Phys., 3999-4000, 45-8 (2018).

Works in preparation:

- J Prieto-Pena, F Gómez, C. Guardiola, Anna Baratto-Roldán, M. C. Jiménez-Ramos, J. García López, M Baselga and C. Fleta, *On the limitation of microdosimetry based in microstructured solid state devices*, in preparation.

- C.Guardiola, A. Lallena, I. Martínez, J. Prieto-Pena, F. Gómez, Y. Prezado, *Monte Carlo comparative study in proton minibeam radiotherapy*, in preparation

- Neira, Sara; Brualla-Gonzalez, Luis; Prieto-Pena, Juan; Gomez, Faustino; Pardo-Montero, Juan, *A kinetic model of diode detector response to pulsed radiation beams*, submitted to Phys. Med. Biol.

Conference talks:

- J. Prieto-Pena, F. Gómez, C. Fleta, S. Esteban, D. Quirion, G. Pellegrini, M. Lozano, Y. Prezado, M. Dos Santos, C. Guardiola, G. Montarou, J. Pardo-Montero. *Microdosimetry with Micro-pattern Silicon Devices*, Global Medical Engineering Physics Exchanges & Pan American Health Exchanges - GMEPE/PAHCE 2016, Madrid (Spain), April 2016

- J. Prieto-Pena, F. Gómez, C. Fleta, G. Pellegrini, M. Donetti, S. Giordanengo, J. Pardo-Montero, D. M. GonzÃ¡lez-Castaño. *Measuring Hadrontherapy Distributions at Nominal Fluence Rate*, 56^{th} Annual Conference of the Particle Therapy Co-Operative Group (PTCOG), Yokohama (Japan), May 2017

- J. Prieto-Pena, F. Gómez, C. Fleta, C. Guardiola, G. Pellegrini, M. Donetti, S. Giordanengo, J. Pardo-Montero and D. M. GonzÃ¡lez-Castaño. *Development of silicon array microdosimeters*,1^{st} ESTRO Physics Workshop, Glasgow (United Kingdom), November 2017

- J. Prieto-Pena, F. Gómez, C. Fleta, C. Guardiola, G. Pellegrini. *Solid State Microdosimetry*, II Workshop Español de Protonterapia, Seville (Spain), March 2018

- Juan Prieto-Pena, Faustino Gómez, Consuelo Guardiola, Anna Baratto-Roldán, M.C. Jiménez-Ramos, Javier García López and Celeste Fleta. *Limitations of solid-state devices for microdosimetry applications*,3rd International Conference on Dosimetry and its Applications, Lisbon (Portugal), May 2019

USC
UNIVERSIDADE
DE SANTIAGO
DE COMPOSTELA